Optoelectronic Applications of Tin-based Oxides - Studies about Optical O_2 Sensing and Photovoltaics

Dissertation

approved for the attainment of the degree of
Doctor of Natural Science
(Dr. rer. nat.)
from the Faculty of Science of the University of Paderborn

Linda Kothe

Paderborn, June 2025

The experimental investigations for this work were carried out from November 2019 to October 2024 in the group of Prof. Dr. Michael Tiemann at the University of Paderborn in cooperation with Wöhler Technik GmbH. From January to June of 2023, experiments were executed in the group of Prof. Dr. Moungi Bawendi at the Massachusetts Institute of Technology.

Reviewer: Prof. Dr. Michael Tiemann

Prof. Dr. Cedrik Meier

Statement of Authorship

With this signature, I declare that I have completed this thesis independently and with all mentioned support and resources. The thesis has never been submitted to any examination authority in the same or similar form.

Paderborn, June 11, 2025

Danksagung

Mit der Abgabe meiner Dissertation möchte ich die Gelegenheit ergreifen, um meinen tiefen Dank an alle Personen auszusprechen, die zum Gelingen dieser Arbeit beigetragen oder mich auf dem Weg dorthin begleitet haben.

Besonders möchte ich mich bei *Prof. Dr. Michael Tiemann* für die Möglichkeit bedanken, unter seiner Leitung promovieren zu dürfen. Vielen Dank für Deine Geduld und Dein Vertrauen. Die vielen Rat- und Vorschläge, sowie Deine Unterstützung bei all meinen Vorgaben haben wesentlich zum Gelingen meiner Arbeiten beigetragen. Die Zeit in unserer Gruppe werde ich immer in positiver Erinnerung behalten.

Dazu möchte ich mich außerdem bei *Prof. Dr. Cedrik Meier* für die Übernahme des Zweitgutachtens bedanken. Die jahrelange positive Zusammenarbeit und gegenseitige Unterstützung haben mich sehr geprägt. Meine Ausflüge in die Physik waren immer schön.

Darüberhinaus möchte ich mich bei den Mitgliedern der Prüfungskommission *Prof. Dr. Martin Brehm* und *Prof. Dr. Julia Linnemann* für Ihren Beisitz bedanken.

An dieser Stelle möchte ich mich sehr herzlich bei *Dr. Stephan Ester* und *Dr. Michael Poeplau* bedanken. Seit wir uns kennen habt Ihr mir beide sehr viel Vertrauen entgegengebracht, mich unterstützt und meine akademische Laufbahn gefördert. Ohne Euch wäre unsere interdisziplinäre Zusammenarbeit sicherlich nicht so erfolgreich.

Dear *Prof. Dr. Moungi Bawendi*, thank you so much for welcoming me into your group and for your support. It was very educational and enjoyable to work with you. Our group ski trip has a special place in my heart.

Weiterhin möchte ich mich bei den vielen Kollegen bedanken, mit denen ich mehr oder weniger täglich Zeit verbringen durfte. Vielen Dank für die zahlreichen schönen Momente und Diskussionen.

Lieber *Dr. Dominik Baier*, uns verbinden vor allem lange Zugfahrten, viele Vorträge und eigentlich immer gutes Frühstück. Danke für die vielen schönen Dienstreisen.

Maria Beyer, auch wenn Du noch nicht lange bei uns bist, habe ich Dich ins Herz geschlossen. Deine witzige Art und Dein Talent für Memes bringen mich immer zum Lachen. Danke für Deine offene und direkte Art. Alles Gute für Deine Zukunft, ich glaube an Dich.

Lieber *Jannik Breda*, vielen Dank für Deine Unterstützung im Labor und die vielen schönen Momente im Praktikum. Auch in schwierigen Situationen konnte ich mich auf Dich verlassen.

Vielen Dank *Dr. Stephan Ester*, dass Du immer ein offenes Ohr für mich hattest und auch in Deinem wohlverdienten Ruhestand für mich da bist. Dein Weitblick und Offenheit haben mich immer sehr beeindruckt. Du hast mir sehr viel beigebracht.

Liebe *Britta Fremerey*, vielen Dank für Deine zahlreiche Unterstützung im Umgang mit der Verwaltung. Ohne Dich wäre ich sicher an verschiedensten Formularen verzweifelt. Wir sehen uns dann im Gym ;)

Christiane Gloger, bei Dir geht mir einfach das Herz auf. Vielen Dank, dass Du immer wieder für mich da warst. Du bist unser Sonnenschein und für immer top vorbereitet im Praktikum.

Bei *Dr. Matthias Grotevent* möchte ich mich für die außergewöhnliche transatlantische Zusammenarbeit bedanken. Danke für Deine Unterstützung und die vielen schönen Mittagessen bei Life alive.

Lieber *Prof. Dr. Bernd Henning*, vielen Dank für die langjährige gute Zusammenarbeit. Die Diskussionen mit Dir sind immer sehr spannend und haben meinen Horizont erweitert.

Mario Hüsten, Dein trockener Humor und Deine ruhige Art sind die Seele in unserem Büro. Danke für die vielen lustigen und guten Gespräche. Melde mich bei Dir, wenn ich wieder Probleme mit den rostigen Gasflaschen habe.

Liebe *Josefin Klippstein*, mit Dir zusammen zu arbeiten vermisse ich jeden Tag. Dein Humor, Engagement und Deine fachlichen Beiträge haben mich sehr inspiriert. Danke für die unvergessliche Zeit mit Dir.

Bei *Dr. Marvin Kloß* möchte ich mich für die ausgiebigen Studien der Kategorie *Humor* bedanken. Du bringst mich vielleicht manchmal zum Lachen. Danke für die schönen Ausflüge mit unseren RISE Studentinnen.

Dear *Chantalle Krajewska*, the endeavor to attain a higher education has been successfully completed. Whenever you get lost in the catacombs, I will find you. Thank you for the fun adventures.

Ohne *Christian Leifels* hätte ich niemals die vielen Messgeräte ans Laufen gebracht. Danke, dass Du mir immer damit geholfen hast.

Ach *Anabel Miletic*. Danke für die schöne Zeit mit Dir. Deine Stärke, Liebe und Beharrlichkeit haben mich sehr geprägt und inspiriert. Wenn Du lachst, weiß ich, dass es ein guter Tag wird.

Lieber *Dr. Michael Poeplau*, bei Dir möchte ich mich vor allem für Deine motivierenden Worte bedanken. Danke, dass ich immer zu Dir kommen kann und Du immer an mich glaubst. Ich habe viel von Dir gelernt.

Ohne *Anke Schoch* hätte ich niemals den Mut gehabt Chemie zu studieren. Danke, dass Du mich auf diesem Weg begleitet hast. Dein legendärer Humor vertreibt auch die dunkelsten Wolken.

Dear *Dr. Tara Šverko*, meeting you was one of my highlights in the U.S.. You are such a force and I adore you dearly. Thank you for teaching me how to ski.

Bei *Prof. Dr. Michael Tiemann* möchte ich mich vor allem dafür bedanken, dass er sich immer auf unsere Aktivitäten eingelassen hat. Bitte vergiss für die nächsten Jahre nicht, dass Glätten verboten ist.

Lieber *Sven Voth*, vielen Dank, dass ich Dich auf Deiner akademischen Laufbahn begleiten durfte. Dich jetzt als Doktorand zu erleben macht mich sehr glücklich. Viel Erfolg für Deine Zukunft.

Vielen Dank *Dr. Thorsten Wagner*, dass Du mich auf meine Promotionszeit so gut vorbereitet hast. Die Arbeit mit Dir hat mich eigenständiger gemacht und für viele andere Themengebiete sensibilisiert.

Tobias Wagner danke ich besonders für die schöne Zeit im Praktikum. Hoffentlich muss ich nicht nochmal umkristallisieren. Dein 1. Platz am Buffet ist reserviert. Pass nur auf, dass Deine Pflanzen Dich nicht vorher umbringen.

Vielen dank *Dr. Christian Weinberger*, dass Du immer für mich da warst. Ganz besonders, wenn ich dumme Fehler im Labor gemacht habe. Danke für Deinen Humor und die liebevolle Pflege der Kaffeemaschine.

Bei *Marc Wengenroth* möchte ich mich für die unzähligen Busfahrten zwischen Paderborn und Bad Wünnenberg bedanken. Auch für unsere Gespräche über Python und Deine Unterstützung beim Programmieren bin ich sehr dankbar.

Liebe *Katharina Wördehoff*, vielen Dank, dass Du Dich so engagiert um den Gasmischer gekümmert hast. Deine Geschichten bringen mich immer zum Lachen. Danke für Deine Unterstützung.

Bei *Zhenyu Zhao* möchte ich mich vor allem für die vielen lustigen Momente bedanken. Deine gute Laune ist sehr ansteckend. Mit Deinen Photoshop Skills wirst Du die Welt beherrschen.

Besonders möchte ich mich bei den Kollegen bedanken, die meine Proben vermessen haben. Die PXRD Crew hat immer alles gegeben. Auch die Flachwitze Fraktion hat meinen Alltag erheitert. Danke für dieses Geschenk.

Außerdem möchte ich mich bei *Maximilian Albert*, *Dr. Hans Egold*, *Dr. Christian Golla*, *Andrea Harbath*, *Dr. Ronja Köthemann*, *Heike Mulka*, *Dr. Adam Neuba*, *Karin Stolte* und *Theresa Struckmeier* für die stets herzliche und kollegiale Zusammenarbeit bedanken.

Dr. Sabrina Amrehn, *Benjamin Fanselow*, *Dr. Ali Javed*, *Laureen Kieke*, *Lena-Sophie Knoop*, *Xi Li*, *Marcus Reese*, *Victoria Reichel*, *Dominik Rengel*, *Lara Schäfers* und *Bertram Schwind* danke ich für die schöne gemeinsame Zeit in unserer Gruppe.

Auch meinen Kollegen der Wöhler Technik GmbH danke ich für die positive und herzliche Zusammenarbeit, darunter ganz besonders *Julia Besse*, *Julian Erlemeier*, *Mohammed Ferchichi*, *Tobias Korb*, *Christoph Kreipe*, *Sebastian Leifels*, *Michael Mosmann*, *Karsten Nelle*, *Simon Omelich*, *Eike Rahlf*, *Alexander Stizenberg*, *Raphael Stümpel*, *Dr. Carsten Unverzagt* und *Johanna von Reth*.

I would also like to express my special gratitude to the members of the Bawendi lab, especially *Dimuthu Arachchi*, *Dr. David Berkinsky*, *Niamh Brown*, *Shelby Elder*, *Jonah Horowitz*, *Dr. Alex Kaplan*, *Aaron Li*, *Yongli Lu*, *Kaelyn McFarlane-Connelly*, *Li Miao*, *Oliver Nix*, *Dr. Cole Perkinson*, *Meng-Chen Shih*, *Shreyas Srinivasan*, *Dr. Shaun Tan* and *Dr. Hua Zhu*. I appreciate your warm welcome and the great time we had.

Von Herzen danke ich *Janina Hofmann*, *Dr. Waldemar Keil*, *Josefin Klippstein*, *Anton Kreft*, *Anabel Miletic*, *Tobias Wagner*, *Leonie Wieneke*, *Aaron und Jana Wrede* sowie *Swaantje und Torben Zöllner* für die jahrelange Unterstützung. Ihr seid die besten Freunde, die man sich wünschen kann und Ihr bedeutet mir sehr viel. Auf unsere kommenden Abenteuer freue ich mich sehr.

Abschließend möchte ich mich bei meiner Familie bedanken. Besonders meinen Eltern, *Gaby* und *Manfred*, sowie meinem Bruder *Nils* danke ich von Herzen. Ihr habt immer an mich geglaubt und mich unterstützt. Danke, dass Ihr immer für mich da seid.

I've had the time of my life
No, I never felt this way before
Yes, I swear, it's the truth
And I owe it all to you

- *Bill Medley und Jennifer Warnes*

Es gilt, wie immer, das Gibihmsche Prinzip.

- *Walter von Gibihm*

List of Publications

Publications in Journals

1. L. Kothe, M. Albert, C. Meier, T. Wagner, M. Tiemann, *Stimulation and Enhancement of Near-Band-Edge Emission in Zinc Oxide by Distributed Bragg Reflectors*, Advanced Materials Interfaces **2022**, 9, 2102357, DOI: 10.1002/admi.202102357.

2. M. J. Grotevent, Y. Lu, T. Šverko, M.-C. Shih, S. Tan, H. Zhu, T. Dang, J. K. Mwaura, R. Swartwout, F. Beiglböck, L. Kothe, V. Bulović, M. G. Bawendi, *Additive-Free Oxidized Spiro-MeOTAD Hole Transport Layer Significantly Improves Thermal Solar Cell Stability*, Advanced Energy Materials **2024**, 2400456, DOI: 10.1002/aenm.202400456.

3. L. Kothe, J. Klippstein, M. Kloß, M. Wengenroth, M. Poeplau, S. Ester, M. Tiemann, *Oxygen-dependent Photoluminescence and Electrical Conductance of Zinc Tin Oxide (ZTO): A Modified Stern-Volmer Description*, ChemPhysChem **2025**, 26, e202400984, DOI: 10.1002/cphc.202400984.

4. L. Kothe, M. Kloß, T. Wagner, M. Wengenroth, M. Poeplau, S. Ester, M. Tiemann, *Temperature Studies of Zinc Tin Oxide Photoluminescence for Optical O_2 Sensing*, The Journal of Physical Chemistry C **2025**, 129, 9239-9245, DOI: 10.1021/acs.jpcc.5 c01678.

5. M. J. Grotevent, L. Kothe, Y. Lu, C. Krajewska, M.-C. Shih, S. Tan, M. Tiemann, M. G. Bawendi, *Non-toxic and rapid chemical bath deposition for SnO_2 electron transporting layers in perovskite solar cells*, Chemistry of Materials **2025**, (submitted)

Talks

- L. Kothe, S. Ester, M. Poeplau, M. Wengenroth, M. Tiemann, *Stabilisierung von O_2-sensitiven Photolumineszenzsignalen durch Temperaturvariation*, GMA/ITG Fachtagung Sensoren und Messsysteme, Nuremberg, June 12, 2024

Poster Presentations

1. L. Kothe, S. Amrehn, D. Klawinski, D. Rengel, X. Wu, T. Wagner, *Making Gas Reactions Visible: Broadbend Gas Transducers Based on Photonic Crystals*, Material Science and Engineering, Darmstadt, September 26-28, 2018

2. D. Rengel, X. Wu, L. Kothe, X. Zhang, S. Amrehn, T. Wagner, *Gas Sensors based on metal oxide photonic crystals: The role of free carrier absorption*, SPIE NanoScience + Engineering, San Diego (USA), August 11-19, 2019

3. L. Kothe, S. Amrehn, T. Wagner, M. Tiemann, *Selection of ZnO Photoluminescence by Distributed Bragg Reflectors Based on Low-ϵ Porous Silica*, 8th Conference of the Federation of the European Zeolite Association, Brighton (UK), July 4-7, 2021

Abstract

Optoelectronic components manifest a dual capacity: they are capable of generating radiation from charge carriers and converting radiation into charge carriers. A critical component of these technologies is the incorporation of transparent conducting oxides.

The present work is focused on the synthesis and characterization of tin oxide-based materials. The optical and electronic properties can be tailored to a specific application through the process of doping with other elements or mixing with other oxides. The recombination of charge carriers is a key factor that determines the functionality of the material under consideration.

In the context of photoluminescence sensing it was found that the recombination of charge carriers is significantly accelerated by the presence of O_2 and an increase in temperature. The interaction of metal oxides with O_2 can be described using the principles of resistive semiconductor gas sensing. The majority of established luminescence sensors are based on metal-organic compounds. In the present work, both models are compared.

In the area of solar cell research, the suppression of the recombination of charge carriers is imperative for achieving high power conversion efficiency. Perovskite solar cells are considered to be among the most promising technologies. The absorption of light leads to the generation and separation of charge carrier pair, which are subsequently separated by polarity at the adjacent charge transporting layer. The objective of this study is to optimize the electron transporting layer.

Kurzfassung

Optoelektronische Komponenten können aus Ladungsträgern Strahlung erzeugen und diese in Ladungsträger umwandeln. Ein wesentlicher Aspekt dieser Technologien ist die Verwendung von transparenten, leitenden Metalloxiden.

Der Fokus dieser Arbeit liegt auf der Synthese und Charakterisierung von Zinnoxid-basierten Materialien. Die optischen und elektronischen Eigenschaften können durch Dotierung mit anderen Elementen oder Mischung mit weiteren Oxiden auf die jeweilige Anwendung abgestimmt werden. Die Rekombination der Ladungsträger hat einen wesentlichen Einfluss auf die Funktionalität des jeweiligen Materials.

Im Rahmen der Photolumineszenz-Sensorik wurde festgestellt, dass die Rekombination der Ladungsträger durch die Anwesenheit von O_2 sowie eine Erhöhung der Temperatur beschleunigt wird. Die Wechselwirkung von Metalloxiden mit O_2 kann mit den Prinzipien der resistiven Halbleitergassensorik beschrieben werden. Etablierte Lumineszenzsensoren basieren in der Regel auf metallorganischen Verbindungen. Im Rahmen der vorliegenden Arbeit erfolgt eine Gegenüberstellung der beiden Modelle.

In Solarzellen ist die Unterdrückung der Rekombination von Ladungsträgern von entscheidender Bedeutung für einen hohen Wirkungsgrad. Perovskit-Solarzellen werden als eine der vielversprechendsten Technologien angesehen. Die Absorption von Licht führt zur Erzeugung von Ladungsträgerpaaren, welche anschließend an der benachbarten Ladungstransportschicht je nach Polarität getrennt werden. Der Fokus dieser Arbeit liegt auf der Optimierung der elektronentransportierenden Schicht.

Contents

List of Abbreviations & Acronyms

General Abbreviations

A_N	nucleophilic addition
APCVD	atmospheric pressure chemical vapor deposition
CBD	chemical bath deposition
CVD	chemical vapor deposition
DOI	digital object identifier
EA	ethylammonium
EDX	energy dispersive X-ray spectroscopy
EELS	energy electron loss spectrocopy
ETL	electron transporting layer
FA	formamidinium
FF	fill factor
FTO	fluorine-doped tin(IV) oxide
HOMO	highest occupied molecular orbital
HTL	hole transporting layer
IC	internal conversion
ISC	intersystem crossing
ITO	indium tin oxide
LED	light-emitting diode
LUMO	lowest unoccupied molecular orbital

MA	methylammonium
MOF	metall-organic framework
PCE	power conversion efficiency
PL	photoluminescence
PXRD	X-ray powder diffraction
PSC	perovskite solar cell
PVD	physical vapor deposition
PTAA	poly(triaryl amine)
SEM	scanning electron microscopy
S_N	nucleophilic substitution
TEM	transmission electron microscopy
TCO	transparent conducting oxide
TCSPC	time-correlated single photon counting
UV/VIS	ultraviolet and visible spectral range
ZTO	zinc tin oxide

Formula Symbols

β	bimolecular recombination coefficient
β_{nr}	nonradiative bimolecular recombination coefficient
$\beta_{[O_2]}$	bimolecular recombination coefficient in O_2 presence

β_r	radiative bimolecular recombination coefficient
δ	dispersion factor
$^1\Delta_g$	neutrally charged singlet excited state of O_2
e	Euler's number
E_A	acceptor level
E_{act}	activation energy
E_C	conduction band
E_D	donor level
E_F	Fermi level
E_G	band gap energy
E_V	valence band
f_a	accessible fraction of center a
f_j	accessible fraction of center j
I	current or PL intensity
I_0	PL intensity at $t = 0$
I_{MP}	maximum power current
$I_{[O_2]}$	PL intensity in O_2 presence
I_{SC}	short circuit current
$I(t)$	time dependent PL intensity
$I(T)$	temperature dependent PL intensity
$I(T = 0K)$	PL intensity at $T = 0$ K

J	current density
γ	summary of bimolecular recombination coefficients
k_B	Boltzmann's constant
k_{ic}	rate constant of internal conversion
k_{isc}	rate constant of intersystem crossing
k_{nr}	rate constant of nonradiative transition
k_q	bimolecular quenching constant
k_r	rate constant of radiative transition
K_{SV}	Stern-Volmer constant
K_{SV}^a	Stern-Volmer constant of center a
K_{SV}^j	Stern-Volmer constant of center j
λ_{ex}	excitation wavelength
M	metal
$[O_2]$	O_2 concentration
P_{in}	input power
P_{ideal}	ideal power
P_{MP}	maximum power point
$^1\Sigma_g^+$	positively charged singlet excited state of O_2
$^3\Sigma_g^-$	triplet ground-state of O_2
S_0	ground-state

S_1	first excited state
S_2	second excited state
τ	lifetime
τ_0	lifetime at $[O_2] = 0$
τ_b	bimolecular lifetime
τ_m	monomolecular lifetime
$\tau_{m,nr}$	monomolecular nonradiative lifetime
$\tau^S_{m,nr}$	monomolecular nonradiative lifetime of singlet state
$\tau_{m,[O_2]}$	monomolecular lifetime in O_2 presence
$\tau^T_{m,nr}$	monomolecular nonradiative lifetime of triplet state
$\tau_{m,r}$	monomolecular radiative lifetime
$\tau^S_{m,r}$	monomolecular radiative lifetime of singlet state
$\tau^T_{m,r}$	monomolecular radiative lifetime of triplet state
$\tau_{[O_2]}$	lifetime in O_2 presence
t	time
T	temperature
T_1	triplet state
V	voltage
V_{OC}	open circuit voltage
V_{MP}	maximum power voltage

Molecular Formulas

CH_4	methane
CuI	copper(I) iodide
CO	carbon monoxide
CO_2	carbon dioxide
Cu_2O	copper(I) oxide
CuO	copper(II) oxide
HCl	hydrochloric acid
H_2O	water
H_2S	hydrogen sulfide
In_2O_3	indium(III) oxide
$Na_2SnO_3{\cdot}3\ H_2O$	sodium stannate trihydrate
NiO_x	nickel(II) oxide
NO	nitrogen monoxide
$^1O_2$	singlet oxygen
O_3	ozone
$Ru(bipy)_3$	Tris(2,2'-bipyridine)ruthenium(II)
$Ru(dpp)_3$	Tris(4,7-diphenyl-1,10-phenanthroline)ruthenium(II)
$Ru(phen)_3$	Tris(1,10-phenantroline)ruthenium(II)
SiO_2	silicon(IV) oxide
$SnCl_2{\cdot}2\ H_2O$	tin(II)chloride dihydrate

$SnCl_4 \cdot 5\ H_2O$	tin(IV)chloride pentahydrate
SnO	tin(II) oxide
SnO_2	tin(IV) oxide
$Sn(O^tBu)_4$	tin(IV) tetra-*tert*-butoxide
Spiro-MeOTAD	2,2',7,7'-Tetrakis(N,N-di-p-methoxyphenylamino)-9,9'-spirobifluorene
TiO_2	titanium(IV) oxide
ZnO	zinc(II) oxide
Zn_2SnO_4	zinc tin oxide

1 Outline

Optoelectronic applications accompany us frequently in our everyday lives. Microelectronics, light-emitting diodes (LEDs), displays, and solar cells are already well-established technologies. The development of innovative materials for sustainable technologies is not only relevant for research, but also for society. In particular, luminescent, transparent conducting oxides are important components in many of these fields. The industrially relevant compounds are based on earth-abundant elements like titanium, tin and zinc.[1]

In this thesis the focus is on the charge carrier recombination, which is a central aspect of the functionality of these materials. In order to promote recombination, chemisorbing gases can be introduced or the operating temperature can be increased. To prevent recombination, charge separation of electrons and holes must be as effective as possible. Here, tin-based oxides are adjusted to explore the respective problems. On the basis of two optoelectronic applications, strategies to promote and prevent charge carrier recombination are investigated, see Figure 1.

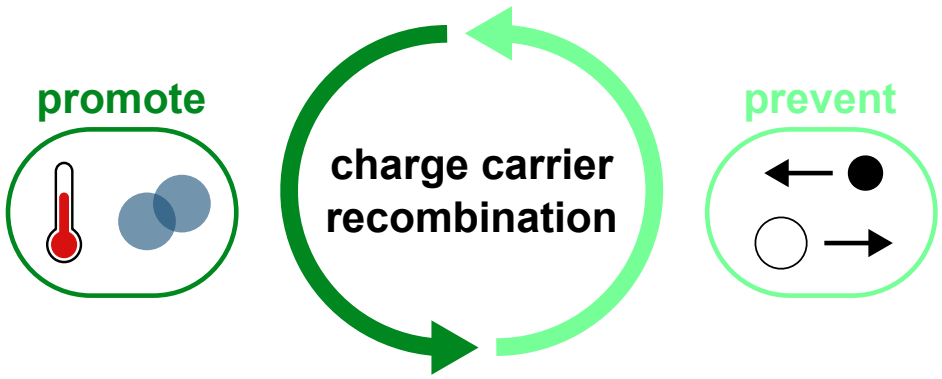

Figure 1: Schematic overview of strategies to promote or prevent charge carrier recombination.

1.1 Gas Sensing

Metal oxides can be used as chemiresistive or optical sensors. They are well-established as resistive gas sensors. However, harsh measurement conditions or elevated operating temperatures may initially damage electrical components of the sensor before affecting the sensing material. Consequently, optical methods are becoming increasingly attractive due to their ability to separate electrical components and sensing materials, thereby unveiling novel contactless sensing applications. The interaction of metal oxides with gases alter the material reversibly as electrons are introduced or removed. This can be measured as a change of *e.g.* conductance, permittivity or photoluminescence (PL).[2–4]

In this work the focus is on the detection of PL. In the presence of oxygen (O_2) the emission intensity and lifetime are both quenched, so the charge carrier recombination is promoted. Commercially available PL gas sensors are based on metal-organic compounds. They exhibit great sensing properties, but are quite sensitive to radiation.[5] In contrast, metal oxides are more promising in terms of photostability. The emission lifetime of binary oxides can be very short (ps to ns), which is difficult to detect with a simple setup. Therefore a ternary system with a much longer lifetime was chosen. Zinc tin oxide (Zn_2SnO_4, ZTO) stands out with a defect-based emission in the visible spectrum with a lifetime in the ms range.[6,7] It is a mixed metal oxide based on zinc(II) oxide (ZnO) and tin(IV) oxide (SnO_2) with a wide band gap (*ca.* 3.6 eV) in the UV range. The models to describe PL sensing are typically about (metal-)organic compounds in a liquid. The interaction of O_2 with the surface of a metal oxide is described with the models for semiconductor gas sensing. Therefore, adjusting and refining the models is necessary for a better understanding of PL sensing with metal oxides.

The operating temperature is a central parameter in both models and provides further insight into the sensing mechanism. With increasing operating temperature the PL intensity and lifetime are also quenched, so the charge carrier recombination is further promoted. Investigating the concentration dependence of simultaneously measured PL intensity and conductance reveals the incomplete gas accessibility and a non-linear relation of both measurands.[8] Studies about the temperature quenching contribute to a better understanding of ZTO's interaction with O_2.[9]

1.2 Solar Cells

Solar cells are becoming increasingly important in our everyday lives. They are multilayer systems, where each layer has a specific function. Classic systems are based on silicon and have dominated the market for over 40 years. In the last two decades the efficiency of silicon cells stagnated around 27 %.[10,11] The efficiency of a single solar cell is physically restricted by the Shockley–Queisser limit, which predicts a maximum efficiency of *ca.* 30 %.[12] Currently III-V multijunction systems achieve efficiencies of nearly 50 %, but are used just in military or aerospace fields due to high production costs.[13] New technologies are *e.g.* dye-sensitized or quantum dot cells, yet perovskite solar cells (PSCs) are by far the most promising. In less than 15 years of research PSCs reached an efficiency of 27 % as single cells and 30 % in tandem setups.[10]

A PSC typically consists of five layers: Anode on a substrate, electron transporting layer (ETL), perovskite layer, hole transporting layer (HTL) and cathode. The perovskite layer is the photoactive layer, where electrons and holes are generated. The PSC is illuminated through the substrate, which requires the anode and ETL to be transparent. Fluorine-doped SnO_2 (FTO) or tin-doped indium(III) oxide (ITO) coated glass substrates provide the basis

as anodes.[14] SnO_2 ETLs are very common as low process temperatures are required, the band alignment is quite favorable and the photodegradation of the perovskite layer is comparably small.[15]

Within the scope of this thesis a new SnO_2 ETL synthesis is presented. ETLs are required to exhibit excellent electron transport behavior to extract electrons from the perovskite layer and to block holes. The recombination of charge carriers is prevented by effective charge separation, which is manifested in the efficiency of the solar cell. SnO_2 ETLs can be prepared either by spin-coating nanoparticles or by directly growing a layer on the substrate surface. Industrially the application of nanoparticles is more interesting as spin-coating is fast and easy to scale up. Established methods to grow SnO_2 layers on FTO require several hours, but higher efficiencies are achieved. Therefore there is a need to develop a fast SnO_2 layer deposition (< 10 min). Fast coating not only makes PSCs more accessible for industrial production, but also simplifies processing in the laboratory, as the application of this layer is the speed-determining step. The presented synthesis reduces the reaction time from 12 h to 6 min by replacing several harmful chemicals with one non-toxic salt.[16]

2 Theoretical Background

2.1 Transparent Conducting Oxides

Indium(III) oxide (In_2O_3), tin(IV) oxide (SnO_2), titanium(IV) oxide (TiO_2) and zinc(II) oxide (ZnO) are the most common transparent conducting oxides (TCOs). Each oxide, either pure, doped or as a mixed oxide, is industrially important.[1,17] SnO_2 is a central component in both solar cells and gas sensors.[12,18] ZnO is also frequently used as a gas sensing material, but also exhibits interesting photoluminescence properties.[12,19] Zinc tin oxide (Zn_2SnO_4, ZTO), which is the mixed metal oxide of SnO_2 and ZnO, shows favorable photoluminescence properties compared to the pure oxides.[20]

2.1.1 Tin Oxide

Tin can either form tin(II) oxide (SnO) or tin(IV) oxide (SnO_2) with oxygen. SnO is metastable and disproportionates at elevated temperatures to SnO_2 and Sn.[21] SnO_2 is one of the most frequently used n-type (electron conduction) metal oxides, due to its outstanding optical and electrical properties. The wide optical band gap (*ca.* 3.6 eV - 4.0 eV) ensures a high transmittance in the in the visible spectrum.[22] A natural high electron mobility is based on a uniform distribution of electron charge density and low scattering of the conduction electrons.

SnO_2 crystallizes in the tetragonal Rutile-type structure (Figure 2). Sn atoms (pink) are octahedrally surrounded by O atoms (dark blue) and octahedrons are corner-connected.[23] Missing O-atoms provide n-type semiconducting behavior.[24] Formally, the oxygen deficit allows coexistence of Sn^{4+}- and Sn^{2+}-ions and enhances the electron mobility.[25] In contrast, SnO exhibits p-type (hole conduction) character, which is highly affected by the available O_2 content and synthesis temperature.[26]

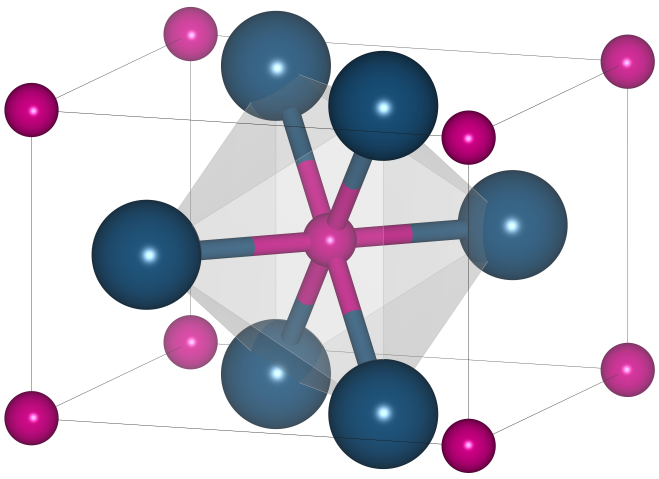

Figure 2: Rutile-type crystal structure of SnO_2. Tin atoms are pink and oxygen atoms are dark blue.[27]

SnO_2 can be synthesized by various concepts, depending on the aimed application. For powder samples, wet-chemical synthesis approaches[28] are as suitable as methods based on mechanochemistry[29] or solid-state reactions.[30] Sol-gel chemistry allows the formation of thin layers, nanoparticles or powders.[31]

A sol consists of solid particles in a size range from 1 to 1000 nm, dispersed in a liquid phase. Thus a sol is a suspension or a colloidal solution. Between the particles van der Waals attraction and surface charges are the dominant forces. Starting with inorganic salts or alkoxides, the formation of colloid particles is based on two different reactions: hydrolysis and condensation. Tin salts for synthesis of tin oxides are *e.g.* $Sn(II)Cl_2 \cdot 2\ H_2O$,[32] $Sn(IV)Cl_4 \cdot 5\ H_2O$,[33] $Sn(O^tBu)_4$[34] or $Na_2SnO_3 \cdot 3\ H_2O$.[35] As solvents water or alcohols can be used.[36]

In aqueous solutions the metal salts are solvated and hydrolized. An equilibrium is established between the aquo, hydroxido and oxido species (Equation 1).[36]

$$[M(OH_2)]^{z+} \rightleftharpoons [M-OH]^{(z-1)+} + H^+ \rightleftharpoons [M=O]^{(z-2)+} + 2H^+ \tag{1}$$

M-(OH_2)	M-OH	M=O
Aqua	Hydroxo	Oxo

Depending on the metal M, additional ligands and pH value, the equilibrium is set. Esterification occurs in alcoholic solutions. Hydrolyzed or esterified groups can condensate *via* a nucleophilic substitution (S_N) (Equation 2).[36]

$$M_1 - OX + M_2 - OY \longrightarrow M_1 - \overset{\overset{X}{|}}{O} - M_2 + OY \tag{2}$$

If the metal ion is coordinatively unsaturated, a nucleophilic addition occurs (A_N) (Equation 3).[36]

$$M_1 - OX + M_2 - OY \longrightarrow M_1 - \overset{\overset{X}{|}}{O} - M_2 - OY \tag{3}$$

Since the pH value determines which species is dominant, it also controls the reaction rate of hydrolysis and condensation. The type of reaction determines the particle size.[36]

The perpetual condensation creates growing clusters until a continuous solid network is formed: a gel. An abrupt increase in viscosity occurs and the often clear, colorless sol turns turbid, which indicates cluster growth. The pores of the gel are filled with the solvent, which can be extracted by supercritical drying to form aerogels[37,38] or be evaporated to form xerogels,[39] which no longer exhibit a porous structure.[36]

The deposition of a thin-layer is easy to adapt for an industrial setup. Typically a sol is spin-,[40] dip-[41] or blade-coated,[42] followed by a thermal conversion. Already prepared (nano)particles can be dispersed and printed like an ink.[43,44] Layers can also be grown directly on a substrate by chemical vapor deposition (CVD)[45] or chemical bath deposition (CBD).[15] In contrast to other TCOs a solution-based deposition is preferred for SnO_2, as the raw materials are inexpensive, easy to process and scale up.[17] Figure 3 summarizes the mentioned methods.

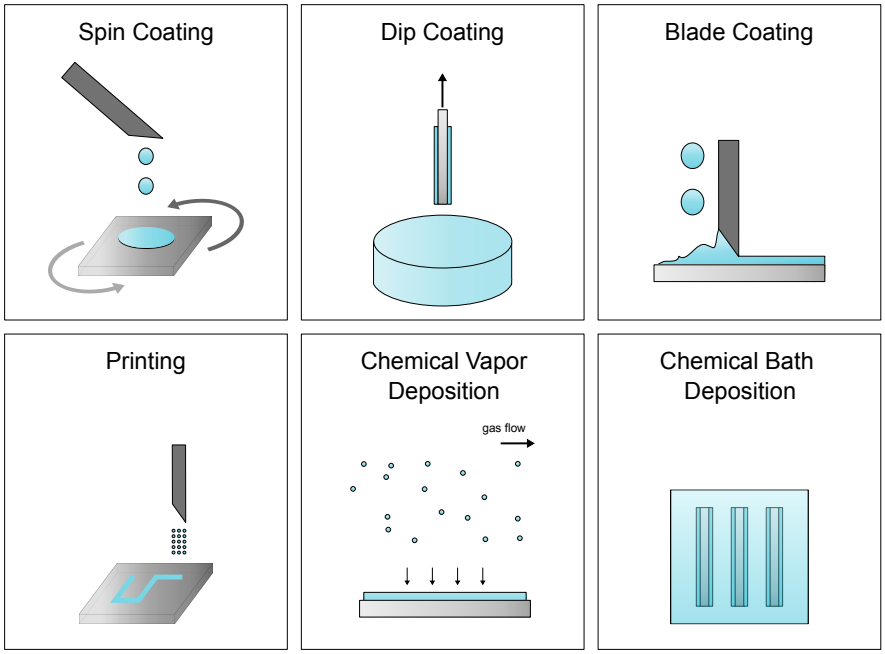

Figure 3: Methods for thin-layer deposition.

Frequent applications of SnO_2 can be attributed to its electron transportation behavior and transparency. The areas of application can be divided into the fields of *microelectronics*, *environmental decontamination*, *energy production*, and *energy storage* (Figure 4).[46] In microelectronics SnO_2 thin-layers are used as transistors[47,48] or capacitors.[49,50] SnO_2 is the most used metal oxide in gas sensing. It can detect gases like CH_4, CO or H_2 and its interaction with O_2 is well understood.[51–53] As a photocatalyst it can degrade organic pollutants[54,55] or participate in water-splitting to generate H_2.[56,57] In future-oriented energy production fields like solar[58,59] or fuel cells[60,61] SnO_2 can be used to transport the generated electrons or protons. SnO_2 is also of interest for energy storage as an electrode material in batteries.[62,63]

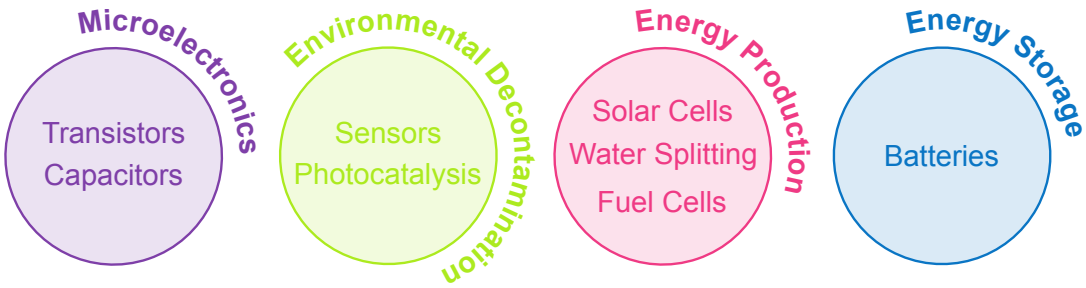

Figure 4: Applications of SnO_2.

Dopants are frequently introduced to SnO_2 to improve its properties, such as electron mobility.[22] SnO_2 is mostly doped with fluorine (fluorine-doped tin(IV) oxide, FTO), which generates an electron excess due to the lower valency of F^- compared to O^{2-}. Optimal doping concentrations vary in the literature, whereas 2 at% seems to be the common concentration.[64,65] The SnO_2 crystal structure is not distorted due to F-doping, since ionic radii of F^- ($R_{F^-} = 1.33$ Å) and O^{2-} ($R_{O^{2-}} = 1.32$ Å) are comparribly similar.[66] Commercially available FTO is deposited on glass substrates *e.g.* by atmospheric pressure chemical vapor deposition (APCVD).[67]

Other dopants may be (transition) metals with the same or lower valency than Sn^{4+}, which may affect the conduction type (n-type or p-type). The conduction types will be discussed in more detail in subsubsection 2.2.2. Table 1 displays examples of dopants and their effect on the conduction type.

Table 1: Examples of SnO_2 dopants.

doping type	dopant
n-type	F[64–66], Nb[68], W[68]
isovalent	Ti[68]
p-type	Al[68], B[69], Cd[68], In[70], Li[68], Ni[71], Sb[72]

2.1.2 Mixed Transparent Conducting Oxides

The commercially most relevant mixed TCO is tin-doped In_2O_3 (indium tin oxide, ITO).[17] Sn is soluble in the In_2O_3 lattice with an amount up to 6 at% without causing any lattice distortion. Usually ITO contains *ca.* 10 at%, which results in a mixed phase.[73,74] ITO is used as an electrode material in solar cells, displays or touchscreens, and is required to be recycled as indium is considered a rare element.[75–77]

Zinc tin oxide (Zn_2SnO_4, ZTO) is a mixed metal oxide, with a stoichiometry of SnO_2 and 2 ZnO. This n-type semiconductor has an optical band gap of *ca.* 3.6 eV, which ensures a high transparency in the visible spectrum, and exhibits high electron charge transport behavior. The abundance of Sn and Zn makes ZTO an interesting alternative for established TCOs. In comparison with pristine SnO_2, the ternary composition allows more degrees of freedom to adjust the Sn:Zn ratio for a precise property engineering.[6]

ZTO crystallizes as the inverse spinel type (Figure 5).[78] The inverse spinel structure is characterized by corner-sharing MO_4 tetrahedra and MO_6 octahedra. One half of the Zn^{2+}-ions occupy tetrahedral and the other half octahedral sites, while all Sn^{4+}-ions occupy octahedral sites. Conventionally, a random distribution of Zn^{2+}- and Sn^{4+}-ions within the octahedral sites has been considered.[79,80] DFT calculations indicate that Sn^{4+}-ions order along the [110] direction, leading to the formation of Sn-Sn chains.[81] The overlap of unoccupied s-orbitals of the cations may result in the formation of electron highways.[82]

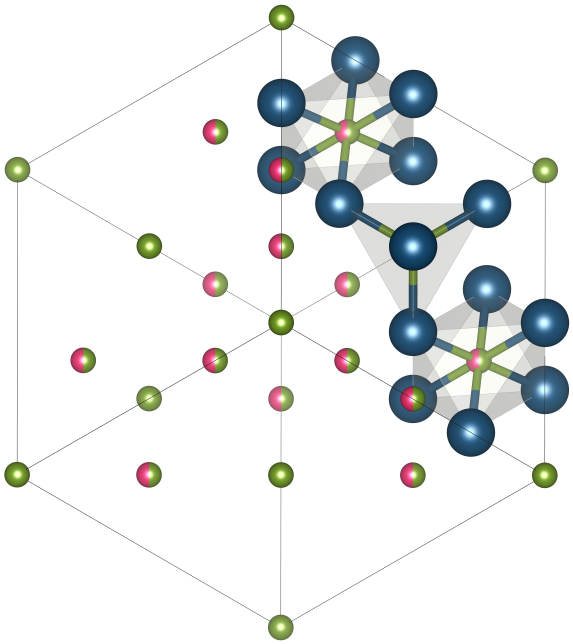

Figure 5: Inverse spinel type crystal structure of Zn_2SnO_4. Tin atoms are pink, zinc atoms are green and oxygen atoms are dark blue.[83]

The synthesis of ZTO is very versatile. The easiest synthesis is a solid-state reaction of SnO_2 and ZnO (1:2) to ZTO at temperatures above 800 °C.[84–86] Solvothermal[20,87,88] or sol-gel-based[89,90] syntheses are primarily used. Low-temperature approaches are also investigated and can either result in the phase-pure ZTO[91] or introduce only Sn[92] or Zn[93,94] into the lattice.

Thin-layer preparation and applications of ZTO are very similar to SnO_2. ZTO thin-layers are prepared *e.g.* by sputtering,[95,96] spin-coating,[97,98] CVD[99] and printing techniques.[100,101] In microelectronics the common use for ZTO are transistors.[102,103] Compared to pristine SnO_2, foremost photocatalytic applications,[87,104,105] including water splitting,[106,107] are much more common for ZTO. Solar cells,[108–110] batteries[111,112] and gas sensors[113–115] are also central applications of ZTO.

2.2 Optical O_2 Sensing

Optical measurement methods enable contactless detection of gases, which opens up new areas of application. Since oxygen (O_2) is not only essential for our survival, but also plays an important role in various areas of life or industrial applications, its detection is a central point of gas sensor technology. In biological systems O_2 is a generic marker that contains a lot of information, for instance about viability or metabolic status.[116] Monitoring the atmospheric composition is also a wide application field, which includes monitoring of food packaging,[117] exhaust gases[118] or air quality.[119,120] Commercially relevant O_2 sensors are *e.g.* the Clark electrode[121] or zirconia-based sensors,[122] both of which are based on electrochemical principles.

O_2 can be detected optically either by absorption or luminescence. In this work the focus is on luminescence sensing. Here, the presence of O_2 reduces the intensity and lifetime of the emission. It is quenched.[123,124] Suitable materials for luminescence-based O_2 sensors can be organic molecules,[125] metal-organic compounds,[125] metal-organic frameworks (MOFs)[126] or luminescent inorganic (nano)materials.[127] Organic and metal-organic compounds can be used both in solution and as solid-state sensors. MOFs and inorganic (nano)materials can only be applied as solid-state sensors.[5]

2.2.1 Metal-Organic Compounds

Metal-organic compounds are the most frequently used in luminescence-based O_2 sensors and are commercially available.[121] Commonly used metal-organic compounds are Ru(II) complexes like Ru(bipyridine)$_3$ (Ru (bipy)$_3$, Figure 6a), Ru(1,10-phenantroline)$_3$ (Ru(phen)$_3$, Figure 6b) or Ru((4,7'-diphenyl-1,10'-phenanthroline)$_3$ (Ru(dpp)$_3$, Figure 6c). By introducing additional functional groups, the luminescence properties are further refined.[5,128]

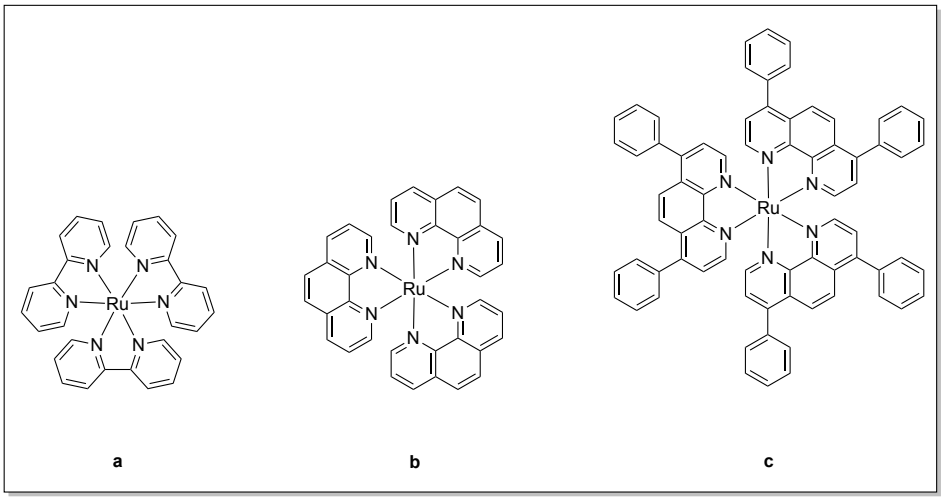

Figure 6: **a** Ru(bipy)$_3$, **b** Ru(phen)$_3$ and **c** Ru(dpp)$_3$.

Though the Ru(II) complexes are the most prominent compounds, the complexes of many other transition metals like Ir(III),[129] Os(II),[130] Pt(II)[131] or Pd(II)[131] are suitable for O_2 detection as well.

The photoluminescence (PL) process of a luminophore and interaction with O_2 can be described *via* a Perrin-Jabłoński diagram (Figure 7). The absorption of radiation elevates electrons from the ground-state (S_0) to the first or second excited state (S_1 or S_2). Regardless of which excited state the electrons enter, they vibronically relax to the lowest energy level of S_1. The electrons from S_2 get through internal conversion (IC, k_{ic}) to S_1. Both vibronic relaxation and IC are nonradiative transitions. From S_1 electrons can relax to S_0 *via* radiative (k_r^S) or nonradiative transitions (k_{ic}^S). This phenomenon is called *fluorescence*. By intersystem crossing (ISC, k_{isc}) electrons can also undergo a spin-forbidden transition to the triplet state (T_1), which is less probable hence less intense. From T_1 electrons can also relax to S_0 radiatively (k_r^T) and nonradiatively (k_{nr}^T), which is called *phosphorescence*. The phosphorescence is considerably longer than fluorescence. The presence of heavy atoms promotes the ISC between S_1 and T_1 due to spin-orbit interaction and can enhance the phosphorescence intensity and decrease the lifetime. Both fluorescence and phosphorescence contain less energy than the absorbed light (Stokes' shift).[125,132]

In the presence of triplet O_2 static or dynamic PL quenching can occur. During static PL quenching, the luminophore forms a nonradiating complex with the quencher molecule, which results in a decrease in PL intensity, but not in lifetime. In case of dynamic quenching, both the PL intensity and lifetime are affected by the quencher. Collisions between the luminophore and the quencher can cause an exchange of energy or electrons.[125,133] The exact mechanism is not yet completely understood, but an energy transfer mechanism is suggested. The ground-state molecular O_2 is in the triplet state ($^3\Sigma_g^-$), which can be excited to a highly reactive neutral ($^1\Delta_g$) or positively charged ($^1\Sigma_g^+$) singlet state. The collision may cause O_2 to get into the $^1O_2$ state, while the ISC between S_1 and T_1 of the luminophore is promoted.[125,132]

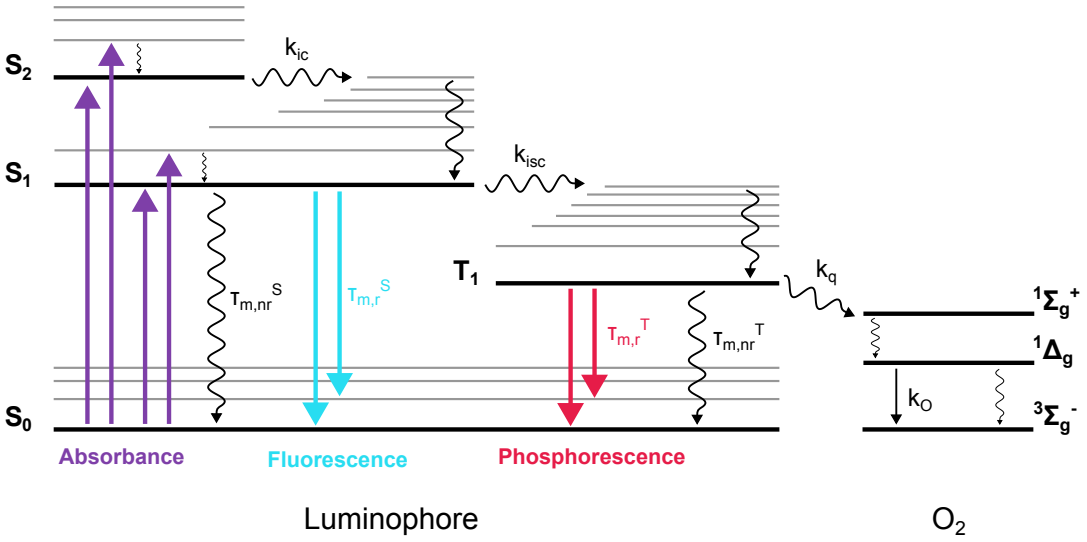

Figure 7: Perrin-Jabłoński diagram of a luminophore interacting with O_2. Adapted from Quaranta *et al.*.[125]

The lifetime τ_m of fluorescence or phosphorescence contains both the radiative $\tau_{m,r}$ and nonradiative $\tau_{m,nr}$ lifetime (Equation 4).[127,134]

$$\frac{1}{\tau_m} = \frac{1}{\tau_{m,r}} + \frac{1}{\tau_{m,nr}} \tag{4}$$

The index m specifies the validity for monomolecular cases. The reciprocal lifetimes are called recombination rates. The collective lifetime is dominated by the transition with the highest recombination rate and thus the shortest lifetime.[127,134]

In the presence of O_2 an additional nonradiative path is introduced. For the lifetime, this means that a further recombination rate ($\frac{1}{\tau_{m,[O_2]}}$) is added, which is dependent on the O_2 concentration $[O_2]$. With increasing O_2 concentration this path becomes more probable as more collisions occur. Equation (4) is extended to Equation (5).[127,132,134]

$$\frac{1}{\tau_m} = \frac{1}{\tau_{m,r}} + \frac{1}{\tau_{m,nr}} + \frac{1}{\tau_{m,[O_2]}} \cdot [O_2] \tag{5}$$

In practice, the lifetime can be determined by exciting the material and deactivating the light source. For lifetimes ranging from µs to s, straightforward configurations equipped with a mechanical shutter can reliably deliver the lifetime. In order to measure lifetimes in the fs to ns range, it is necessary to employ time-correlated single photon counting (TCSPC) or a streak camera.[134–136] In the context of O_2 sensors, lifetimes in the µs to ms range are optimal due to the simple detection process. The subsequent decay behavior, known as the afterglow of the emission, is often characterized by a single exponential decay, as demonstrated in Equation (6). The intensity at $t = 0$ is I_0, t denotes the time and $\tau_{m,[O_2]}$ stands for the lifetime at the corresponding O_2 concentration.[127,132]

$$I(t) = I_0\, e^{-\frac{t}{\tau_m}} \tag{6}$$

The lifetime is defined as the time of intensity decay to a value of 1/e, Equation 7.

$$I(\tau_m) = I_0 \cdot \frac{1}{e} \tag{7}$$

Figure 8 illustrates the single exponential decay of the intensity in the absence and presence of O_2.

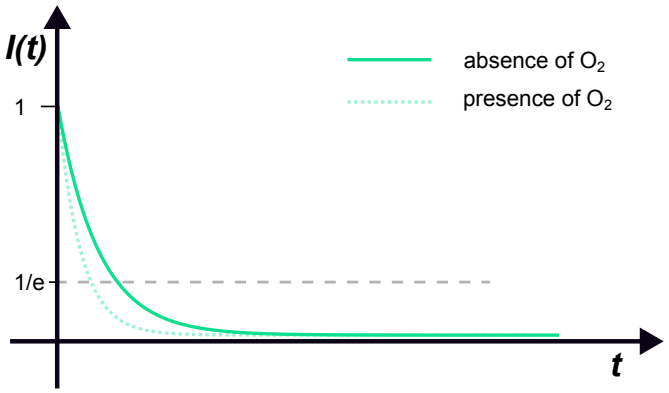

Figure 8: Exponential decay of PL intensity after deactivating the light source in the absence and presence of O_2.

For metal-organic compounds the lifetime can range from fs to µs[5,137] and can easily be engineered *e.g.* by the modification of the ligands.[138]

The kinetic of dynamic quenching is described with the Stern-Volmer Equation (Equation 8). I_0 and $I_{[O_2]}$ or τ_0 and $\tau_{[O_2]}$ are the intensities or lifetimes in the absence and presence of O_2. k_q is the bimolecular quenching constant, K_{SV} is the Stern-Volmer constant and $[O_2]$ denotes the O_2 concentration.[132]

$$\frac{I_0}{I_{[O_2]}} = \frac{\tau_0}{\tau_{[O_2]}} = 1 + k_q \tau_0 [O_2] = 1 + K_{SV}[O_2] \tag{8}$$

The intensity and lifetime are linear to the O_2 concentration (Figure 9). Stern-Volmer plots can also be generated from lifetime measurements.[139] In large molecules or solid systems, where the metal-organic compound is embedded *e.g.* in a polymer[140] or a porous matrix,[141] the luminophore may show a deviation from the linear behavior. An upwards curvature indicates, that dynamic and static quenching both occur. A downwards curvature indicates that just a fraction of luminescent centers interacts with the quencher. S. S. Lehrer first proposed a model for this case for proteins.[142] Multiple luminescence centers may be present here and, depending on the chemical environment, the centers may be differently accessible to the quencher.[132,142]

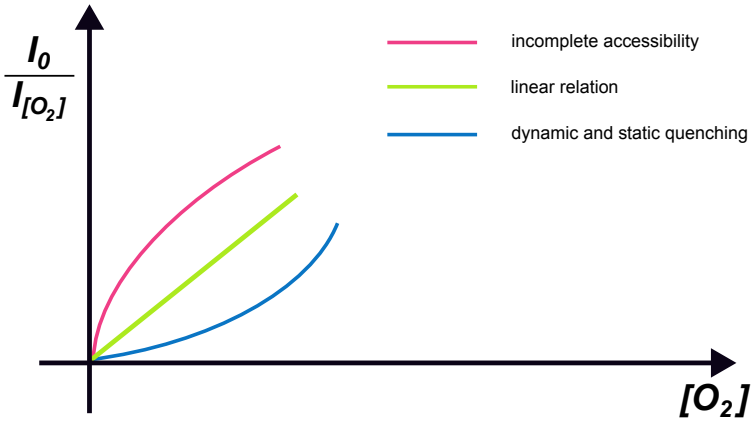

Figure 9: Deviations from the linear Stern-Volmer plot attributed to incomplete accessibility of the quencher or the coexistence of dynamic and static quenching.

In terms of incomplete accessibility, it is hypothesized that two luminescent centers are present, while only center *a* is accessible to the quencher. Mathematically the Stern-Volmer equation, Equation 8, is extended. In the modified Stern-Volmer equation f_a is the accessible fraction and K_{SV}^a the Stern-Volmer constant for center *a* (Equation 9).[132,142]

$$\frac{I_0}{I_0 - I_{[O_2]}} = \frac{1}{f_a K_{SV}^a [O_2]} + \frac{1}{f_a} \tag{9}$$

For luminophores with multiple luminescent centers that interact *via* different kinetics with the quencher Equation (10) is applicable.[143]

$$\frac{I_{[O_2]}}{I_0} = \sum_j \frac{f_j}{1 + K_{SV}^j [O_2]} \tag{10}$$

For each center an additional term can be included, whereas the sum of all f_j is 1.

Metal-organic compounds show excellent sensing properties. Excitation and emission wavelengths are usually located in the visible spectrum. O_2 concentrations below 100 ppm can be detected reliably with response times *e.g.* < 0.2 s (0.0 vol% – 0.55 vol% O_2).[144] Though the materials can be quite expensive to synthesize, just a few mg are required to fabricate a sensor. In contrast, these fast and sensitive materials have disadvantages with the long-term stability. Ru-complexes show significant photobleaching under irradiation and especially in O_2 containing environments.[145–147] $^1O_2$, which may form during collisions of the complex and O_2, damages the compounds and therefore compromises the emission intensity and lifetime in the long term.[145] Stabilization[147] or $^1O_2$ scavangers[145] may enhance the photostability.

2.2.2 Metal Oxides

Semiconducting metal oxides are already deeply established materials in the field of gas sensing (see 2.1). They are commonly used as resistive gas sensors,[51] but optical applications[4,148] have also been explored.

In a metal oxide the valence (E_V) and conduction band (E_C) are separated by an energy barrier, the band gap E_G. Unlike the highest occupied molecular orbital (HOMO) and lowest unoccupied molecular orbital (LUMO) in a molecule, these bands are not discrete, they may overlap, interact and are continuous. In E_V electrons are unable to move in the lattice. Energy absorption in form of *e.g.* thermal or photon energy excites electrons to E_C. In E_C the electrons are mobile and participate in conductance. Classical semiconductors have band gaps between 0.1 eV and 3 eV. Despite their large band gaps, many metal oxides show a significantly higher electron mobility as compared to insulators, since (un)intentional doping generates additional states in the band gap (Figure 10).[149]

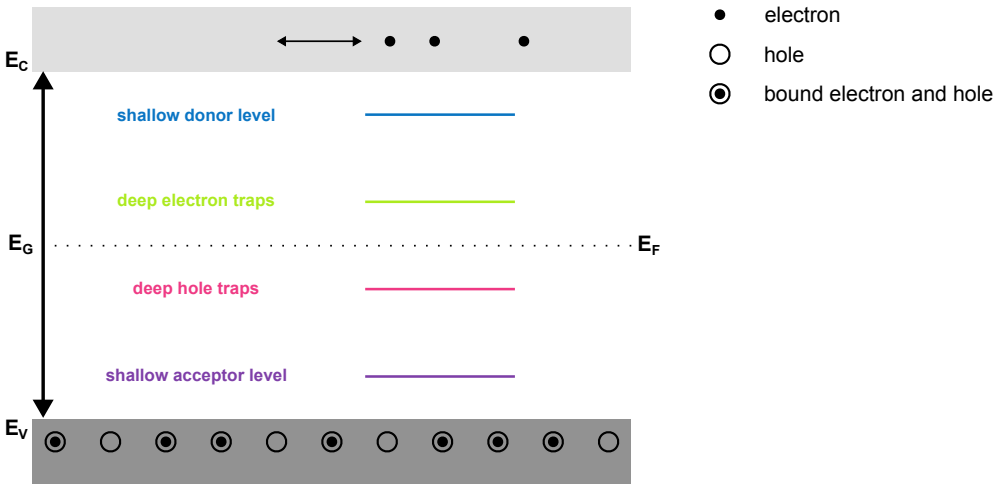

Figure 10: Simplified band scheme of a semiconductor with different defect states. Adapted from Wijesinghe *et al.*.[150]

Levels closer to E_C are electron-rich and act as donors, whereas levels closer to E_V are occupied with holes and act as acceptors. Depending on the position of these levels the Fermi level (E_F) is closer to E_C or E_V. Is E_F closer to E_C, electrons are charge carriers and the material shows *n-type* conduction. Is E_F closer to E_V, conduction is based on the movement of holes (*p-type*). In case of Si, a typical intrinsic semiconductor (E_G = 1.2 eV),[151] E_F is exactly between E_V and E_C. Doping with electron-rich or -depleted atoms shifts E_F accordingly.[152]

Metal oxides may also exhibit PL. The absorption of radiation excites electrons from E_V to E_C (Figure 11 i), when the energy of the radiation has the same or a higher energy than E_G. The excitation generates *excitons*. An exciton is a couple of an electron and a hole,

which are attracted over several lattice constants *via* Coulomb forces, and represents the lowest excited state in a semiconductor. Excitons possess a binding energy and move as a bound entity. In the case that the binding energy is overcome, both electrons and holes can move through the lattice separately. From E_C the excited electrons can relax to E_V *via* different channels. The parity selection rule defines that radiative (electromagnetic) transitions can only occur between states with a different parity. Regarding nonradiative transitions, there are three possible options. First and most often, the excess energy is released as a series of phonons, *i.e.* lattice vibrations manifesting as heat. Secondly, recombination has the potential to generate new point defects within the lattice. Thirdly, alteration of the material through photochemistry is another possibility. The band-band transition (ii) is the transition with the highest energy. Semiconductors can have a direct or indirect band gap, which further classifies the form of recombination. In case of a direct band gap the *k*-vector (crystal momentum) of excitons stays constant during the recombination. With an indirect band gap, the recombination is supported by a phonon, whereby the *k*-vector changes. The band-band transition typically occurs in direct band gap materials with high purity and is the fastest radiative transition. The described donor (E_D) and acceptor levels (E_A) within the band gap also generate luminescence centers. A donor transition (iii) is a radiative transition between E_D and E_V. An acceptor transition (iv) occurs between E_C and E_A. The donor-acceptor transition (v) is the transition with the lowest energy. Transitions *via* defect levels prolong the lifetime.[134,152]

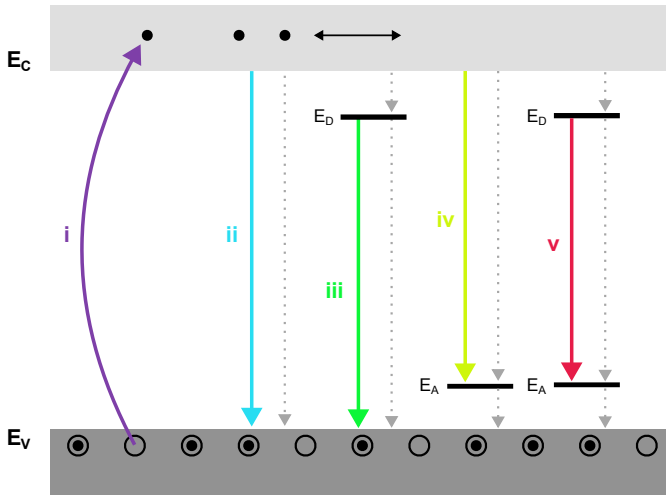

Figure 11: Band scheme with possible radiative and nonradiative transitions in a semiconductor. i Absorption, ii band-band transition, iii donor transition, iv acceptor transition and v donor-acceptor transition. Dotted lines indicate nonradiative transitions.

In real systems E_V and E_C are bent near the crystal domain surface due to defects, surface groups or disorder in the crystal lattice. In ambient air O_2, H_2O and CO_2 are present and can either physisorb or chemisorb to the surface. The chemisorbed groups can be bound quite stronger, requiring temperatures of at least 300 °C to be completely removed from the

oxide surface.[24,153,154] Figure 12 illustrates a realistic oxide surface in ambient air.

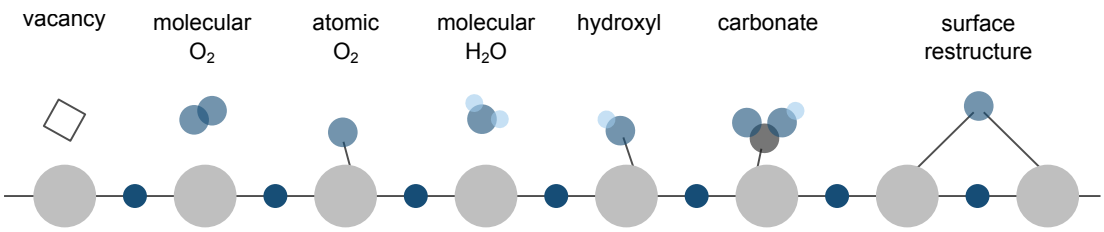

Figure 12: Illustration of real oxide surface in the presence of ambient air (O_2, CO_2 and H_2O). Adapted from Staerz *et al.*.[154]

P-type semiconductors exhibit downwards and n-type semiconductors upwards bending. Given that all metal oxides presented in this work are n-type semiconductors, only this mechanism will be described below. Figure 13 depicts an exemplary band scheme of a defect-rich n-type semiconductor under inert conditions and constant irradiation. The photon penetration depth determines the relevant region. Due to the presence of defect levels E_F is located near E_C. Electrons from E_V are excited to E_C as a consequence of absorption (Figure 13 i). Alternatively, the electrons can also be thermally activated to E_C from donor levels (Figure 13 ii). Radiative transitions originate from these levels (Figure 13 iii). The continuous irradiation generates a space-charge layer near the surface. Holes accumulate at the surface, which reduces band-bending, and electrons move into the bulk. The resulting electric field near the surface lowers the recombination rates so that there are hardly radiative transitions in this layer. Therefore, it is also called a "dead-layer".[3,153,155]

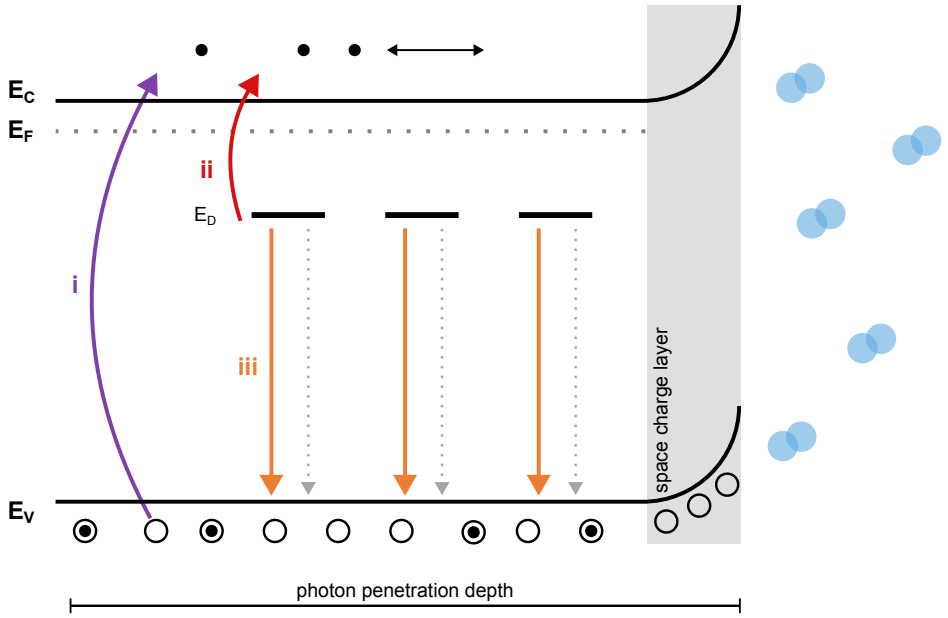

Figure 13: Band scheme of an n-type semiconductor in a pure N_2 (light blue molecules) atmosphere. Electrons can be optically i or thermally ii activated to E_C. Emission iii from E_D.

The detection mechanism of gases with metal oxides can be described with the ionosorption model. N-type semiconductors act as electron donors in the presence of O_2 due to the electron-rich defect levels. O_2 has the capacity to engage in either physisorption or chemisorption on the surface. The chemisorption of O_2 traps electrons from E_C at the surface and new nonradiative transitions are generated (Figure 14). This results in the formation of an electron depletion layer, which is analogous to the space-charge region. Hence, the space-charge region increases due to O_2 adsorption. The localization of electrons at the surface reduces the conductance, emission intensity and lifetime. E_F is lowered and band-bending increases. The position of E_F is limited by the LUMO position of O_2. If E_F and $LUMO_{O_2}$ are equal, the surface is saturated with O_2.[3,8]

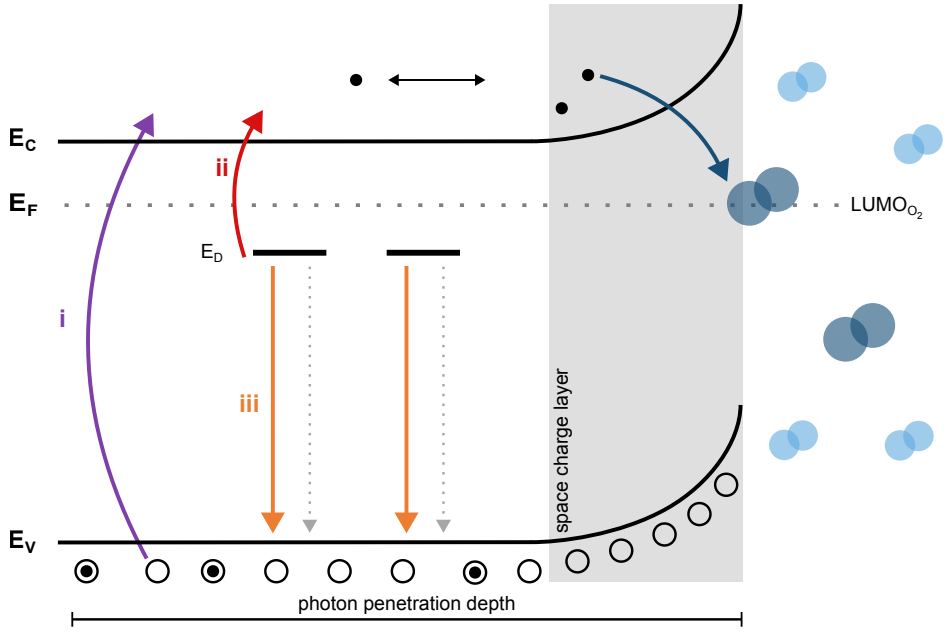

Figure 14: Band scheme of an n-type semiconductor in an O_2 containing (dark blue molecules) atmosphere. Electrons can be optically **i** or thermally **ii** activated to E_C. Emission **iii** from E_D. Increase of space charge layer and band bending, reduction of E_F and emission intensity due to O_2 adsorption.

The present O_2 species is dependent on the operating temperature. At temperatures up to 80 °C, the predominant O_2 species is the neutral O_2 molecule. The presence of a single negatively charged superoxide ion (O_2^-) is also notable. At approximately 150 °C, there is an increase in the prevalence of the superoxide species. Exceeding 200 °C, the presence of single O-ions (lattice-like, *oxide*, O^{2-}) has been reported. The temperatures described refer to SnO_2 and ZnO; it is fair to assume that a comparable situation exists for ZTO.[8] Figure 15 illustrates the potential species of O_2.

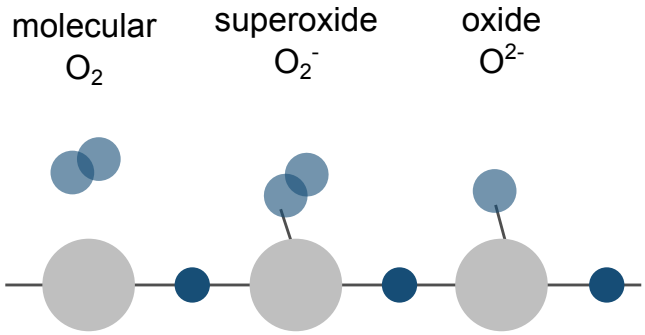

Figure 15: Potential surface adsorbed species of O_2.

For PL gas sensing the form of excitation is relevant. Electrons can also be excited directly to E_D ($E_V \rightarrow E_D$) and exhibit PL. This can be the case *e.g.* for doped insulators with high energy band gaps. The indirect excitation, *i.e.* the route *via* E_C, is required in order to detect O_2.[127]

The detection of other analytes like H_2, CO or H_2S is based on the above-described mechanism. The test gases react with the surface-adsorbed O-species. The reaction with oxidizing gases (*e.g.* O_3 or NO) results in a decrease in conductance, while the reaction with reducing gases (*e.g.* H_2 or CO) leads to an increase in conductance. This principle should also apply to PL sensing; however, the operating temperature of resistive semiconductor gas sensors typically ranges from 300 °C to 600 °C. It should be noted that for resistive gas sensing the optical activation (illumination with $\lambda_{ex} \approx E_G$) lowers the operating temperature significantly.[153,155–157]

PL is very sensitive to temperature fluctuations. With increasing temperature nonradiative transitions become more dominant and new nonradiative transitions may occur. This type of behavior is called a Schön-Klasens mechanism, where multiple radiative and nonradiative transitions are involved.[158–160] The temperature dependence of PL intensity $I(T)$ can be described with Equation (11), which is related to the Fermi-Dirac statistics.

$$I(T) = \frac{I(T = 0K)}{1 + Cexp\{-\frac{E_{act}}{k_B T}\}} \tag{11}$$

$I(T = 0K)$ is the PL intensity at 0 K, C denotes a dimensionless constant, E_{act} the activation energy, k_B Boltzmann's constant and T the temperature. E_{act} can be regarded as the ionization energy of the luminescent center. In case of an acceptor level, holes are thermally emitted to E_V. In donor levels electrons are thermally emitted to E_C. According to this model, the PL intensity remains constant at low temperatures until a critical temperature is reached. Beyond the critical temperature the PL intensity is quenched (Figure 16).[158]

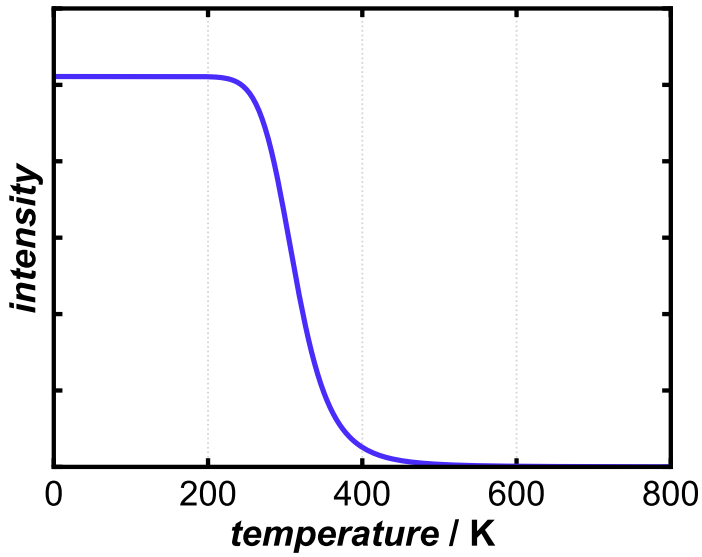

Figure 16: Temperature dependent PL intensity course.

In comparison to the single exponential PL decay of a molecule, in a semiconductor both the electrons and holes affect the dynamics of recombination. This *bimolecular*-analogous behavior cannot be described with a single or with multiple exponential functions. The intensity $I(t)$ is a power-law function of time (Equation 12). In addition, the emission intensity is dependent on the excitation intensity, which makes the system susceptible to fluctuations of the light source intensity.[134,161]

$$I(t) = \frac{I_0}{(\gamma\sqrt{I_0}t + 1)^2} \quad \text{with} \quad \gamma = \frac{\beta}{\sqrt{\beta_r}} \tag{12}$$

The recombination rate is considered as the bimolecular recombination coefficient β, Equation 13, which is the sum of the radiative β_r and nonradiative bimolecular recombination coefficients β_{nr}. In the presence of O_2 the function is extended with the bimolecular recombination coefficient at the corresponding O_2 concentration $\beta_{[O_2]}$. The bimolecular lifetime τ_b is the reciprocal value of β.[134,161]

$$\beta = \beta_r + \beta_{nr} + \beta_{[O_2]}[O_2] \quad \longrightarrow \quad \tau_b = \frac{1}{\beta} \tag{13}$$

The lifetime τ_b is the time of decay to a value of 1/e (Figure 17).

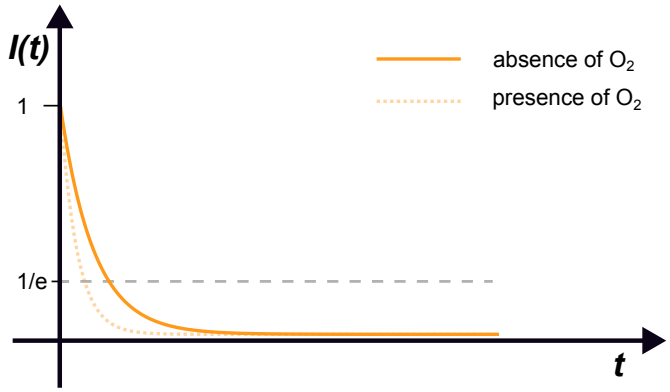

Figure 17: Power-law decay of PL intensity after deactivating the light source in the absence and presence of O_2.

In disordered systems a stretched exponential decay is often observed (Equation 14). This behavior may be related to the dispersion diffusion of photoexcited carriers. The carriers can be trapped and released multiple times, which prolongs the lifetime. The dispersion of movement is determined by the dispersion factor δ.[134]

$$I(t) = I_0 e^{-\left(\frac{t}{\tau_b}\right)^{\delta}} \tag{14}$$

The data can be fitted directly with Equation (14) or can be deconstructed in a single exponential and a generic power-law part, which is revealed on a double-logarithmic scale (Figure 18).[162,163]

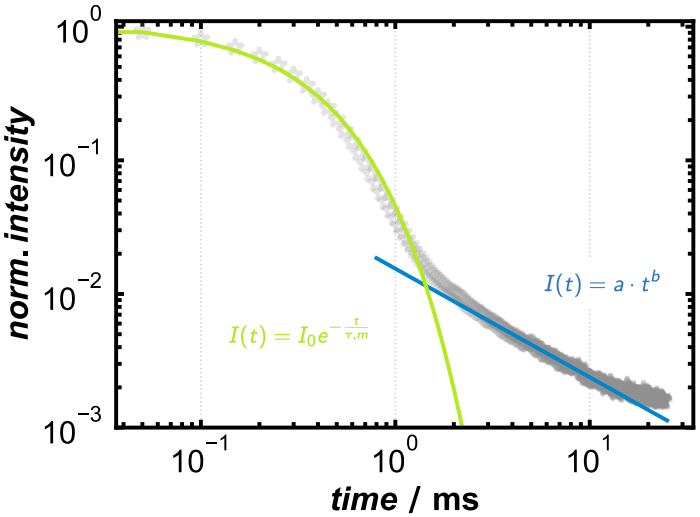

Figure 18: Power-law decay of PL intensity after deactivating the light source as a double-logarithmic scale, revealing a single exponential and power-law component.

The emission properties of SnO_2, ZnO and ZTO differ significantly from each other. With *ca.* 3.3 eV, ZnO has the smallest band gap of the three oxides.[164] Several possible defects generate radiative transitions throughout the entire visible spectral range. O- and Zn-atoms can be missing from their lattice positions, be inverted or placed interstitially. Of the compounds presented, only ZnO exhibits a radiative band-band transition. In Table 2 the radiative transitions, associated defects and lifetimes, are summarized. The defects are described according to the Kröger-Vink notation.[165]

Table 2: ZnO defects associated with various PL transitions.[19,166,167]

defect	region	lifetime
$CB \rightarrow VB$	UV	ps-ns[168,169]
V''_{Zn}	blue	ps-ns[168,169]
V_O, O_i, O_{Zn}	green/yellow	ns-µs[170,171]
V_O	red	ns[171]

SnO_2 exhibits fewer options for radiative transitions (Table 3). Here, only O-defects and Sn-interstitials contribute to emission.[172]

Table 3: SnO_2 defects associated with various PL transitions.

defect	region	lifetime
$CB \rightarrow V_O^{\bullet\bullet}$, Sn_i	blue[173,174]	ns[175,176]
V_O	yellow/orange[177,178]	ns[179]

As the only ternary oxide, the possibilities of defects and their interactions are more pronounced in ZTO (Table 4). Vacancies, interstitials, lattice deformations and alterations in the stoichiometry enable various radiative transitions.[180]

Table 4: Zn_2SnO_4 defects associated with various PL transitions.[180]

defect	region	lifetime
V''_{Zn}	violet[181,182]	
$V_O^{\bullet}$	blue[183]	
Zn_i,Sn_i	green[183,184]	ns[185]
Zn_i, Sn_i, VB_{h+}	green[183,184]	ns[185]
(V_O^x, $V_O^{\bullet}$, $V_O^{\bullet\bullet}$)	yellow/orange[186]	ms[7]
(Sn_i, O_i), V_O	yellow/orange[186–188]	ms[7]
(V''_{Zn}, V''''_{Sn}), (V_O^x, $V_O^{\bullet}$, $V_O^{\bullet\bullet}$), (Zn_i, Sn_i, O_i), residual lattice deformation	orange/red[186]	ms[8]
alterations of Zn/Sn stoichiometry	red[189]	µs[8,190]

PL O_2 sensing has been performed with all the three oxides.[3,8] It is evident from Tables 2-4 that ZTO has significantly longer lifetimes than SnO_2 or ZnO, which is a huge advantage. Lifetimes in the ms range can be further extended by doping with other transition metals *e.g.* Mn, Cr or Al.[190,191]

Compared to metal-organic compounds, metal oxides react distinctly slower with O_2 and excitation wavelengths in the UV range are required. On the other hand, metal oxides exhibit greater resilience to (photo)chemical degradation.[192,193] The synthesis is less complex, it can be easily adapted to large quantities, the samples can be regenerated, the chemicals are earth-abundant and often significantly more environmentally friendly.[6]

2.3 Perovskite Solar Cells

Perovskite solar cells (PSCs) are multi-layer systems. Each layer has a specific function in the cell. Optically transparent substrates, which are coated with transparent conducting oxides (TCOs) like indium tin oxide (ITO) or fluorine-doped tin(IV) oxide (FTO) are the basis for PSCs. The common layer architecture is called *n-i-p structure* and starts with an electron transporting layer (ETL), followed by the light absorbing perovskite layer (Figure 19). On top a hole transporting layer (HTL) is applied. At last, Au electrodes are deposited on the HTL by thermal evaporation.[14,194–196]

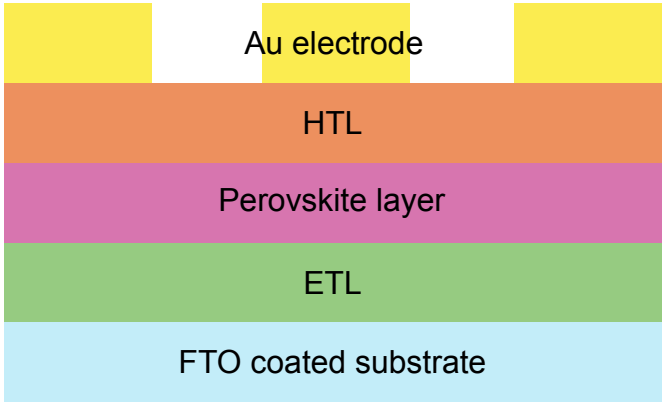

Figure 19: Schematic drawing of an n-i-p perovskite solar cell.

When illuminated with photons of energy larger than the band gap of the semiconductor, an electron-hole pair is generated in the perovskite layer. The electrons and holes are collected by the ETL and HTL, respectively. The substrate acts as an anode and the Au layer as a cathode.

The ETL transports the photogenerated electrons away from the perovskite layer and suppresses the migration of holes from the perovskite layer to the FTO. Therefore, a band structure is necessary that effectively separates electrons and holes to prevent electron-hole

recombination. In addition, the lowest unoccupied levels of the electron transport material needs to be of lower energy than the conduction band energy of the perovskite. It is anticipated that the material will exhibit both high transmittance in the UV/VIS range and thermal stability. Hence this layer usually consists of a metal oxide, *e.g.* TiO_2, SiO_2, SnO_2 or ZnO.[18,197]

The light absorbing perovskite layer has the general formula ABX_3 and can either be inorganic or organic-inorganic based, or a combination of the two. The inorganic perovskite consists of one alkali cation (Li^+, Na^+, K^+, Rb^+ or Cs^+), three halide anions (Cl^-, Br^- or I^-) and one divalent cation like Pb^{2+}, Sn^{2+} or Ge^{2+}. The organic-inorganic perovskite contains instead of the alkali cation a monovalent organic cation like methylammonium ($CH_3NH_3^+$, MA), ethylammonium ($CH_3CH_2NH_3^+$, EA) or formamidinium ($NH_2CHNH_2^+$, FA). The monovalent cations are located on the corners of the unit cell and surround the divalent cation, which is in the center of the unit cell. The anions surround the divalent cation octahedraly and are positioned on the faces of the cubic unit cell (Figure 20).

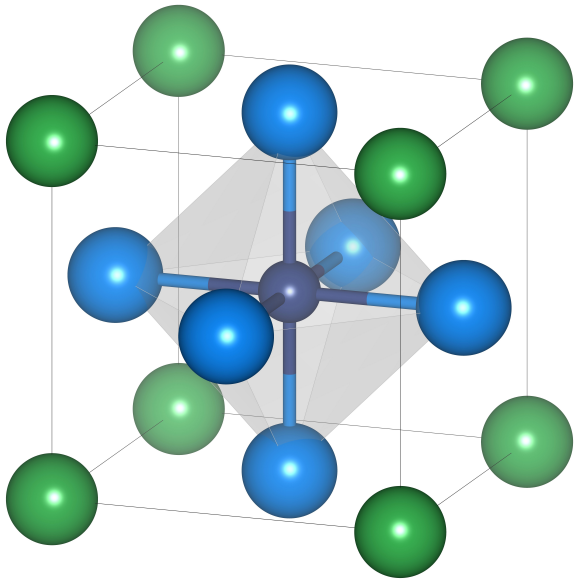

Figure 20: Perovskite crystal structure of $CsPbCl_3$. Caesium atoms are green, chlorine atoms are light blue and the lead atom is dark blue.[198]

The HTL transports the photo-generated holes to the Au cathode and inhibits electron migration. The highest occupied electronic level of the hole transport material is required to be of higher energy than of the used perovskite. Inorganic materials, like NiO_x, Cu_2O, CuO or CuI, or organic materials, *e.g.* Poly(triaryl amine) (PTAA, Figure 21a) or 2,2',7,7'-Tetrakis(N,N-di-p-methoxyphenylamino)-9,9'-spirobifluorene (Spiro-MeOTAD, Figure 21b), are suitable candidates.

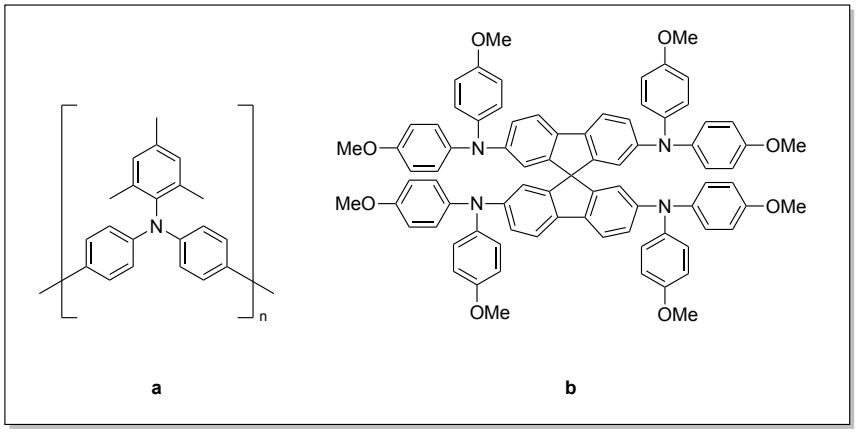

Figure 21: **a** PTAA and **b** Spiro-MeOTAD.

The illumination of the solar cell through a transparent substrate generates current. To characterize the solar cell it is illuminated with a solar simulator and the current I is measured in dependence of the applied voltage V. By relating the current to the size of the illuminated area the current density J is obtained.[199]

From the resulting current-voltage curve (*I-V curve*), the efficiency can be calculated (Figure 22 blue curve). The product of current and voltage is the power P (Figure 22 green curve). The ideal I-V relationship is represented as the dashed red curve in Figure 22.[199]

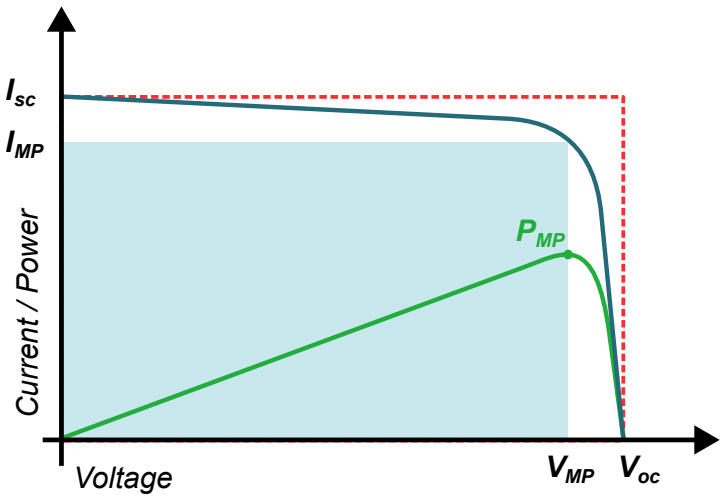

Figure 22: Current (blue) and power (green) of a solar cell in dependence of voltage and ideal current course (dashed red). The power conversion efficiency is the light blue area.[199]

The open-circuit voltage V_{OC} is the voltage required to halt the photogenerated current flow. The maximum photogenerated current, that can be produced from the solar cell, is the short-circuit current I_{SC}. The product of V_{OC} and I_{SC} is the maximum ideal power of the solar cell P_{ideal} (Equation 15).[199]

$$P_{ideal} = V_{OC} \cdot I_{SC} \tag{15}$$

As Figure 22 demonstrates, this power is beyond the measured data. The maximum power point P_{MP} of the solar cell is calculated from the I-V maximum power current I_{MP} and voltage V_{MP}, indicated as the light-blue highlighted area below. The ratio of P_{MP} and P_{ideal} is called *fill factor* (FF) (Equation 16).[199]

$$FF = \frac{P_{MP}}{P_{ideal}} = \frac{V_{MP} \cdot I_{MP}}{V_{OC} \cdot I_{SC}} \tag{16}$$

The power conversion efficiency (PCE) is the ratio of the total output P_{out} and input P_{in} power (Equation 17).[199]

$$PCE = \frac{P_{out}}{P_{in}} = \frac{P_{MP}}{P_{in}} = \frac{V_{MP} \cdot I_{MP}}{P_{in}} \tag{17}$$

3 Zinc Tin Oxide for Photoluminescence O_2 Sensing

The investigation of suitable materials for PL gas sensors is limited by various requirements and technical applicability. For a simple measurement setup without expensive optical components, the excitation and emission wavelengths should be spectrally separated, yet be located in the visible spectral range. The material should be an oxide, as other chalcogenides, *e.g.* sulfur-based, have problems with photobleaching and transform into the corresponding oxides. In addition, the photoluminescence (PL) intensity should be high and the lifetime in the far µs to ms range. This enables excitation with an LED instead of an expensive laser. The specific research of luminescent metal oxides with long lifetimes resulted in the synthesis, characterization and examination of zinc tin oxide's (Zn_2SnO_4, ZTO) gas sensitivity. Though resistive gas sensing has been reported in the literature frequently, PL gas sensing with ZTO has barely been investigated.

In this work, ZTO was prepared through a sol-gel process, followed by thermal conversion. The obtained powders were characterized using a variety of analytical methods, including X-ray powder diffraction (PXRD), UV/VIS-, PL-, and energy dispersive X-ray (EDX) spectroscopy. A thorough examination through scanning electron microscopy (SEM) revealed the absence of any distinct morphology. The prepared samples exhibited an intense orange to red PL emission with a lifetime in the ms range. This emission was effectively quenched in the presence of O_2, thereby giving rise to further inquiries. Fundamental questions concerning the sensing mechanism were a recurring theme. New concepts for PL gas sensing with metal oxides have been developed, building upon the foundations laid by the models for PL gas sensing with (metal-)organic compounds and resistive gas sensing with semiconductors. The applicability of the Stern-Volmer model for bulk materials and the influence of the operating temperature were issues that needed to be resolved.

3.1 O_2 Sensing by Photoluminescence and Electrical Conductance

In order to achieve a more profound comprehension of the sensing mechanism, an investigation was carried out into the Stern-Volmer model in relation to metal oxides. According to the Stern-Volmer model, a linear relationship is established between emission intensity or lifetime and O_2 concentration, resulting in Stern-Volmer plots.

A variation in the operating temperature is indicative of trends in the Stern-Volmer plots, which offer insight into the sensing mechanism. The temperature dependence of the data is crucial in determining the presence of dynamic or static quenching. In the context of static quenching, the formation of a nonradiating complex between the luminophore and quencher is observed. This complex undergoes a decline in stability with an increase in temperature. During dynamic quenching, the luminophore collides with the quencher, a process that becomes more probable with increasing temperature. To date, Stern-Volmer investigations of

solids have been reported exclusively in the context of quantum dots; however, there has been no such reporting with regard to bulk materials so far. This particular topic was the focus of the following study.

The PL and conductance of ZTO were measured simultaneously, while the O_2 concentration and operation temperature were varied. The Stern-Volmer plots of the emission intensity demonstrated that dynamic quenching was observed to occur in accordance with the increase in Stern-Volmer constant with the operating temperature. This assertion was further evidenced by the findings of lifetime measurements in the presence and absence of O_2, which demonstrated the quenching of lifetime. Furthermore, a deviation from the linearity of the classic model was observed. The Stern-Volmer plots exhibited a downward curvature, indicative of incomplete accessibility of the quencher to all luminescent centers within the solid. In this context, the luminescent centers can be conceptualized as photoexcited electrons. As the operating temperature increased, there was a substantial increase in the number of photoexcited electrons that interacted with O_2.

The question of whether charge carriers were fully accessible in the gas was predicated on the proportionality between PL intensity and electrical conductance. The qualitative comparison of PL and conductance revealed a non-linear proportionality and similar data shape regarding Stern-Volmer plots. Though the exact physical background for the conductance data require further investigations, they also indicated that just a fraction of charge carriers was accessible to O_2.

L. Kothe, J. Klippstein, M. Kloß, M. Wengenroth, M. Poeplau, S. Ester, M. Tiemann, *Oxygen-dependent Photoluminescence and Electrical Conductance of Zinc Tin Oxide (ZTO): A Modified Stern-Volmer Description*, ChemPhysChem **2025**, 26, e202400984

- DOI: 10.1002/cphc.202400984

Participation in this Publication

L.K., M.T. and M.P. conceived the project. L.K. was in charge of the experimental work, data analysis and writing of the manuscript with contributions of all authors. M.W. constructed the temperature regulation. S.E. contributed to the critical scientific discussions about the measurements and the Stern-Volmer model. J.K. and M.K. performed the PXRD measurements.

Check for updates

ChemPhysChem

Research Article
doi.org/10.1002/cphc.202400984

Chemistry Europe
European Chemical Societies Publishing

www.chemphyschem.org

Oxygen-Dependent Photoluminescence and Electrical Conductance of Zinc Tin Oxide (ZTO): A Modified Stern-Volmer Description

Linda Kothe,[a, b] Josefin Klippstein,[a] Marvin Kloß,[a] Marc Wengenroth,[b] Michael Poeplau,[b] Stephan Ester,[b] and Michael Tiemann*[a]

Zinc tin oxide (ZTO) is investigated as a photoluminescent sensor for oxygen (O_2); chemisorbed oxygen quenches the luminescence intensity. At the same time, ZTO is also studied as a resistive sensor; being an *n*-type semiconductor, its electrical conductance decreases by adsorption of oxygen. Both phenomena can be exploited for quantitative O_2 sensing. The respective sensor responses can be described by the same modified Stern-Volmer model that distinguishes between accessible and non-accessible luminescence centers or charge carriers, respectively. The impact of the temperature is studied in the range from room temperature up to 150 °C.

Introduction

Photoluminescence-based sensors have great potential for contactless gas detection.[1] Most frequently, metal-organic compounds are used. In recent years, however, purely inorganic materials were also investigated, including porous silicon,[2] semiconducting metal oxides,[3,4] and metal chalcogenides, including quantum dots.[5,6] Oxygen (O_2) detection is a major application of photoluminescence sensing. As oxygen is present in biological systems, safety and air quality, oxygen sensors are required to monitor vital or healing functions,[7,8] detonation limits[9] or air quality.[10] Commercially available resistive O_2 sensors based on metal oxides, *e.g.* zirconium dioxide (ZrO_2), can cover a concentration range from 0.1 vol% to 100 vol% O_2.[11]

To describe the gas-dependent change of luminescence intensity and decay time of semiconductors, the ionosorption model, which is the basis of standard models in resistive semiconductor gas sensing, can be used. In case of *n*-type semiconductors, oxygen (O_2) binds to the surface, thereby immobilizing electrons from the conduction band, which reduces the overall conductance.[12] This model can be extended to luminescence-based sensors, where O_2-induced luminescence quenching is used for detection. Photoexcited electrons are trapped (immobilized) by adsorption of O_2 at the surface and therefore cannot recombine radiatively or non-radiatively with valence band holes or acceptor/donor states. With increasing O_2 concentration, the thus-induced electron depletion layer becomes thicker, and the surface barrier becomes higher. Hence, photoluminescence intensity and electrical conductance may be regarded as proportional.

At molecular level, O_2-induced quenching of photoluminescence is described by the Stern-Volmer model.[13] It has also been explored for quantum dots,[6,14] but not to bulk solid-state oxygen sensors, to the best of our knowledge. The Stern-Volmer model distinguishes between static and dynamic quenching. In the static case, the luminescent center and a quencher molecule form a non-radiative complex. This has an impact on the luminescence intensity but not on the decay time; the complex dissociates with increasing temperature. In case of dynamic quenching, the luminescent center and a quencher molecule collide, and the energy of the excited luminophore is transferred to the quencher. As the excited electron recombines non-radiatively, the recombination rate is affected by the quencher molecule, although no chemical bond forms. With increasing temperature, more collisions occur, and the impact becomes more pronounced. The standard Stern-Volmer Equation (1) applies to both mechanisms, where I_0 and I_Q are the fluorescence intensities in the absence and presence of the quencher, respectively, [*Q*] is the quencher concentration, and K_{SV} is the Stern-Volmer constant. The Stern-Volmer equation is valid if all luminescent centers are equally accessible to the quencher molecules and either dynamic or static quenching occurs.

$$\frac{I_0}{I_Q} = 1 + K_{SV} \cdot [Q] \tag{1}$$

Bulk materials may not be as accessible for the quencher as molecules, due to the coexistence of surface and bulk excitons. Therefore, we suggest the modified Stern-Volmer Equation (2),

[a] L. Kothe, J. Klippstein, M. Kloß, M. Tiemann
Faculty of Science – Department of Chemistry, Paderborn University, Warburger Str. 100, D-33098 Paderborn, Germany
E-mail: michael.tiemann@uni-paderborn.de

[b] L. Kothe, M. Wengenroth, M. Poeplau, S. Ester
Woehler Technik GmbH, Woehler-Platz 1, D-33181 Bad Wuennenberg, Germany

Supporting information for this article is available on the WWW under https://doi.org/10.1002/cphc.202400984

ChemPhysChem
Research Article
doi.org/10.1002/cphc.202400984
Chemistry Europe
European Chemical Societies Publishing

which was first introduced by Lehrer[15] for proteins in solution, as a suitable alternative that deepens the understanding of the sensing mechanism.

$$\frac{I_0}{I_0 - I_Q} = \frac{1}{f_a K_a [Q]} + \frac{1}{f_a} \quad (2)$$

The modified Stern-Volmer equation contains a fraction f_a, which provides quantitative information about the accessibility of the luminescent centers for the quencher.

Suitable metal oxides for photoluminescence-based O_2 sensing are, *e.g.*, SnO_2, TiO_2, ZnO or lanthanoid-doped ZrO_2.[3,4] Here we introduce zinc tin oxide (ZTO, Zn_2SnO_4) as another candidate. ZTO is an *n*-type semiconductor which is chemically more stable than ZnO and transparent in the visible range (wide band gap of *ca.* 3.6 eV). It is interesting for a variety of potential applications, including as gas sensors, coatings, transistors, photocatalysts and in optoelectronics.[16,17,18] Therefore, ZTO is a suitable material for gas-sensing studies based on both photoluminescence and electrical conductance.

In this work we show the O_2-depencence of the ZTO defective photoluminescence and investigate its quencher accessibility with the modified Stern-Volmer equation between 40 °C and 150 °C.

Results and Discussion

ZTO is used as an exemplary material to gain deeper understanding of photoluminescence and conduction O_2 sensing. The synthesized ZTO is characterized in the Supporting Information (Figures S1–S5). Additional information about measurement setup and parameters are also available in the Supporting Information (Figures S6–S8).

Sensing Mechanism

For gas sensing, either by photoluminescence or by the resistive method, the surface-near region of the semiconducting material is relevant (Debye length, photon penetration depth).[19,20] Figure 1 shows a schematic of the band energies and defect state levels.

When the semiconductor is excited by electromagnetic radiation of higher energy than the band gap, electrons are elevated from the valence band to the conduction band (i). Since semiconductors show strong absorbance in the band gap energy domain, it can be assumed that the exciting radiation is completely absorbed and that all luminescent centers are excited. In case of ZTO, the band gap is between 3.6 eV and 3.7 eV. When ZTO is excited with 325 nm, the estimated photon penetration length, depending on the absorption coefficient (*e.g.*, 0.625), is *ca.* 520 nm.[21] Excited electrons from the conduction band reach a defect state by non-radiative transition (ii). It was reported that photoluminescence in the blue-green range is probably attributable to oxygen defects, whereas emission at longer wavelengths may be related to interaction between oxygen vacancies and interfacial tin or zinc vacancies.[22,23] Hence, the photoluminescence in this study (orange, *ca.* 2.05 eV) is presumably based on a combination of interacting defect states. The excitation/emission spectrum and emission spectrum at $\lambda_{ex} = 325$ nm are shown in the Supporting Information section (Figure S4). From the defect state, electrons can recombine radiatively with valence band holes (iii).

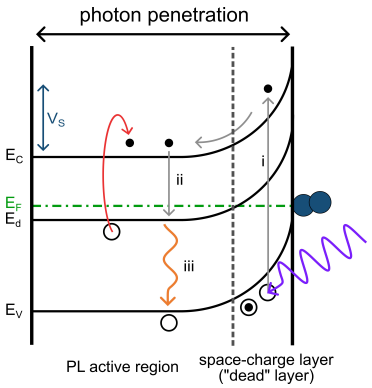

Figure 1. Schematic depiction of the energy levels of zinc-tin oxide (ZTO). Excitation with UV radiation (violet), followed by non-radiative transitions (gray) to the defect state, where electrons recombine radiatively (orange) with the valence band. Thermal activation (red) of electrons from the defect state to the conduction band.

The chemisorption of O_2 results in an upward band-bending, as ZTO is an *n*-type semiconductor, and a decrease in Fermi energy. Photoexcited electrons are trapped by O_2 at the surface and do not participate in recombination. Consequently, fewer photoelectrons are present, and the luminescence intensity decreases; an electron depletion layer is generated. It should be noted that different oxygen species must be expected to chemisorb to the ZTO surface, depending on the temperature. In case of SnO_2 and ZnO the main adsorbing species between room temperature and *ca.* 80 °C is the neutral O_2 molecule. In addition, the singly negatively charged O_2^- molecular ion (superoxo ion) is present. This species implies a formal reduction of one O atom to the oxidation state -I and proves the chemical alteration of the metal oxide. At *ca.* 150 °C, the superoxo ion becomes more dominant than the uncharged molecule. The ratio of physisorbed (molecular) and chemisorbed (superoxo) O_2 is temperature-dependent, but only the chemisorbed species affects the photoluminescence and conductance. Above 200 °C, the dissociated O^- (peroxo) and O^{2-} (lattice-like oxide) species are present.[24–27] It is fair to assume a similar situation for ZTO. The supplemented surface charge due to chemisorption of O_2^- and/or O^- is compensated by the space-charge layer, as holes accumulate near the surface. With increasing temperature, the adsorption/desorption process of O_2 is also accelerated.

ChemPhysChem
Research Article
doi.org/10.1002/cphc.202400984
Chemistry Europe
European Chemical Societies Publishing

The spatial separation of electrons and holes due to continuous excitation creates a space-charge layer in the surface-near regions of the metal oxide, where electrons move into the bulk and holes move to the surface. The presence of holes at the surface results in surface photovoltage and reduces band-bending.[28] The recombination rates are reduced by the near-surface electric field. Due to the low PL intensity in this region, it is called "dead layer".[29,30] Therefore, the dead layer is a photophysical phenomenon. As band-bending also affects the defect state, radiative recombination can only occur if the Fermi energy is larger than the defect state energy. The thickness of the space-charge layer, which is roughly a synonym for the depletion layer, is defined as the depth where the Fermi and defect state energy are equal. The height of the depletion layer is called surface potential, V_s, or Schottky barrier.

Beyond the space-charge layer lies the photoluminescence-active region, which is also affected by the surface potential and the thickness of the depletion layer. O_2 saturation occurs if the Fermi energy is equal to the LUMO (lowest unoccupied molecular orbital) of O_2 and no further band bending occurs. The LUMO of O_2 is energetically lower than the Fermi energy of ZTO in the absence of O_2. The decrease in Fermi energy due to O_2 chemisorption is limited by the absolute position of the O_2 LUMO. The energy difference between conduction band and Fermi energy stays intact. The absolute LUMO position of O_2 does not change with O_2 concentration, but the band bending and the absolute position of the Fermi energy, which are both limited by the absolute position of the O_2 LUMO.

In addition to the intensity the emission lifetime is also quenched in the presence of O_2 (Figure 2). The emission spectrum (see Figure S4b) reveals that two emission bands overlap, resulting in an emission maximum at *ca.* 650 nm, when excited with 325 nm. The overlapping emission bands have their intensity maxima at 613 nm and 741 nm, respectively. Here we focus on the emission at 613 nm, while the emission at 741 nm will be part of future studies. To determine the lifetime, we evaluate the time that the system needs to decay to 1/*e* of the intensity. In a pure N_2 atmosphere the lifetime is 4656 µs ± 17 µs, whereas with a content of 20 vol% O_2, it is shorter by 442 µs (4214 µs ± 21 µs). The lifetimes under ambient conditions and at 741 nm are displayed in the Supporting Information, see Figure S5. The quenching of the lifetime supports the assumption, that the chemisorption of O_2 introduces additional non-radiative routes, which trap photoelectrons.

Modified Stern-Volmer Equation for Photoluminescence

The difference in photoluminescence intensity in pure N_2 and in a 20/80 vol% O_2/N_2 atmosphere is displayed in Figure 3. The emission intensity is higher in the absence of O_2, which can be explained by the above-described O_2 quenching.

When a temperature change is applied, the intensity changes instantaneously. (Spikes in the intensity are artefacts caused by overdriving from the heating element.) With increasing temperature, more electrons from the defect state are thermally activated to the conduction band, which, in resistive gas sensing, causes an increase in electrical conductance. Concerning photoluminescence, however, non-radiative recombination instances become more and more dominant with increasing temperature, resulting in temperature-induced luminescence quenching. This is probably a Schön-Klasens mechanism, since the thermal activation can also be measured via conductance and additional possibilities for non-radiative recombinations are introduced by O_2 chemisorption.[31,32] The temperature quenching is likely affected by the chemisorption of O_2 and therefore the respective species could have a different influence on temperature quenching. As previously described, the neutral molecular and the superoxo species are most likely present at the operating temperatures in this study. Therefore, the superoxo species might influence the temperature quenching.

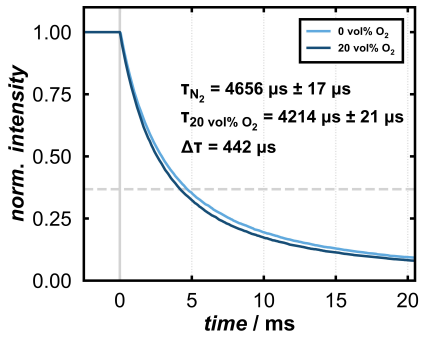

Figure 2. Life time of the orange emission (λ_{em} = 613 nm, with λ_{ex} = 325 nm) at room temperature in N_2 (light blue) and 20 vol% O_2 in N_2 (dark blue).

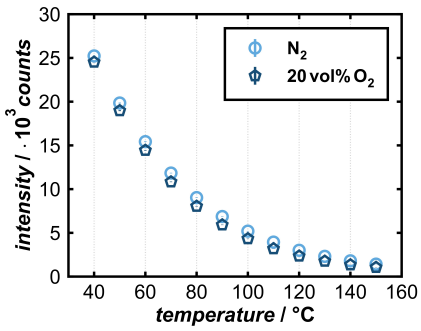

Figure 3. Temperature dependence of the intensity at 606 nm in N_2 (light blue) and 20 vol% O_2 in N_2 (dark blue).

ChemPhysChem
Research Article
doi.org/10.1002/cphc.202400984
Chemistry Europe
European Chemical Societies Publishing

O_2-induced quenching was investigated by measuring the luminescence at variable O_2 concentration (0% … 20 vol% in N_2), each at variable temperature. Data are plotted in Figure 4a as (I_0/I_{O2})-1 *vs.* O_2 concentration, corresponding to the Stern-Volmer Equation (1). (Measured intensities vs. time and vs. temperature are shown in the Supporting Information, Figure S8). Two findings are apparent from Figure 4a: (i) With increasing temperature, the slope of the graphs becomes steeper, which is a typical behavior of dynamic photoluminescence quenching. Oxygen chemically binds to the semiconductor's surface, analogous to the collision of the quencher molecule with the luminescent center in the description of molecular luminescence quenching. (ii) The relationship between (I_0/I_{O2})-1 and the O_2 concentration is clearly not linear, *i.e.* Stern-Volmer Equation (1) does not describe the behavior. The decrease in the slope of the graphs with increasing O_2 concentrations indicates that not all luminescence centers interact with the quencher.[13] This behavior is frequently observed for proteins or metal-organic compounds with several luminescent centers.[15,33] In addition, an inhomogeneous particle size distribution (see Figure S3a) may result in a variation of quencher accessibility.

For a more accurate description of the relationship between luminescence quenching and O_2 concentration, we propose the extended Stern-Volmer model in Equation (2). This equation is based on the assumption that there are two kinds of luminescent centers, only one of which interacts with the quencher molecules. The overall intensity is then the sum of both intensities. In Equation (2), $I0_{,a}$ is the luminescence intensity (in the absence of the quencher) of the accessible centers that can interact with the quencher, with a Stern-Volmer constant K_a, and $I_{0,b}$ is the luminescence intensity of the inaccessible centers that are unaffected by the quencher.

$$I_Q = \frac{I_{0,a}}{1 + K_a[Q]} + I_{0,b} \tag{2}$$

The fraction of accessible centers (irrespective of the quencher concentration) is defined as f_a by Equation (3).

$$f_a = \frac{I_{0,a}}{I_{0,a} + I_{0,b}} \tag{3}$$

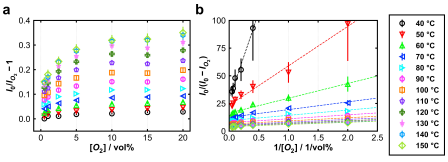

Figure 4. (a) Original Stern-Volmer plot of photoluminescence between 40 °C and 150 °C. **(b)** Modified Stern-Volmer plot of photoluminescence between 40 °C and 150 °C and the respective linear fits as dashed lines.

Combining Equations (2) and (3) yields the modified Stern-Volmer Equation (4) (see Supporting Information, Equations S2–S13).

$$\frac{I_0}{I_0 - I_Q} = \frac{1}{f_a K_a[Q]} + \frac{1}{f_a} \tag{4}$$

If f_a equals 1, Equation (4) becomes the standard Stern-Volmer Equation (1), as all centers are accessible.

Figure 4b shows the plots of $I_0/(I_0\text{-}I_Q)$ *vs.* $[Q]^{-1}$, according to Equation (4), at variable temperature. All graphs show a near-linear behavior for all temperatures; with increasing temperature, the slopes and intercepts decrease. Figure 5 shows the data in single plots (for clarity), including the results of linear regression (slope *m* and ordinate intercept *b*).

Between 40 °C and 60 °C the linearity (R^2) is better than at higher temperatures. Since the modified Stern-Volmer equation assumes two luminescent centers with only one of them interacting with the quencher, the deviation from linearity might indicate a third group of luminescent centers that also interact with the quencher but with a different Stern-Volmer constant. Structural changes due to the increased measuring temperature seem negligible, as significant structural changes, such as opening of defect sites or formation of a porous phase, would be irreversible.

Modified Stern-Volmer Equation for Conductance

As discussed above, a close relationship exists between O_2-induced luminescence quenching (usable for optical O_2 sensing) and O_2-induced decrease in electrical conductance (usable for resistive sensing). Indeed, photoluminescence intensity and electrical conductance *G* turn out to be proportional to each other, as shown in Figure 6, which stands to reason considering that both are similarly affected by O_2 adsorption.

The normalized measurements and concentration-dependent values are displayed in the Supporting Information (Figures S10–S12). It needs to be stressed that the conductance was measured simultaneously with luminescence, *i.e.* under irradiation; without this optical activation, the conductance is altogether lower, as will be discussed below (see Supporting Information, Figure S13). The response is stronger for the conductance under all conditions, while photoluminescence shows faster response and a more stable signal baseline. In particular, the recovery of the conductance is vastly incomplete within the one-hour periods between consecutive O_2 supplies. The photoluminescence response to O_2 increases with temperature, from 2% at 40 °C to 25% at 160 °C (for 20% O_2, as compared to pure N_2 atmosphere). The lowest signal-to-noise ratio is observed at 120 °C.

At 160 °C, the O_2 dependence for both conductance and photoluminescence is most pronounced. When plotted against each other, the proportionality of these two measurands is revealed (Figure 7).

The plot indicates two different proportionalities. Between 0 vol% and 2.5 vol% O_2, a non-linear relation exists, whereas

ChemPhysChem
Research Article
doi.org/10.1002/cphc.202400984
Chemistry Europe
European Chemical Societies Publishing

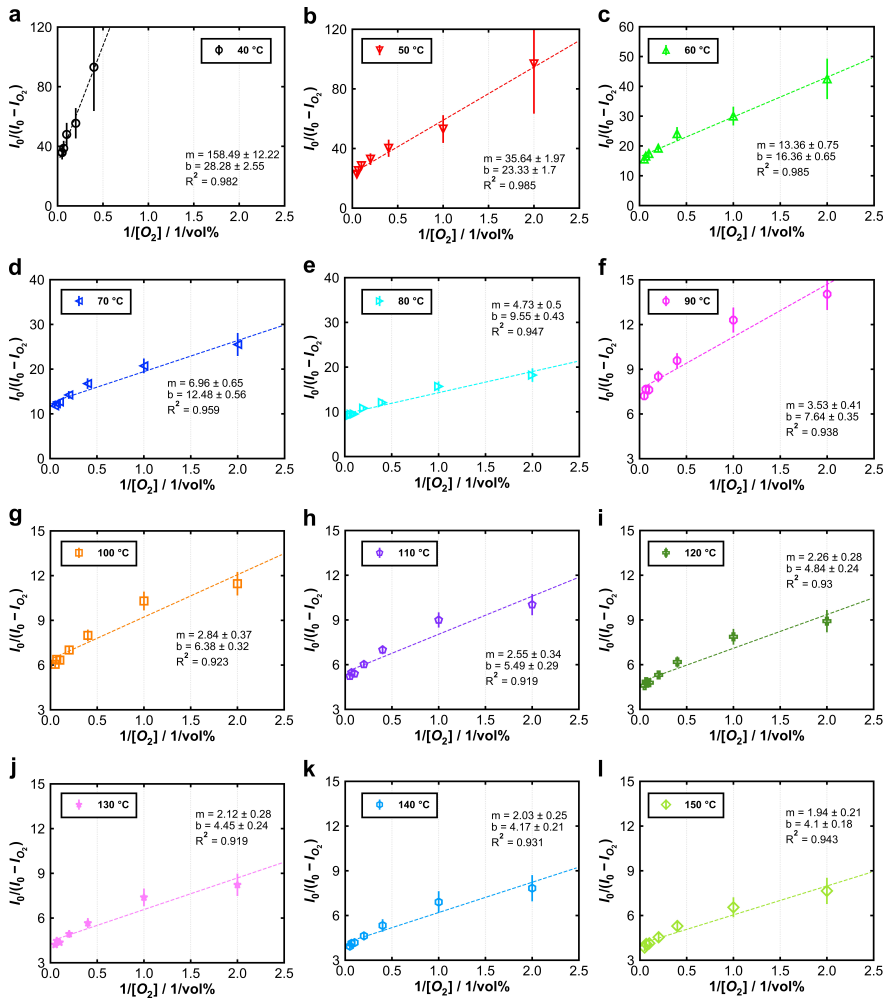

Figure 5. Modified Stern-Volmer plot of photoluminescence and linear regression (dashed lines) at **(a)** 40 °C, **(b)** 50 °C, **(c)** 60 °C, **(d)** 70 °C, **(e)** 80 °C, **(f)** 90 °C, **(g)** 100 °C, **(h)** 110 °C, **(i)** 120 °C, **(j)** 130 °C, **(k)** 140 °C, and **(l)** 150 °C.

between 2.5 vol% and 20 vol% O_2, a linear proportionality manifests. This might indicate that at lower O_2 concentrations mechanistic differences are more pronounced and need to be evaluated, but if saturation occurs, both measurands act roughly linear proportional with a slope of 0.143 nS/counts.

Applying the Stern-Volmer Equation (1) to the electrical conductance G reveals the same behavior as previously observed for the luminescence intensity (Figure 8a). With increasing temperature, the slope of the graphs becomes steeper, and a downward curvature occurs. Hence, only a fraction of charge carriers seems to be accessible to O_2. Again, when the data are plotted according to the modified Stern-Volmer Equation (5), a near-linear behavior is observed (Figure 8b), with the same tendencies as for the luminescence

ChemPhysChem
Research Article
doi.org/10.1002/cphc.202400984
Chemistry Europe
European Chemical Societies Publishing

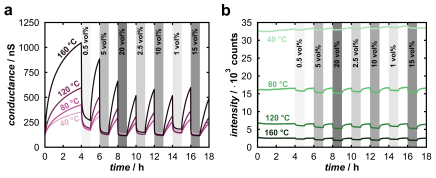

Figure 6. (**a**) Conductance and (**b**) photoluminescence measured simultaneously (40 °C, 80 °C, 120 °C and 160 °C) at different O_2 concentrations.

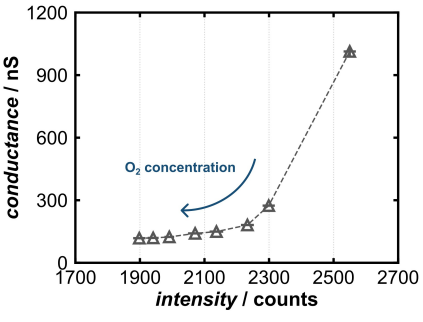

Figure 7. Conductance vs. photoluminescence at 160 °C. (The grey dashed line serves as a guide for the eye only).

intensity. From the slopes and intercepts of the linear regressions to the data in Figure 4b and 7b, the Stern-Volmer constant K_σ and the accessible fraction f_σ can be calculated from for each temperature (40 °C–160 °C). The results are shown in Figure 9 for both photoluminescence and conductance.

For luminescence, the Stern-Volmer constant increases from *ca.* 0.18 vol%$^{-1}$ (40 °C) to *ca.* 2.16 vol%$^{-1}$ (90 °C) and stays approximately constant at higher temperature. The accessible fraction also increases with temperature. At 40 °C, less than 5 % ($f_\sigma < 0.05$) of all luminescent centers are accessible to O_2; for 150 °C, the value reaches *ca.* 25 % ($f_\sigma = 0.25$). These results are consistent with the above-mentioned 'dead layer' model, especially for smaller temperatures, where the lowest degree of band-bending occurs. Only few photo-excited electrons are accessible to interact with O_2 due to their spatial separation from the solid-gas interface. With increasing temperature, more and more electrons are thermally activated from donor states below the conduction band (Figure 1), which is consistent with the observation of higher electrical conductance (see below). With a higher amount of charge carriers in the conduction band, more electrons can be trapped by O_2. Thus, the surface potential increases, and the depletion layer becomes thicker.

Even though the Stern-Volmer model can technically also be applied to the conductance data, the respective values of f_σ and K_σ are not physically analogous, though still proportional. The derivation of a corresponding model regarding the conductivity would be worthwhile and interesting. However, this would require additional studies based on adsorption models to gain a deeper understanding of the physical background of these parameters,[34,35] which is beyond the scope of this study. Therefore, we compare the two distinct sets of f_σ and

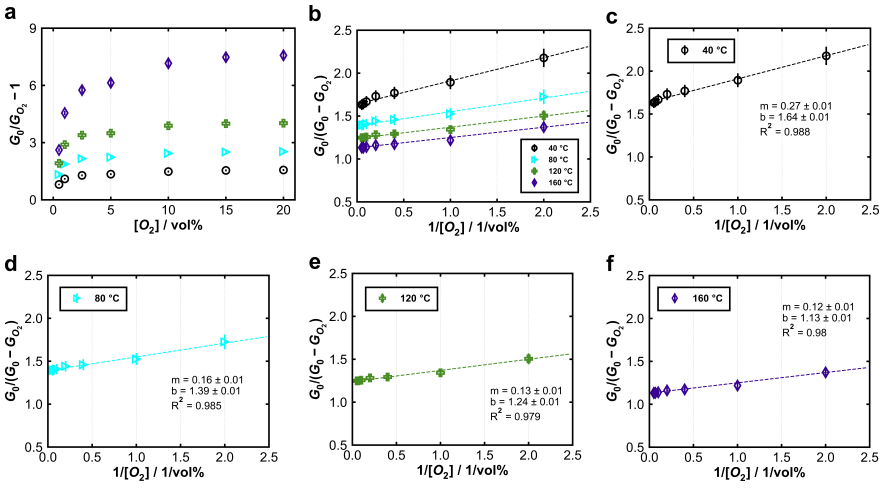

Figure 8. (**a**) Original Stern-Volmer plot of conductance between 40 °C and 160 °C. Modified Stern-Volmer plots of conductance and linear regression (dashed lines) between 40 °C and 160 °C (**b**) as well as single plots at (**c**) 40 °C, (**d**) 80 °C, (**e**) 120 °C, (**f**) 160 °C.

ChemPhysChem
Research Article
doi.org/10.1002/cphc.202400984
Chemistry Europe
European Chemical Societies Publishing

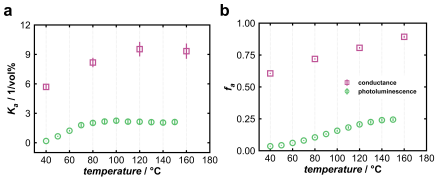

Figure 9. (**a**) Temperature-dependent Stern-Volmer constant K_a and (**b**) accessible fraction f_a for photoluminescence (green) and conductance (pink).

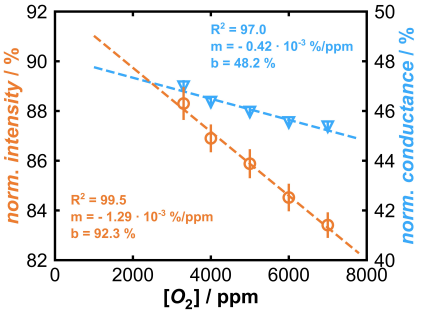

Figure 10. Normalized photoluminescence (orange) and conductance (light blue) measured simultaneously at 120 °C at different O_2 concentrations (3300 ppm to 7000 ppm) both fitted by linear regression.

K_a values at a qualitative level only. For electrical conductance, the Stern-Volmer constant increases up to 120 °C, followed by a plateau. The f_a values also become higher with temperature, which indicates that the charge carries might become more accessible to O_2. For luminescence, both K_a and f_a reach a plateau at lower temperature than for conductance. This may indicate that recombination processes and, thus, the interaction with O_2 are more affected by small temperature changes than in case of conductance.

We hypothesize that a major difference in accessibility between photoluminescence and conductance may be related to the binding energy of the excitons. The charge carriers, measured by conductance are mobile and mostly inhibited by the surface potential (Schottky barrier). However, in order for an exciton to release an electron to form a surface bond, the binding energy of the exciton must also be overcome. With increasing temperature, the exciton bonds become weaker, which may facilitate a higher degree of accessibility to O_2.[36] The separated excitons may act as additional luminescent centers that interact with O_2, but with different kinetics as compared to intact excitons. It should also be stressed that, in case of photoluminescence, the Stern-Volmer model indicates a dynamic quenching based on an energy transfer between the excited state and the quencher.

A pronounced influence of ultraviolet (UV) light illumination on both the electrical conductance and the response to oxygen (O_2) is observed. This is apparent from comparing the conductance measurements taken in the absence of illumination, as shown in the supporting information (Figure S13). This effect of photo-activation is well-established in the field of resistive gas sensing.[37,38]

To estimate the lower O_2 detection limit, photoluminescence and conductance were measured simultaneously at 120 °C with O_2 concentrations between 3300 ppm and 7000 ppm (limits of the current gas mixing equipment, see Supporting Information, Figure S14). In previous studies we found that, at 120 °C, the signal-to-noise ratio due to O_2 and temperature quenching is the highest.[39] From the measurements, the normalized values at the different O_2 concentrations were determined and plotted accordingly, Figure 10. For the measured concentration range a linear behavior is revealed.

Though the intercept of conductance is much lower compared to photoluminescence, the slope of the photoluminescence values is significantly higher. For a better comparison of the slopes, it was assumed for both measurands that the lower detection limit is the double value of the worst standard deviation for a reliable detection. For photoluminescence (1.32 %) results from the slope a detection limit of *ca.* 1000 ppm and for conductance (0.53 %) a limit of *ca.* 1250 ppm. This would indicate that photoluminescence might be more surface sensitive than conductance. The photoluminescence of SnO_2 did not change significantly in the presence of O_2, but the lower detection limit for the defect luminescence of TiO_2 were at 25 ppm O_2. For ZrO_2 and ZnO no lower detection limits were determined so far, but O_2 concentrations between 0.4 vol% and 2 vol% were usually detected reliably.[3,4]

Conclusions

Semiconducting zinc tin oxide (ZTO) was used as a sensor for oxygen (O_2) by measuring both photoluminescence quenching (optical sensor) and electrical conductance (resistive sensing). An increase in temperature thermally quenches photoluminescence and enhances conductance by thermal activation. Luminescence intensity and electrical conductance are found to be proportional to each other, consistent with the fact that both phenomena are related to the degree of oxygen adsorption at the surface of ZTO. The responses to O_2 (at elevated temperature) can be described by a modified Stern-Volmer model that accounts for an accessible and for a non-accessible fraction of luminescent centers and charge carriers, respectively. The accessible fraction of luminescent centers increased fivefold in a temperature range of 110 °C, which highlights the advantage of photoluminescence gas sensing at low operating temperature.

ChemPhysChem
Research Article
doi.org/10.1002/cphc.202400984
Chemistry Europe
European Chemical Societies Publishing

Experimental

Sensor Preparation

0.154 mol zinc(II)acetate (98%; VWR) and 0.077 mol anhydrous tin(IV)chloride (99%, VWR) were added to a solution of 150 mL absolute ethanol (≥99.5%, VWR), 150 μL ethylene glycol (≥98%, VWR) and 0.77 mol diethanolamine (synthesis quality, VWR). The synthesis mixture was refluxed for 2 h and then cooled to room temperature. The thus-obtained clear solution (sol) was stored for one week. Part of the clear, colorless sol was heated to 550 °C with a heating rate of 300 °C/h and held for 4 h, followed by grinding. The residual was heated to 1100 °C with a heating rate of 300 °C/h and the temperature was kept for 6 h. Finally the product was ground. The substrates were cleaned alternately with acetone and ethanol, three times each, and dried at 80 °C. An aqueous dispersion of the product with a concentration of 0.04 mg/μL was prepared. At 80 °C 150 μL of the dispersion were drop coated twice on the interdigital structure of the substrate.

Characterization

Scanning electron microscopy was performed with a Zeiss Neon 40. Powder X-ray diffraction patterns were recorded with a Bruker D8 Advance diffractometer (Cu-K_α, 0.02° steps, 3 s illumination time). The excitation-emission spectra (2 nm steps) and lifetime measurements ("phosphorescence life time", $\lambda_{ex} = 325\ nm$, excitation bandwidth = 5 nm, $\lambda_{em} = 613\ nm$ and 741 nm, emission bandwidth = 20 nm, 50 ms chopping period) were recorded with a JASCO 8550 spectrofluorometer.

Acknowledgements

We thank Nadine Buitkamp for help with SEM and EDX. Open Access funding enabled and organized by Projekt DEAL.

Conflict of Interests

The authors declare no conflict of interest.

Data Availability Statement

The data that support the findings of this study are available from the corresponding author upon reasonable request.

Keywords: Zinc tin oxide (ZTO) · Gas sensor · Photoluminescence · Resistive sensor · Stern-Volmer model

[1] X.-D. Wang, O. S. Wolfbeis, *Chem. Soc. Rev.* **2014**, *43*, 3666–3761.
[2] W. Jaimes Salcedo, F. J. Ramirez Fernandez, J. C. Rubim, *Spectrochim. Acta A* **2004**, *60*, 1065–1070.
[3] A. Fioravanti, P. Marani, S. Morandi, L. Giordano, P. Maddalena, M. C. Carotta, S. Lettieri, *Chemosensors* **2021**, *9*, 163.
[4] V. Kiisk, L. Puust, H. Mändar, P. Pitslaid, M. Rähn, I. Bite, D. Jankovia, I. Sildos, R. Jaaniso, *Mater. Chem. Phys.* **2018**, *214*, 135–142.
[5] M. Poeplau, S. Ester, B. Henning, T. Wagner, *Phys. Chem. Chem. Phys.* **2020**, *22*, 19948–19956.
[6] X. Q. Yan, Z. B. Shang, Z. Zhang, Y. Wang, W. J. Jin, *Luminescence* **2009**, *24*, 255–259.
[7] D. B. Papkovsky, R. I. Dmitriev, *Chem. Soc. Rev.* **2013**, *42*, 8700–8732.
[8] M. Ochoa, R. Rahimi, J. Zhou, H. Jiang, C. K. Yoon, D. Maddipatla, B. B. Narakathu, V. Jain, M. M. Oscai, T. J. Morken, R. H. Oliveira, G. L. Campana, O. W. Cummings, M. A. Zieger, R. Sood, M. Z. Atashbar, B. Ziaie, *Microsyst. Nanoeng.* **2020**, *6*, 46.
[9] M. Wilett, *Sensors* **2014**, *14*, 6084–6103.
[10] R. Ramamoorthy, P. K. Dutta, S. A. Akbar, *J. Mater. Sci.* **2003**, *38*, 4271–4282.
[11] PST Process Sensing Technologies, *Probe Zirconia Oxygen Sensor*, 28.11.**2024**, 14:35, https://www.processsensing.com/en-us/products/probe-oxygen-sensor.htm
[12] M. Tiemann, *Chem. Eur. J.* **2007**, *13*, 8376–8388.
[13] J. R. Lakowicz, *Principles of Fluorescence Spectroscopy*, Springer, New York **2006**, 277–289.
[14] J. Zhang, L. Na, Y. Jiang, D. Lou, L. Jin, *Anal. Methods* **2016**, *8*, 7242.
[15] S. Lehrer, *Biochemistry* **1971**, *10*, 3254–3263.
[16] J. Dou, D. Shen, Y. Li, A. Abate, M. Wei, *ACS Appl. Mater. Interfaces* **2019**, *11*, 36553–36559.
[17] J. Seo, H. Yoo, *Membranes (Basel)* **2022**, *12*, 485.
[18] T. Huang, Y. Hou, H. Zheng, L. Zhao, J. Wang, R. Jiang, S. Hu, S. Chu, Y. Zhang, S. Jia, J. Wang, *ACS Nano* **2024**, *18*, 5396–5408.
[19] A. Stevanovic, M. Büttner, Z. Zhang, J. Yates, *J. Am. Chem. Soc.* **2012**, *134*, 324–332.
[20] Z. Zhang, J. T. Yates, *Chem. Rev.* **2012**, *112*, 5520–5551.
[21] J.-B. Shi, P.-F. Wu, H.-S. Lin, Y.-T. Lin, H.-W. Lee, C.-T. Kao, W.-H. Liao, S.-L. Young, *Nanoscale Res. Lett.* **2014**, *9*, 210.
[22] L. Wang, X. Zhang, X. Liao, *Nanotechnology* **2005**, *16*, 2928–2931.
[23] J.-W. Zhao, L.-R. Qin, L.-D. Zhang, *Solid State Commun.* **2007**, *141*, 663–666.
[24] H. Chon, J. Pajares, *J. Catal.* **1969**, *14*, 257–260.
[25] N. Yamazoe, J. Fuchigami, M. Kishikawa, T. Seiyama, *Surf. Sci.* **1979**, *86*, 335–344.
[26] A. Gurlo, *ChemPhysChem* **2006**, *7*, 2041–2052.
[27] A. Staerz, U. Weimar, N. Barsan, *Sens. Actuators B* **2022**, *358*, 131531.
[28] K. Sell, I. Barke, S. Polei, C. Schumann, V. von Oeynhausen, K.-H. Meiwes-Broer, *Phys. Status Solidi B* **2010**, *247*, 1087–1094.
[29] R. E. Hollingsworth, J. R. Sites, *J. Appl. Phys.* **1982**, *53*, 5357–5358.
[30] G. J. Meyer, G. C. Lisensky, A. B. Ellis, *J. Am. Chem. Soc.* **1988**, *110*, 4914–4918.
[31] M. Reshchikov, *J. Appl. Phys.* **2014**, *115*, 012010.
[32] M. Reshchikov, *Phys. Status Solidi A* **2021**, *218*, 2000101.
[33] F. Friedl, N. Krah, B. Jähne, *Sens. Actuators B* **2015**, *206*, 336–342.
[34] J. Wang, X. Guo, *Chemosphere* **2020**, *258*, 127279.
[35] C. Muschielok, A. Reiner, R. Röß-Ohlenroth, A. Kalytta-Mewes, D. Volkmer, A. Wixforth, H. Oberhofer, *ACS Appl. Mater. Interfaces* **2022**, *14*, 33662–33674.
[36] T. S. Jeong, P. Y. Yu, *J. Korean Phys. Soc.* **2000**, *36*(2), 102.
[37] T. Wagner, C.-D. Kohl, S. Morandi, C. Malagú, N. Donato, M. Latino, G. Neri, M. Tiemann, *Chem. Eur. J.* **2012**, *18*, 8216–8223.
[38] T. Wagner, C.-D. Kohl, C. Malagú, N. Donato, M. Latino, G. Neri, M. Tiemann, *Sens. Actuators B* **2013**, *187*, 488–494.
[39] L. Kothe, S. Ester, M. Poeplau, M. Wengenroth, M. Tiemann, *Proceedings 22. GMA/ITG-Fachtagung Sensoren Und Messsysteme* **2024**, *2024*, 66–71.
[40] M.-T. Tsai, Y.-S. Chang, Y.-C. Liu, *Ceram. Int.* **2017**, *43*, S428–S424.
[41] T. Hashemi, H. M. Al-Allak, J. Illingsworth, A. W. Brinkman, J. Woods, *J. Mater. Sci.* **1990**, *9*, 776–778.
[42] P. Scherrer, *Göttinger Nachrichten Math. Phys.* **1918**, *2*, 98–100.
[43] M. A. Becker, C. Bernasconi, M. I. Bodnarchuk, G. Rainò, M. V. Kovalenko, D. J. Norris, R. F. Mahrt, T. Stöferle, *ACS Nano* **2020**, *14*, 14939–14946.

Manuscript received: October 23, 2024
Revised manuscript received: January 9, 2025
Accepted manuscript online: January 14, 2025
Version of record online: January 24, 2025

ChemPhysChem

Supporting Information

Oxygen-Dependent Photoluminescence and Electrical Conductance of Zinc Tin Oxide (ZTO): A Modified Stern-Volmer Description

Linda Kothe, Josefin Klippstein, Marvin Kloß, Marc Wengenroth, Michael Poeplau, Stephan Ester, and Michael Tiemann*

Supporting Information

Characterization

This work focuses on the O_2-dependent photoluminescence and electrical conductance of zinc tin oxide (ZTO). The synthesis was inspired by Tsai et al.[40] As displayed in figure S1, Zn_2SnO_4 was obtained, with only low amounts of SnO_2.

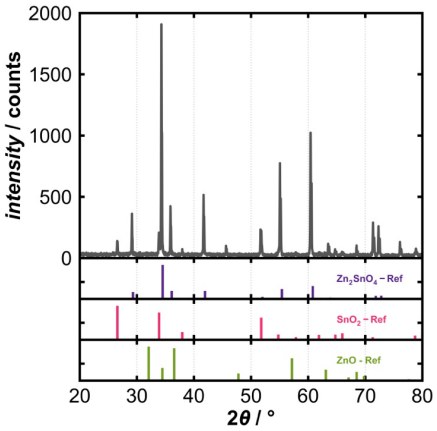

Figure S1. *x-ray diffraction pattern.*

An incomplete incorporation of SnO_2 is likely, since the formation of Zn_2SnO_4 is a solid-state reaction.[41] The most intense powder XRD reflection (311) at 34.30 ° was fitted with a linear combination of two gaussian functions, figure S2 and equation S1, to determine the center and full width at half maximum.

The (311) reflex of ZTO at 34.30 ° was fitted with a linear combination of two Gaussian functions, equation S1, as the Cu-$K_{\alpha,1}$ and Cu-$K_{\alpha,2}$ beam are not separated.

$$g(x) = A \frac{1}{\sigma\sqrt{2\pi}} exp\left(-\frac{1}{2}\left(\frac{x-\mu}{\sigma}\right)^2\right) \quad \text{(S1)}$$

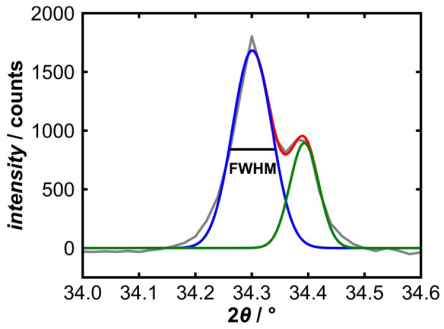

Figure S2. *magnification of x-ray diffraction (311) reflex at 34.30 °, fitted with a double gaussian function.*

Based on the Scherrer equation, the average crystallite size is 111.5 nm.[42]

This is consistent with scanning electron microscopy (SEM) images, figure S3a, as there are either smaller and bigger crystallites. Despite residual amounts of SnO_2, Zn and Sn are homogeneously distributed in the sample, figure S3b and c. Due to the different weights and resulting penetrations depths of X-rays, the topography of the particles is apparent in the energy dispersive X-ray spectroscopy (EDX) data.

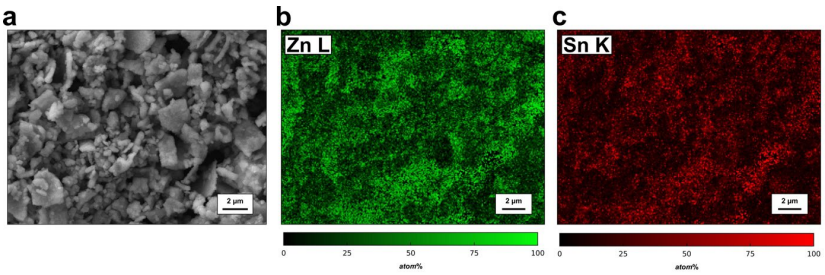

Figure S3. ***a*** *SEM image 5000 x magnification,* ***b*** *EDX mapping of Zn (green) and* ***c*** *Sn (red) in atom% 5000 x magnification.*

Excitation-Emission spectrum, figure S4a, and emission spectrum (λ_{ex} = 325 nm), figure S4b, at room temperature under ambient conditions of ZTO. The spectrum was fitted with a linear combination of two Gaussian functions. The two emission bands were also reported in the literature before.[22,23]

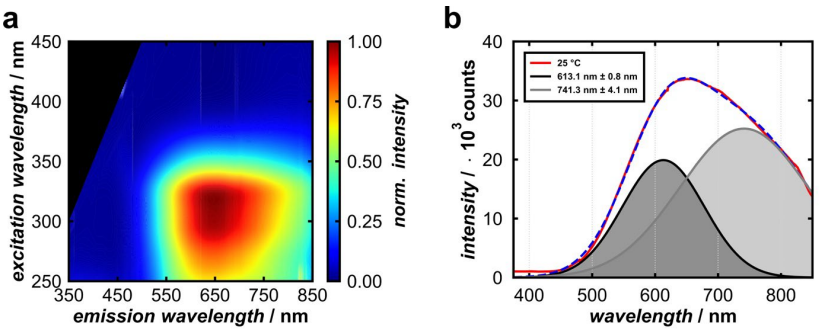

Figure S4. ***a*** *excitation-emission spectrum,* ***b*** *emission spectrum at room temperature fitted with a linear-combination of two Gaussian functions (λ_{ex} = 325 nm).*

The lifetime was determined at λ_{em} = 613 nm and 741 nm. Each measurement ("phosphorescence lifetime", λ_{ex} = 325 nm, excitation bandwidth = 5 nm, λ_{em} = 613 nm and 741 nm, emission bandwidth = 20 nm, 50 ms chopping period) was performed 10 times for each emission wavelength. One measurement is containing 100 measurements, which results in an average value of 1000 single measurements. As most solids don't show a single exponential decay behavior we evaluate the data in two different ways. The first method evaluates the time the intensity requires to reach a value of 1/e. A second method is based on the log-log scaling of the data, revealing an initial single exponential stage, followed by a finite stage, which can be fitted with a power law.[43] The slope of the power law might reveal additional information about different interactions, which can elongate the lifetime, e.g. exciton phonon interactions etc., but are not the focus of this work. We have chosen these methods to keep the determination of lifetimes as comparable as possible.

First the lifetimes at λ_{em} = 613 nm and 741 nm were determined under ambient (no active gas flow) conditions, figure S5a and b. Both evaluation methods reveal a longer lifetime of the 613 nm emission compared to 741 nm. In addition, the double-log scaling of the data indicate, that the emission at 613 nm might be more affected by additional interactions, as the elongation term is here much more pronounced. The effect of O_2 on the lifetime was then determined for both emission bands. The sample was kept in a pure N_2 or 20 vol% O_2 in N_2 atmosphere (300 ml/min) at room temperature for 1 h each before the measurements. The emission at 613 nm (Figure 2, Figure S5e) is quenched by O_2. In contrast the emission at 741 nm seems not to be quenched by O_2 (Figure S5c and S5d), which is subject for further studies.

4

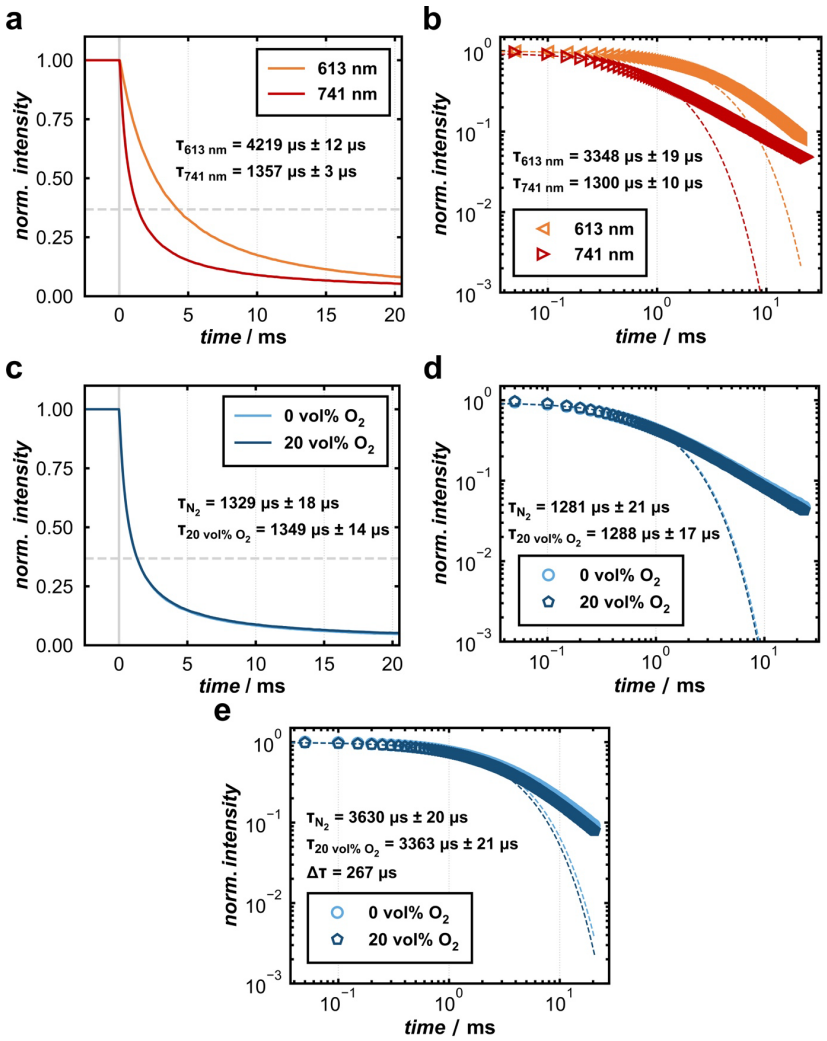

Figure S5. ***a*** *lifetimes at 613 nm and 741 nm (ambient conditions),* τ *is (1/e),* ***b*** *lifetimes at 613 nm and 741 nm (ambient conditions),* τ *from single exponential fit,* ***c*** *lifetimes at 741 nm in pure* N_2 *and 20 vol% O₂ in* N_2 *atmosphere,* τ *is (1/e),* ***d*** *lifetimes at 741 nm in pure* N_2 *and 20 vol% O₂ in* N_2 *atmosphere,* τ *from single exponential fit,* ***e*** *lifetimes*

at 613 nm in pure N_2 and 20 vol% O_2 in N_2 atmosphere, τ from single exponential fit. All excited with 325 nm.

Measurement Setup

On a ceramic substrate with a gold interdigital structure the conductance and photoluminescence (PL) of the drop-coated ZTO particles can be measured simultaneously with a custom-built setup. The measurement setup (figure S6a) is housed in an aluminum body to shield external light. The insert for a commercially available quartz glass cuvette (figure S6b) was constructed to measure PL and conductance at a controlled temperature and gas atmosphere. A type-K thermocouple is connected to a flue gas analyzer (Woehler A450) to determine the substrate temperature. An Agilent E3640A power supply was used for heating; the heating element is controlled by a Python script. A Roithner DUV325-HL46N LED, operated at 15 V with a Voltcraft LSP-1403 power supply, was used to excite the sample. The emitted radiation is collected with a collimator lens and transferred by optical fibers to an Ocean Optics Flame Miniature spectrometer. The gas atmosphere is mixed with a gas mixing system (Woehler GM450) and applied with a flow rate of 150 mL/min. The interdigital electrode structure is operated in series with a 1 MOhm resistor on a Voltcraft LSP-1403 power supply with a constant output voltage of 20 V. The conductance of the ZTO particles is calculated using the measured voltage (multimeter, HP 34401A) via the interdigital structure.

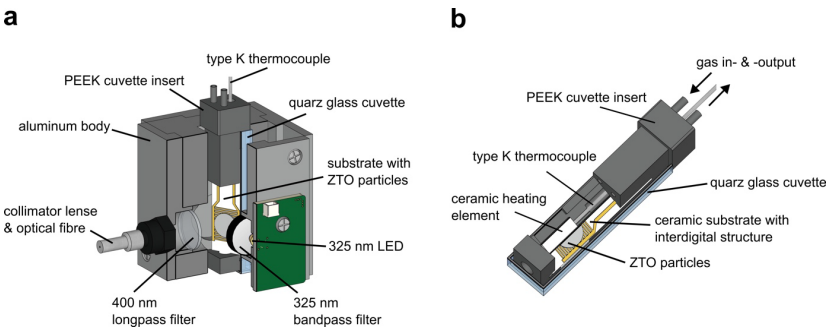

Figure S6. *Sectional drawings of **a** experimental setup to measure photoluminescence and conductance simultaneously at controlled temperatures and gas atmospheres, **b** the cuvette insert.*

Data Evaluation

For each emission spectrum the spectrometer integrates over 30 seconds. To evaluate the data, spectra are smoothed with a moving average of 20 measurement points. The spectral resolution is 0.473 nm. The emission spectrum of ZTO particles is displayed in figure S7. To evaluate the quencher impact, the intensity at 606 nm (vertical orange line) is determined for every spectrum and tracked over time.

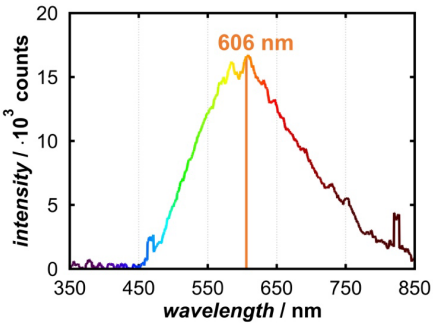

Figure S7. *emission spectrum of ZTO particles, 606 nm highlighted with vertical orange line, excited with 325 nm.*

Measurement Modes

Two different measurement modes were performed. During the first one, the O_2 concentration was kept constant during the measurement, and the temperature was varied. Then the temperature was kept constant during the measurement, and the O_2 concentration varied. For the first measurement mode (figure S8a), the temperature is varied in 0.5 vol%, 1 vol%, 2.5 vol%, 5 vol%, 10 vol%, 15 vol% and 20 vol% O_2 in N_2 atmospheres (150 ml/min). The temperature sequence starts with a 150 °C segment for 2 h, followed by a temperature decrease to 40 °C in 10 °C steps. Each temperature is kept constant for 30 min. Finally, an additional segment at 150 °C is applied for 15 min. The second measurement mode (figure S8b) is operated at 40 °C, 80 °C, 120 °C and 160 °C. After a 4 h N_2 segment the O_2 concentration is varied from 0.5 vol% to 20 vol% for 1 h each (150 ml/min). The measurements performed to determine the lower detection limit were performed at 120 °C. After a 4 h N_2 segment the O_2 concentration varied from 0.33 vol% to 0.7 vol% for 1 h each (300 ml/min).

8

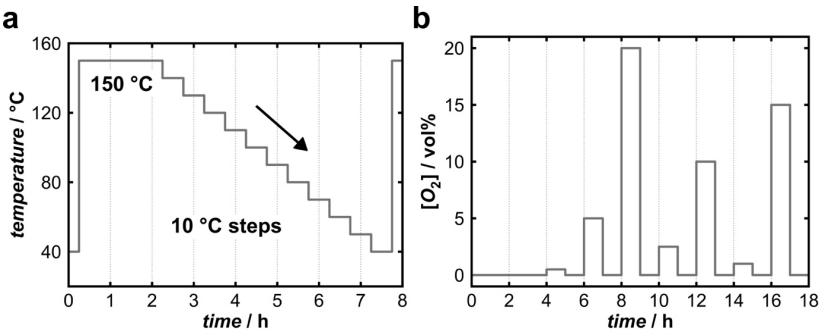

Figure S8. ***a*** *temperature profile under constant O_2 concentration,* ***b*** *concentration profile at constant temperatures*

Temperature variation (0% to 20 vol% O_2 in N_2)

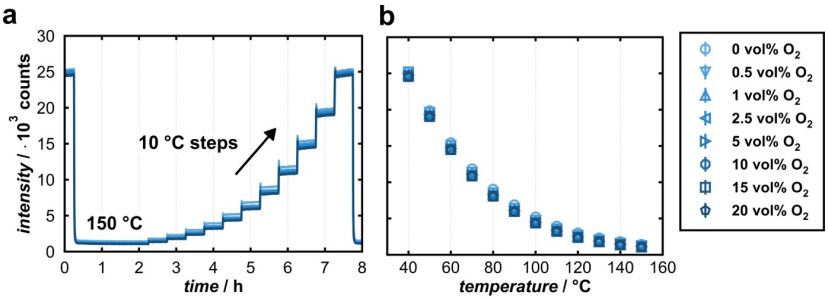

Figure S9. ***a*** *temperature profile under constant O_2 concentration,* ***b*** *concentration profile at constant temperatures.*

Derivation of Modified Stern-Volmer Equation

$$f_a = \frac{I_{0,a}}{I_0} \rightarrow I_{0,a} = f_a I_0 \quad \text{(S2)}$$

$$I_0 = I_{0,a} + I_{0,b} \quad \rightarrow \quad I_{0,b} = I_0 - f_a\, I_0 \tag{S3}$$

$$I_Q = \frac{I_{0,a}}{1 + K_a[O_2]} + I_{0,b} \tag{S4}$$

$$I_Q = \frac{f_a I_0}{1 + K_a[O_2]} + I_0 - f_a\, I_0 \tag{S5}$$

$$I_Q = I_0 \left(\frac{f_a}{1 + K_a[O_2]} + 1 - f_a\right) \qquad | : I_0 \tag{S6}$$

$$\frac{I_Q}{I_0} = \frac{f_a}{1 + K_a[O_2]} + 1 - f_a \qquad | - 1 \tag{S7}$$

$$\frac{I_Q}{I_0} - 1 = \frac{f_a}{1 + K_a[O_2]} - f_a \qquad | \cdot (-1) \tag{S8}$$

$$1 - \frac{I_Q}{I_0} = f_a - \frac{f_a}{1 + K_a[O_2]} \tag{S9}$$

$$\frac{I_0}{I_0} - \frac{I_Q}{I_0} = f_a \left(1 - \frac{1}{1 + K_a[Q]}\right) \qquad | : f_a \tag{S10}$$

$$\frac{I_0 - I_Q}{I_0 f_a} = \frac{1 + K_a[Q]}{1 + K_a[Q]} - \frac{1}{1 + K_a[Q]} = \frac{1 + K_a[Q] - 1}{1 + K_a[Q]} = \frac{K_a[Q]}{1 + K_a[Q]} \qquad | \cdot f_a \tag{S11}$$

$$\frac{I_0 - I_Q}{I_0} = \frac{f_a K_a[Q]}{1 + K_a[Q]} \qquad | (\,)^{-1} \tag{S12}$$

$$\frac{I_0}{I_0 - I_Q} = \frac{1 + K_a[Q]}{f_a K_a[Q]} = \frac{1}{f_a K_a[Q]} + \frac{K_a[Q]}{f_a K_a[Q]} = \frac{1}{f_a K_a[Q]} + \frac{1}{f_a} \tag{S13}$$

10

Conductance & Photoluminescence Measurements

The conductance was normalized on the maximum value at each temperature, table S1.

Table S1. Maximum conductance between 40 °C and 160 °C.

temperature / °C	conductance / nS
40	352.87
80	426.98
120	596.00
160	1046.42

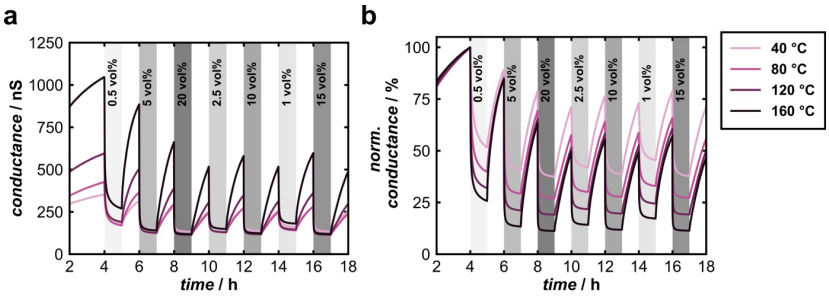

Figure S10. *O_2 dependent conductance between 40 °C and 160 °C **a** as measured, **b** normalized.*

The intensity was averaged between 3 h and 4 h and used for normalization at each temperature, table S2.

Table S2. Maximum intensity between 40 °C and 160 °C.

temperature / °C	intensity / counts
40	33039
80	16493
120	6586
160	2541

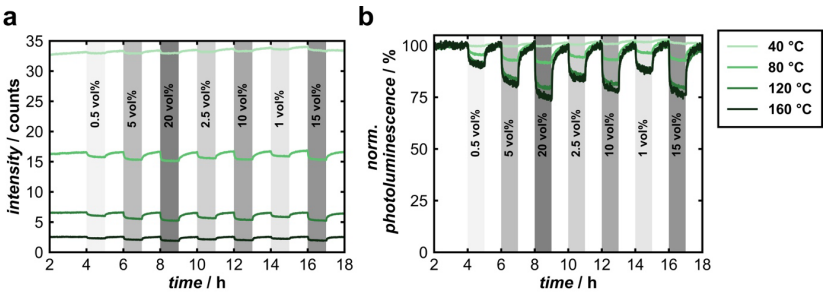

Figure S11. *O_2 dependent photoluminescence between 40 °C and 160 °C* ***a*** *as measured,* ***b*** *normalized.*

From the measurements displayed in Figure 6 the characteristic curves at the different operating temperatures were extracted for conductance and photoluminescence.

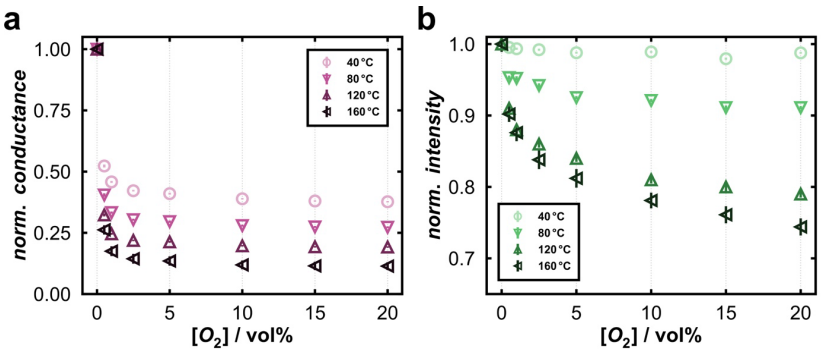

Figure S12. *O_2 dependent responses for **a** conductance and **b** photoluminescence between 40 °C and 160 °C.*

Table S3. Maximum conductance at 160 °C with and without optical activation.

optical activation	conductance / nS
325 nm	1046.42
without	140.19

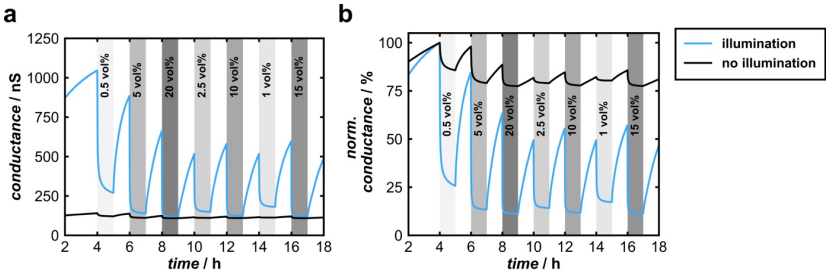

Figure S13. *O_2 dependent conductance at 160 °C with illumination by 325 nm LED (light blue) and without illumination (black) **a** as measured, **b** normalized.*

Determination of lower detection limit from simultaneous measurement of photoluminescence and conductance. Lower O_2 concentrations could not be measured due to the current gas mixing equipment.

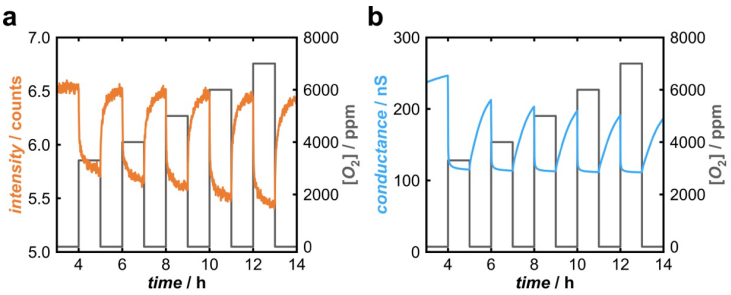

Figure S14. *photoluminescence **a** and conductance **b** measured simultaneously at 120 °C at different O_2 concentrations (3300 ppm to 7000 ppm).*

Table S4. Maximum intensity and conductance at 120 °C.

intensity	6530 counts
conductance	245.84 nS

3.2 Temperature Dependent Photoluminescence

The Stern-Volmer studies provided insight into the sensing mechanism of photoluminescence (PL) O_2 sensing with metal oxides. Furthermore, the considerable impact of the operating temperature was substantiated, necessitating further investigation to explore its implications. Of particular interest in the present study were the effects on the emission spectrum and lifetime, as well as O_2 sensitivity.

The study consisted of measuring the emission spectra of zinc tin oxide (Zn_2SnO_4, ZTO) at varying operating temperatures. It was demonstrated that the emission spectra exhibited an orange and red component, which overlapped. The emission energies of the two transitions were evaluated separately, revealing a general increase in emission energy with rising operating temperature. The emission lifetimes also underwent a considerable temperature-induced quenching effect. The temperature dependent intensity quenching course was modeled with a function derived from Fermi–Dirac statistics. The parameters included in the formula indicated the positions of defect levels in the band gap of ZTO. The presence of O_2 resulted in an observable alteration in the defect level position. The individual evaluation of the orange and red emission suggested that the orange emission was more impacted by the presence of O_2. The assumption was further confirmed by simultaneous measurements of PL and conductance at varying O_2 concentrations.

L. Kothe, M. Kloß, T. Wagner, M. Wengenroth, M. Poeplau, S. Ester, M. Tiemann, *Temperature Studies of Zinc Tin Oxide Photoluminescence for Optical O_2 Sensing*, J. Phys. Chem. C **2025**, 129, 9239-9245

- DOI: 10.1021/acs.jpcc.5c01678

Participation in this Publication

L.K., M.T. and M.P. conceived the project. L.K. was in charge of the experimental work, data analysis and writing of the manuscript with contributions of all authors. M.W. constructed the temperature regulation. S.E. contributed to the critical scientific discussions about the measurements and the temperature fitting. M.K. and T.W. performed the PXRD measurements.

THE JOURNAL OF PHYSICAL CHEMISTRY C
A JOURNAL OF THE AMERICAN CHEMICAL SOCIETY
pubs.acs.org/JPCC
Article

Temperature Studies of Zinc Tin Oxide Photoluminescence for Optical O_2 Sensing

Linda Kothe, Marvin Kloß, Tobias Wagner, Marc Wengenroth, Michael Poeplau, Stephan Ester, and Michael Tiemann*

Cite This: J. Phys. Chem. C 2025, 129, 9239−9245
Read Online
ACCESS | Metrics & More | Article Recommendations | Supporting Information

ABSTRACT: The photoluminescence of zinc tin oxide (ZTO) is investigated regarding its temperature (room temperature to 433 K) and gas-phase oxygen (O_2) concentration (250 ppm to 20 vol %) dependence. Both the emission intensity and electrical conductance decrease upon O_2 adsorption, as ZTO is an n-type semiconductor. A temperature increase significantly quenches the photoluminescence intensity and results in a strong blue-shift of the orange and red emission. The temperature-induced exponential intensity decay can be described with an empirical equation similar to the Fermi−Dirac statistic. The obtained activation energies allow to propose a detailed band scheme of ZTO.

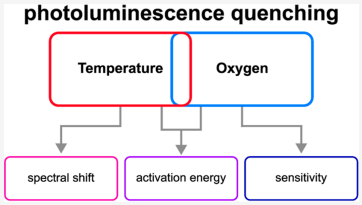

INTRODUCTION

Optical gas sensing with metal oxides has become more relevant in recent years as new applications for contactless detection are increasingly developed.[1,2] Contactless oxygen (O_2) detection is relevant, for example, in biological systems, to monitor air quality or safety-critical compositions.[3−5] Although photoluminescence-based sensors typically contain metal−organic compounds, metal oxides have also been part of the research.[6] It has been shown that established metal oxides used in resistive gas sensing, such as titanium dioxide (TiO_2), zinc oxide (ZnO), or lanthanoid-doped zirconium oxide (ZrO_2), also have great potential for photoluminescence O_2 sensing.[7,8]

In photoluminescence gas sensing, the metal oxide is excited with radiation that has a higher energy than the band gap, which is usually in the UV range and its resulting photoluminescence, mostly in the visible range, is detected. The same physical principles apply to this system as to a light-activated resistive gas sensor; the ionosorption model is valid. For an *n*-type semiconductor, O_2 chemisorbs on the surface, which traps electrons from the conduction band and reduces the conductance; the intensity and lifetime of the emission, i.e., photoluminescence and conductance, are considered quasi-proportional.[9,10] With increasing O_2 concentration, the depletion layer becomes thicker, and the surface potential increases.

In this study, we investigate the photoluminescence of zinc tin oxide (Zn_2SnO_4, ZTO) regarding its temperature and O_2 dependence. ZTO is an *n*-type semiconductor that is transparent in the visible range and has a band gap in the UV range.[11] It can be synthesized, for example, by a solid-state reaction of ZnO with SnO_2 or through solvothermal reaction.[12−14] Here, we chose a sol−gel-based approach, followed by thermal conversion, which was inspired by Tsai et al. but further refined.[15] Reported applications of ZTO include transistors,[16,17] photocatalysts,[18,19] optoelectronic compounds,[20,21] solar cells[22] or gas sensors.[23−25] In the literature, three emission bands of ZTO are reported: blue-green (497 nm, 2.49 eV), orange (606 nm, 2.05 eV), and red (740 nm, 1.68 eV).[26−28] The green emission might be related to oxygen vacancies; the orange and red transitions are likely caused by interactions of oxygen vacancies and interfacial tin or zinc vacancies. In our products, only the orange and red emissions are present. With increasing measurement temperature, the intensity of the emissions decreases, which is most likely described by a Schön−Klasens mechanism.[29−31] The temperature-induced quenching can be described by the empirical eq 1 which assumes that the emission intensity is constant at low temperatures until quenching is induced at a critical temperature. In the equation, $I(T = 0)$ is the intensity at 0 K, C is a dimensionless constant, E_{act} is the activation energy, k_B is Boltzmann's constant, and T is the temperature.

$$I(T) = \frac{I(T=0)}{1 + C\cdot\exp\left\{-\frac{E_{act}}{k_B T}\right\}} \quad (1)$$

Received: March 12, 2025
Revised: April 28, 2025
Accepted: April 30, 2025
Published: May 6, 2025

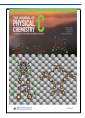

https://doi.org/10.1021/acs.jpcc.5c01678
J. Phys. Chem. C 2025, 129, 9239−9245

It should be noted that this equation is very similar to the Fermi−Dirac distribution, eq 2.[32] Here f_0 is the probability of occupation, E the energy of the conduction band, E_F the Fermi level, k_B Boltzmann's constant and T the temperature.

$$f_0(E, E_F, T) = \frac{1}{1 + \exp\left\{-\frac{E - E_F}{k_B T}\right\}} \quad (2)$$

The investigation of the temperature-dependent orange and red emission could lead to a better understanding of the band structure of ZTO and further clarify the mechanism of photoluminescence gas sensing.

EXPERIMENTAL SECTION

Synthesis of ZTO Powder. 92 μL ethylene glycol (≥98%, VWR), 34.7 g diethanolamine (0.33 mol, synthesis quality, VWR) and 150 mL pure ethanol (≥99.5%, VWR) were stirred for 15 min 15.7 g zinc(II)acetate dihydrate (0.066 mol, 98%; VWR) and 3.9 mL anhydrous tin(IV)chloride (0.033 mol, 99%, VWR) were added. The solution was refluxed for 1 h and cooled to room temperature. The thus-obtained clear dispersion (sol) was aged for 7 days at room temperature in the dark. For gelation 300 mL water was added and stirred for an additional 15 min. The white dispersion was centrifuged (4000 rpm, 30 min) and the remaining gel was washed twice with water. The gel was dried for 72 h at 150 °C. The residue was grinded for 5 min. Two g of the solid were annealed at 1100 °C for 6 h (300 °C/h), followed by grinding. For sensor preparation, substrates (ceramic or quartz glass) were cleaned with acetone and ethanol and dried at 80 °C. The product was dispersed in water (0.04 mg/μL). The ceramic substrates were drop-coated twice with 150 μL of the dispersion and completely dried at 80 °C. The quartz glass substrates were masked with tape (ca. 1 cm × 1 cm unmasked area), drop-coated once with 100 μL and subsequent drying at 80 °C.

Characterization. Powder X-ray diffraction patterns were recorded with a Bruker D8 Advance diffractometer (Cu−K_α, 0.02° steps, 3 s illumination time). Transmittance spectra were recorded with a PerkinElmer Lambda 650 in combination with a Harrick praying mantis. Below 319.2 nm a deuterium lamp (250−319 nm) and above 319.2 nm a tungsten lamp (319−800 nm) was used. The wavelength range was 250−800 nm with an integration time of 1 s/nm. Barium sulfate ($BaSO_4$) was used as a reference for 100% transmittance. The excitation−emission spectra (2 nm steps), emission spectra and lifetime measurements (excitation bandwidth = 5 nm, emission bandwidth = 20 nm, 50 ms chopping period) were recorded with a JASCO 8550. Scanning electron microscopy was performed with a Zeiss Neon 40.

RESULTS & DISCUSSION

Temperature-Induced Photoluminescence Quenching. The synthesized ZTO was characterized with powder X-ray diffraction (PXRD), scanning electron microscopy (SEM), energy dispersive X-ray spectroscopy (EDX) and UV/vis spectroscopy, see Supporting Information Figure S1−S4, Table S1 and eqs S1−S5. Powder X-ray diffraction analysis suggests no crystalline impurities in the synthesized ZTO (Zn_2SnO_4). Calculated crystallite sizes obtained from the Scherrer equation suggest domains of 120.8 nm ± 7.8 nm. SEM images reveal a nonspecific particle morphology. The transmittance data show values around 90% in the visible range. Below 450 nm, photon absorption increases. Optical band gaps for direct (3.70 eV ± 0.07 eV) and indirect (3.38 eV ± 0.03 eV) transitions are obtained from the Kubelka−Munk function and Tauc plot. The indirect band gap results from the Urbach tails (E_U 149.7 ± 0.7 meV), which extend into the band gap.

The excitation−emission spectrum (Figure S5) reveals visible photoluminescence (PL) in the orange and red range. When excited with 325 nm, the PL intensity is maximized, which is why the following studies were performed with an excitation wavelength of 325 nm. To control the sample temperature, a cuvette insert (Figure S6a) was used. The single emission spectrum (Figure 1) is asymmetric and consists of two overlapping emission bands. As previously mentioned, the orange and red transitions are likely caused by interactions of oxygen vacancies and interfacial tin or zinc vacancies. Higher energetic transitions in the blue-green range are linked to oxygen vacancies but were not observed.[26−28]

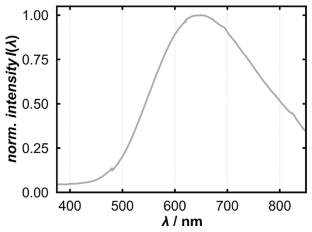

Figure 1. Emission spectrum (gray line) of ZTO in pure N_2 atmosphere at 313 K.

These results allow us to propose a band scheme for ZTO, as depicted in Figure 2. The surface-near region of the metal

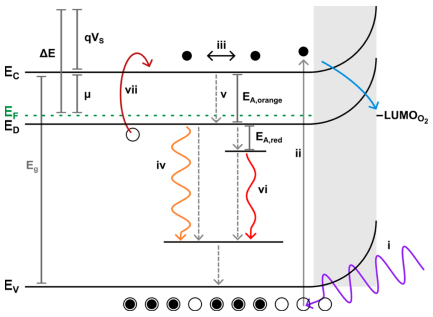

Figure 2. Proposed band scheme of ZTO in the photon penetrating area, separated in dead layer (light gray) and photoluminescence-active region (white). (i) UV irradiation, (ii) excitation of electrons from valence to conduction band, (iii) electron mobility in the conduction band, (iv) radiative and nonradiative recombination to donor state (orange), (v) radiative and nonradiative recombination to acceptor state, (vi) radiative and nonradiative recombination from deep donor state to acceptor state (red), (vii) thermal activation from donor state to conduction band. Gray dashed arrows represent nonradiative transitions.

https://doi.org/10.1021/acs.jpcc.5c01678
J. Phys. Chem. C 2025, 129, 9239−9245

oxide is crucial regarding relaxation processes, which result in emission and gas sensing. Electromagnetic radiation (i) with an energy larger than the band gap E_g (3.7 eV) of the semiconductor can excite electrons from the valence to the conduction band (ii). The electrons in the conduction band are mobile (iii) and can participate in radiative and nonradiative recombination (iv) to a donor state, establishing the *n*-type semiconducting character. From this donor state, radiative and nonradiative recombination to an acceptor state (v) occurs. From a deeper donor state to the acceptor state, radiative and nonradiative recombination (vi) could also be possible, potentially resulting in longer emission wavelengths. The spatial separation of electrons moving into the bulk and holes moving to the surface creates a space-charge layer at the surface.[33] In this area, the recombination rates are reduced by the near-surface electric field; a surface photovoltage occurs and band-bending is reduced. This area is called the "dead layer" and is equivalent to the electron depletion layer. Radiative recombination is possible only if the energy of the donor state is lower than the Fermi energy; thus, the thickness of the space-charge layer is defined as the depth where these energies are equal.[34] In the presence of O_2, photoexcited electrons are trapped at the surface due to O_2 chemisorption and are unable to participate in radiative recombination. Thus, the PL intensity decreases; it is quenched. Band-bending to higher energies occurs, the thickness of the dead layer or depletion layer increases, and the Fermi energy decreases.[33] Thereby, the energy difference between the conduction band and the Fermi energy μ remains constant. If the surface is saturated with O_2, the Fermi energy is equal to the LUMO (lowest unoccupied molecular orbital) of O_2. As shown previously, the PL-active region underneath the dead layer is also affected by O_2, but only a fraction of photoelectrons interacts with O_2.[35] The surface potential V_S, which is also referred to as Schottky barrier, describes the height of the depletion layer, i.e., the energy difference between the conduction band in the bulk and the upper conduction band at the surface. An increase in temperature elevates electrons from the donor state back to the conduction band (vii). Thus, resulting in an increased conduction and a decrease in PL intensity.

We first focus solely on the temperature dependence of photoluminescence in pure N_2. With increasing temperature, the emission intensity of ZTO decreases significantly and will be discussed in detail in section "Oxygen effect on Photoluminescence". We note that the substrates used may also contribute to photoluminescence, as shown in the Supporting Information section (Figure S7+S8). For this spectral evaluation, quartz glass substrates were used (Figure S9). The obtained spectra were converted from a wavelength to an energy scale (eqs S6−S10 + Figure S10) and were fitted on the reciprocal energy scale in good agreement with a combination of two Gaussian functions (eq S1). From the fitted spectra, the amplitudes, peak positions, peak widths, and peak areas are determined for the orange and red emission bands, respectively, see Figure S11 and Tables S2 and S3.

Regarding photoluminescence, temperature-induced quenching reveals that nonradiative recombination instances become more dominant, with increasing temperature. It is likely that additional nonradiative transitions become possible; therefore, we assume a Schön-Klasens mechanism. Here, multiple centers—radiative and nonradiative centers—participate in the thermal emission of electrons or holes. The activation energy is considered to be the ionization energy of an acceptor state (thermal emission of holes to the valence band) or donor state (thermal emission of electrons to the conduction band).[29]

Figure 3 shows the obtained peak positions from the fits for the orange and red emission, converted to energy and plotted

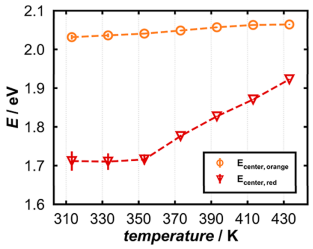

Figure 3. Orange and red emission energy of ZTO. For all data, the excitation wavelength is 325 nm, the temperature range between 313 and 433 K and the atmosphere pure N_2. (The dashed lines serve as a guide for the eye only.)

in dependence on temperature. It is revealed that with increasing temperature, both emission energies become larger. The orange emission energy slightly increases with temperature and, after an abrupt increase in emission energy at 373 K, seems to stay constant. The red emission energy stays constant up to 353 K and then significantly increases with temperature. Over a course of 60 K, the peak position shifts by approximately 200 meV. This shift can be explained by the proposed band scheme shown in Figure 4a. At room

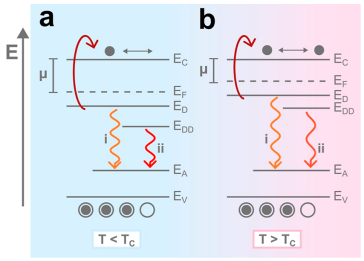

Figure 4. Proposed band scheme of ZTO. (a) Below T_C (critical temperature), orange and red emission coexist, with incomplete thermal activation of the donor state E_D; E_D approaches E_C. (b) Above T_C, the thermal activation of the deep donor state E_{DD} increases significantly, E_{DD} approaches E_D.

temperature or below a critical temperature T_C, the orange and red photoluminescence occur simultaneously. After excitation, the photoelectron of the orange emission starts at the donor state E_D and recombines with a hole in an acceptor state E_A (i); the red emission originates from a deeper donor state E_{DD} (ii) but assumingly also recombines with the acceptor state.[36] It should be noted that the donor states are not completely thermally activated at room temperature. The

https://doi.org/10.1021/acs.jpcc.5c01678
J. Phys. Chem. C 2025, 129, 9239−9245

occupancy of electrons in the conduction band of a donor state can be described with eq 3, where n is the density of electrons, N_C the effective density of states, E_C the conduction band edge, E_F the Fermi level, k_B Boltzmann's constant, and T the temperature. This equation is valid if $E_C - E_F > 2k_BT$.[20]

$$n = N_c \cdot \exp\left[\frac{-(E_C - E_F)}{k_B T}\right] \quad (3)$$

In the case of ZTO, $E_C - E_F$ can be estimated from literature data as approximately 0.3 eV; thus, at room temperature ($2k_BT \approx 50$ meV), eq 3 is a valid assumption.[37,38] When the temperature increases, the Fermi level approaches the conduction band, resulting in a higher electron density, which is directly proportional to the conductance. After the critical temperature is exceeded (Figure 4b) the data might indicate that with increasing temperature, first, the donor state (E_D) approaches the conduction band (E_C), which results in a small blue shift of the orange emission, while the energy of the red emission stays constant. After the critical temperature is exceeded, electrons from the deep donor state are increasingly elevated to the donor state, which results in an abrupt blue shift of both emission energies. If the temperature increases further, the deep donor state further approaches the donor state. The energy difference between E_D and E_{DD} at is *ca.* 320 meV at 313 K, and *ca.* 150 meV at 433 K. This shift is completely reversible, which further supports our assumption that it is only temperature-induced.[39]

The lifetimes were measured at the peak positions for the orange and red emission bands, which were obtained from the Gaussian fits (Figure 5). With increasing temperature (298–333 K), both lifetimes first drop significantly, with the orange emission lasting much longer than the red one. At 353 K, both lifetimes are very similar, and above 373 K, the lifetime of the red emission becomes longer than the orange one. Although both lifetimes are quenched by temperature, the orange emission decreases especially between 313 and 353 K. At 373 K, the lifetime of the red emission shows a local maximum. This coincides with the just described mechanistic change, i.e., the strong blue shift of the red emission. The energetic elevation of the deep donor state and the enhanced thermal activation of the electrons might elongate the lifetime of the red emission. This is supported by the fact that the lifetimes between 373 and 433 K are longer than at 333 and 353 K. It should be noted that the emission lifetimes were also measured in a 20:80 vol % O_2/N_2 atmosphere (see Supporting Information section, Figures S12 and S13). Regarding our measurements, the lifetime was not significantly affected by O_2 except for the measurement at room temperature. As this was a reproducible circumstance, we assume that changes in the lifetimes were too small to be resolved. However, these studies are outside the scope of this work.

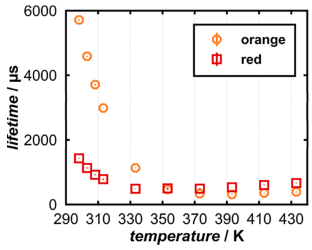

Figure 5. Lifetimes of orange and red ZTO emission, measured at the respective peak positions (pure N_2) between 298 and 433 K. For all data the excitation wavelength is 325 nm.

Oxygen Effect on Photoluminescence. As described above, the photoluminescence intensity is quenched not only by an increase of temperature but also by O_2 chemisorption. Although a small intensity change can be measured with the JASCO fluorometer (see Supporting Information section, Figure S9), we chose our custom measurement setup (Figure S6) for intensity evaluation for reasons of higher sensitivity. The intensities at 606 and 730 nm were tracked over time (Figure S14), while the gas atmosphere remained constant and the temperature varied in a sequence (Figures S15a, S16 and S17).

For the orange emission (606 nm), differences in temperature dependencies are revealed when the temperature is varied in pure N_2 and in O_2-containing atmospheres (20 vol % O_2 in N_2; Figure 6). The data show that at every measured temperature, the intensity in pure N_2 is higher than in an O_2-containing atmosphere, confirming O_2-induced quenching. This is further highlighted in Figure S16a, where the complete intensity course is shown. To gain a deeper understanding of temperature quenching, eq 1 was used to fit the experimental data.

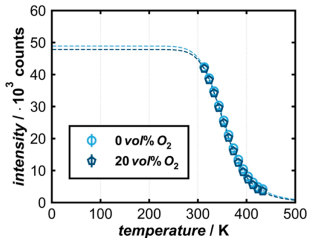

Figure 6. ZTO emission intensity at 606 nm in pure N_2 (light blue) and 20 vol % O_2 in N_2 (dark blue), fitted with eq 1.

The characteristics and assumptions of this model are that the photoluminescence intensity is constant at low temperatures and decreases once a critical temperature is reached. As this type of fitting is typically used for low-temperature emission studies, we calculated the first derivative (eq S11; Figure S16b) to further confirm the nature of the data. The data lie around the inflection point of eq 1 and therefore represent the local minimum of the first derivative. The fit parameters (Table 1) reveal that they all change in the presence of O_2. The value of $I_{(T=0\ K)}$ is 1067 counts higher in pure N_2 than in 20 vol % O_2, which is in accordance with the mechanism for O_2 sensing, as electrons are trapped by chemisorbed O_2 and are unable to participate in radiative recombination. It can be considered that C is antiproportional to the internal quantum efficiency η_0 (eq 4). The increase of C might therefore be explained by a decrease in quantum efficiency due to O_2 chemisorption as well.[29]

https://doi.org/10.1021/acs.jpcc.5c01678
J. Phys. Chem. C 2025, 129, 9239−9245

Table 1. Fit Parameters and Critical Temperature of Orange (606 nm) and Red (730 nm) ZTO Emission in Pure N_2 and 20 vol % O_2 in N_2

emission wavelength/nm	$[O_2]$/vol %	$I_{(T=0\ K)}$/counts	C	E_{act}/meV	$T_{I(T\neq 0K)}$/K
606	0	48,901 ± 287	779,032 ± 75,155	415 ± 3	193
	20	47,834 ± 344	1,589,241 ± 204,210	436 ± 4	197
730	0	32,862 ± 614	75,579 ± 5369	309 ± 3	161
	20	32,170 ± 640	98,254 ± 7973	317 ± 3	164

$$C \propto (1 - \eta_0) \tag{4}$$

The most interesting fitting parameter is the activation energy. The energy difference in a pure N_2 atmosphere and 20 vol % O_2 is 21 meV. Based on the band scheme (Figure 2), this activation energy can be regarded as the energy difference between the conduction band and donor state, in which case it contains the Fermi level and Schottky barrier. This also fits well with the basis of the Schön-Klasens mechanism, where the activation energy is assumed to be the ionization energy of a donor state. The Fermi level for ZTO was reported to be approximately 0.3 eV.[37,38] Since we applied a different synthesis method, the Fermi level for our ZTO may be slightly different but in a comparable value range. To our knowledge, the O_2-induced band bending of ZTO has not been reported so far. Reports on SnO_2 suggest a band bending of approximately 130 meV at 673 K in 5 vol % O_2. We expect lower values at significantly lower operation temperatures and gas flow. From resistive measurements at 393 K (Figure S18), band bending can be estimated for ZTO via a simplified Schottky model.[40] The estimated change in band bending in a N_2 atmosphere containing 20 vol % O_2 is approximately 6.3 meV (Figure 7). Above 5 vol % O_2, the change in band bending is nearly constant, which indicates saturation. This change in band bending is in the same order as the error of the Gaussian fittings presented in Figure 3, which may explain why no spectral shift in the presence of O_2 is detected. In contrast, a change of 21 meV may therefore be the maximal change of band bending induced by O_2 chemisorption at significantly higher operating temperatures. Additionally, it should be noted that the activation energy of the orange emission is very similar to the energy difference of the orange and previously described green-blue emission, which was also reported in the literature (497 nm: 2.49 eV, 606 nm: 2.05 eV, ΔE = 440 meV).[26−28] This indicates that the green-blue emission could be a radiative path between the conduction band and an acceptor state.

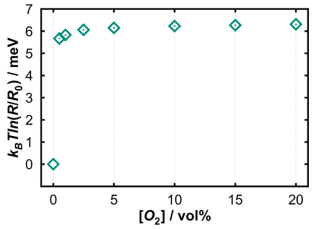

Figure 7. Change of ZTO band bending between 0.5 vol % and 20 vol % O_2 in N_2. Measured at 393 K, excited with 325 nm LED.

The intensity of the red emission (730 nm) is just slightly affected by the presence of O_2 (Figure S17) and the fit parameters show a similar picture. The values for $I_{(T=0K)}$ in pure N_2 are approximately 700 counts higher than in the O_2-containing atmosphere, but the error, which results from the accuracy of the fits, is in the same order. C increases in the presence of O_2, which also indicates a decrease in quantum efficiency. The activation energy in 20 vol % O_2 is 8 meV higher than in pure N_2, which is also just slightly higher than the calculated error. This altogether indicates that the orange emission is more affected by the chemisorption of O_2. It should be stressed that the values of the activation energies are very similar to the energy difference of the orange and red emission shown in Figure 3, further confirming that the obtained activation energy is the energy difference between the deep donor and donor state. As this activation energy is also lower than the activation energy of the orange emission, this is in alignment with the temperature-induced spectral shifts. With increasing temperature, the deep donor state is approaching the donor state and when they overlap, both are probably approaching the conduction band, which is expected for significantly higher temperatures and beneficial for, e.g., resistive gas sensing. The critical temperature $T_{I(T\neq 0K)}$ at which the intensity starts to decrease is approximately 30 K higher for the orange emission than for the red one, but both are enhanced similarly due to O_2 chemisorption.

For a better comparison of the O_2-induced photoluminescence change of the orange and red emissions, we performed measurements at 393 K with O_2 concentrations ranging from 250 ppm to 20 vol %, see Supporting Information (Tables S6, S7 and Figures S19, S20). The sensitivity S (eq 5), was determined, where $I_{[O2]}$ was the normalized intensity at the respective O_2 concentration.[41]

$$S = 100 - I_{[O_2]} \tag{5}$$

The logarithmic plot of the sensitivity (Figure 8) shows that the sensitivity of the orange emission intensity is significantly larger at every O_2 concentration than that of the red emission. With increasing O_2 concentration, this trend becomes more

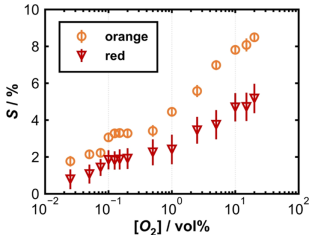

Figure 8. Sensitivity of the orange (606 nm) and red (730 nm) emission intensity between 250 ppm and 20 vol % O_2 in N_2. Measured at 393 K, excited with 325 nm LED.

https://doi.org/10.1021/acs.jpcc.5c01678
J. Phys. Chem. C 2025, 129, 9239−9245

pronounced. This is in alignment with the above-discussed change of activation energy, which is also significantly higher for the orange emission than for the red one. This suggests a correlation between the sensitivity and the change of the activation energy and would be in alignment with classical resistive gas sensing mechanisms.

CONCLUSION

The photoluminescence of semiconducting zinc tin oxide (ZTO) was investigated regarding its temperature and oxygen (O_2) quenching. The emission spectrum consists of an orange and a red emission band, which are both blue-shifted with increasing temperature. The temperature-dependent intensity fitting, which is based on the Fermi−Dirac statistic, reveals the activation energies of the orange and red emissions. These results provide an important contribution to understanding the band structure of ZTO. Variation of the O_2 concentration (250 ppm−20 vol %) demonstrates that the orange emission is more sensitive to O_2 than the red one. The different sensitivities show which transitions are influenced by the O_2 adsorption and thus help to better understand the sensor mechanism.

ASSOCIATED CONTENT

Supporting Information

The Supporting Information is available free of charge at https://pubs.acs.org/doi/10.1021/acs.jpcc.5c01678.

X-ray diffraction pattern of ZTO (Figure S1); Gaussian function (Equation S1); double Gaussian fit of (311), (511) and (440) reflexes (Figure S2); Scherrer equation (Equation S2); Reflex parameters and crystallite sizes (Table 1); SEM and EDX images of ZTO (Figure S3); Function of reflectance (Equation S3); function of absorption (Equation S4); linearized function of absorption (Equation S5); UV/vis data of ZTO (Figure S4); excitation−emission spectrum of ZTO (Figure S5); measurement cell and setup (Figure S6); emission spectra of substrates (Figure S7); emission of ZTO on ceramic and quartz glass substrates (Figure S8); emission spectra of ZTO between 313 and 433 K in pure N_2 and 20 vol % O_2 in N_2 (Figure S9); conversion of wavelength in energy (Equation S6); energy conversion of energy and wavelength dependent spectra (Equation S7); Jacobian Transformation (Equation S8); conversion of wavelength to reciprocal energy scale (Equation S9); emission peak position in wavelength from reciprocal energy (Equation S10); comparison of spectra conversion to the energy scale (Figure S10); emission spectra of ZTO between 313 and 433 K in pure N_2 fitted with double Gaussian fit (Figure S11); fit parameters of 1. Gaussian function (Table S2); fit parameters of 2. Gaussian function (Table S3); lifetime of ZTO at 298 K in pure N_2 and 20 vol % O_2 in N_2 (Figure S12); lifetimes of orange and red emission between 298 and 433 K in pure N_2 and 20 vol % O_2 in N_2 (Figure S13); Peak position in wavelength and lifetime of orange emission (Table S4); Peak position in wavelength and lifetime of red emission (Table S5); emission spectrum of ZTO in measurement setup (Figure S14); temperature and gas programs (Figure S15); intensity course and 1. Derivative of temperature dependent intensity at 606 nm (Figure S16); 1. Derivative of eq 1 (Equation S11); intensity course, fit and 1. Derivative of temperature dependent intensity at 730 nm (Figure S17); mean emission intensity (orange and red) and conductance at 393 K between 0.5 vol % and 20 vol % O_2 (Table S6); as measured and normalized conductance at 393 K between 0.5 vol % and 20 vol % O_2 (Figure S18); as measured and normalized intensity at 393 K between 0.5 vol % and 20 vol % O_2 (Figure S19); mean emission intensity (orange and red) at 393 K between 250 and 2000 ppm of O_2 (Table S7); as measured and normalized intensity at 393 K between 250 and 2000 ppm of O_2 (Figure S20) (PDF)

AUTHOR INFORMATION

Corresponding Author

Michael Tiemann − *Paderborn University, Faculty of Science, Department of Chemistry, D-33098 Paderborn, Germany;* orcid.org/0000-0003-1711-2722; Email: michael.tiemann@upb.de

Authors

Linda Kothe − *Paderborn University, Faculty of Science, Department of Chemistry, D-33098 Paderborn, Germany; Woehler Technik GmbH, D-33181 Bad Wuennenberg, Germany*

Marvin Kloß − *Paderborn University, Faculty of Science, Department of Chemistry, D-33098 Paderborn, Germany*

Tobias Wagner − *Paderborn University, Faculty of Science, Department of Chemistry, D-33098 Paderborn, Germany*

Marc Wengenroth − *Woehler Technik GmbH, D-33181 Bad Wuennenberg, Germany*

Michael Poeplau − *Woehler Technik GmbH, D-33181 Bad Wuennenberg, Germany*

Stephan Ester − *Woehler Technik GmbH, D-33181 Bad Wuennenberg, Germany*

Complete contact information is available at: https://pubs.acs.org/10.1021/acs.jpcc.5c01678

Author Contributions

L.K., M.T. and M.P. conceived the project. M.W. constructed the temperature regulation. S.E. contributed to the critical scientific discussions about the measurements and the temperature fitting. M.K. and T.W. performed the X-ray diffraction measurements. The manuscript was written by L.K. with contributions of all authors. All authors discussed the results and have approved the final version of the manuscript.

Notes

The authors declare no competing financial interest.

ACKNOWLEDGMENTS

We thank Nadine Buitkamp for help with SEM and EDX. We would like to thank Prof. Cedrik Meier for the valuable discussions.

REFERENCES

(1) Hodgkinson, J.; Tatam, R. P. Optical gas sensing: a review. *Meas. Sci. Technol.* **2013**, *24*, 012004.

(2) Amrehn, S.; Wu, X.; Wagner, T. Tungsten Oxide Photonic Crystals as Optical Transducer for Gas Sensing. *ACS Sens.* **2018**, *3*, 191−199.

(3) Tawade, P.; Mastrangeli, M. Integrated Electrochemical and Optical Biosensing in Organs-on-Chip. *ChemBioChem* **2024**, *25*, No. e202300560.

https://doi.org/10.1021/acs.jpcc.5c01678
J. Phys. Chem. C 2025, 129, 9239−9245

(4) Tanumihardja, E.; Olthuis, W.; Van den Berg, A. Ruthenium Oxide Nanorods as Potentiometric pH Sensor for Organs-On-Chip Purposes. *Sensors* **2018**, *18* (9), 2901.
(5) Xu, Y.; Zhou, X.; Sorensen, O. T. Oxygen sensors based on semiconducting metal oxides: an overview. *Sens. Actuators, B* **2000**, *65*, 2−4.
(6) Jin, J.; Huang, Y.; Zhang, C.; Zhang, L.; Jiang, S.; Chen, X. Novel Lead Halide Perovskite and Copper Iodide Materials for Fluorescence Sensing of Oxygen. *Biosensors* **2025**, *15* (3), 132.
(7) Fioravanti, A.; Marani, P.; Morandi, S.; Giordano, L.; Maddalena, P.; Carotta, M. C.; Lettieri, S. Optical Sensing of Molecular Oxygen (O_2) via Metal Oxide Photoluminescence: A Comparative Study of TiO_2, SnO_2 and ZnO. *Chemosensors* **2021**, *9* (7), 163.
(8) Kiisk, V.; Puust, L.; Mändar, H.; Ritslaid, P.; Rähn, M.; Bite, I.; Jankovica, D.; Sildos, I.; Jaaniso, R. Phase stability and oxygen-sensitive photoluminescence of ZrO_2:Eu,Nb nanopowders. *Mater. Chem. Phys.* **2018**, *214*, 135−142.
(9) Tiemann, M. Porous Metal Oxides as Gas Sensors. *Chem. Eur. J.* **2007**, *13*, 8376−8388.
(10) Poeplau, M.; Ester, S.; Henning, B.; Wagner, T. Recombination mechanisms of luminescence type gas sensors. *Phys. Chem. Chem. Phys.* **2020**, *22*, 19948.
(11) Seo, J.; Yoo, H. Zinc-Tin Oxide Film as an Earth-Abundant Material and Its Versatile Applications to Electronic and Energy Materials. *Membranes* **2022**, *12*, 485.
(12) Hashemi, T.; Al-Allak, H. M.; Illingsworth, J.; Brinkman, A. W.; Woods, J. Sintering behaviour of zinc stannate. *J. Mater. Sci. Lett.* **1990**, *9*, 776−778.
(13) Fang, J.; Huang, A.; Zhu, P.; Xu, N.; Xie, J.; Chi, J.; Feng, S.; Xu, R.; Wu, M. Hydrothermal preparation and characterization of Zn_2SnO_4 particles. *Mater. Res. Bull.* **2001**, *36*, 1391−1397.
(14) Baruah, S.; Dutta, J. Zinc stannate nanostructures: hydrothermal synthesis. *Sci. Technol. Adv. Mater.* **2011**, *12*, 013004.
(15) Tsai, M.-T.; Chang, Y.-S.; Liu, Y.-C. Photocatalysis and luminescence properties of zinc stannate oxides. *Ceram. Int.* **2017**, *43*, S428−S434.
(16) Fernandes, C.; Santa, A.; Santos, A.; Bahubalindruni, P.; Deuermeier, J.; Martins, R.; Fortunato, E.; Barquinha, P. A Sustainable Approach to Flexible Electronics with Zinc-Tin Oxide Thin-Film Transistors. *Adv. Electron. Mater.* **2018**, *4*, 1800032.
(17) Kim, J. S.; Jang, Y.; Kang, S.; Lee, Y.; Kim, K.; Kim, W.; Lee, W.; Hwang, C. S. Substrate-Dependent Growth Behavior of Atomic-Layer-Deposited Zinc Oxide and Zinc Tin Oxide Thin Films for Thin-Film Transistor Applications. *J. Phys. Chem. C* **2020**, *124* (49), 26780−26792.
(18) Rovisco, A.; Branquinho, R.; Deuermeier, J.; Freire, T.; Fortunato, E.; Martins, R.; Barquinha, P. Shape Effect of Zinc-Tin Oxide Nanostructures on Photodegradation of Methylene Blue and Rhodamine B under UV and Visible Light. *ACS Appl. Nano Mater.* **2021**, *4* (2), 1149−1161.
(19) Lou, X.; Jia, X.; Xu, J.; Liu, S.; Gao, Q. Hydrothermal synthesis, characterization and photocatalytic properties of Zn_2SnO_4 nanocrystal. *Mater. Sci. Eng., A* **2006**, *432*, 221−225.
(20) Kim, B.; Park, J.; Geier, M. L.; Hersam, M. C.; Dodabalapur, A. Voltage-Controlled Ring Oscillators Based on Inkjet Printed Carbon Nanotubes and Zinc Tin Oxide. *ACS Appl. Mater. Interfaces* **2015**, *7*, 12009−12014.
(21) Miyauchi, M.; Liu, Z.; Zhao, Z.-G.; Anandan, S.; Hara, K. Single crystalline zinc stannate nanoparticles for efficient photoelectrochemical devices. *Chem. Commun.* **2010**, *46*, 1529−1531.
(22) Wang, Y.-F.; Li, K.-N.; Xu, Y.-F.; Rao, H.-S.; Su, C.-Y.; Kuang, D.-B. Hydrothermal fabrication of hierarchically macroporous Zn_2SnO_4 for highly efficient dye-sensitized solar cells. *Nanoscale* **2013**, *5*, 5940.
(23) Chen, Z.; Cao, M.; Hu, C. Novel Zn_2SnO_4 Hierarchical Nanostructures and Their Gas Sensing Properties toward Ethanol. *J. Phys. Chem. C* **2011**, *115*, 5522−5529.
(24) Sivapunniyam, A.; Wiromrat, N.; Myint, M. T. Z.; Dutta, J. High-performance liquefied petroleum gas sensing based on nanostructures of zinc oxide and zinc stannate. *Sens. Actuators, B* **2011**, *157*, 232−239.
(25) Ma, G.; Zou, R.; Jiang, L.; Zhang, Z.; Xue, Y.; Yu, L.; Song, G.; Li, W.; Hu, J. Phase-controlled synthesis and gas-sensing properties of zinc stannate ($ZnSnO_3$ and Zn_2SnO_4) faceted solid and hollow microcrystals. *CrystEngComm* **2012**, *14*, 2172.
(26) Hu, Q. R.; Jiang, P.; Zhang, Y.; Wang, S. L.; Jia, X.; Tang, W. H. Synthesis and photoluminescence of Zn_2SnO_4 nanowires. *J. Alloys Compd.* **2009**, *484*, 25−27.
(27) Wang, L.; Zhang, X.; Liao, X.; Yang, W. A simple method to synthesize single-crystalline Zn_2SnO_4 (ZTO) nanowires and their photoluminescence properties. *Nanotechnology* **2005**, *16*, 2928.
(28) Zhao, J.-W.; Qin, L.-R.; Zhang, L.-D. Single-crystalline Zn_2SnO_4 hexangular microprisms: Fabrication, characterization and optical properties. *Solid State Commun.* **2007**, *141*, 663−666.
(29) Reshchikov, M. A. Mechanisms of Thermal Quenching of Defect-Related Luminescence in Semiconductors. *Phys. Status Solidi A* **2021**, *218*, 2000101.
(30) Schön, M. Zum Leuchtmechanismus der Kristallphosphore. *Z. Phys.* **1942**, *119*, 463−471.
(31) Klasens, H. A. Transfer of Energy Between Centres in Zinc Sulphide Phosphors. *Nature* **1946**, *158*, 306−307.
(32) Ibach, H.; Lüth, H. *Solid-State Physics*; Springer: New York, 2009; pp 144ff−426ff..
(33) Zhang, Z.; Yates, J. T. Band Bending in Semiconductors: Chemical and Physical Consequences at Surfaces and Interfaces. *Chem. Rev.* **2012**, *112*, 5520−5551.
(34) Myndrul, V.; Coy, E.; Bechelany, M.; Iatsunskyi, I. Photoluminescence label-free immunosensor for the detection of Aflatoxin B1 using polyacrylonitrile/zinc oxide nanofibers. *Mater. Sci. Eng., C* **2021**, *118*, 111401.
(35) Kothe, L.; Klippstein, J.; Kloß, M.; Wengenroth, M.; Poeplau, M.; Ester, S.; Tiemann, M. Oxygen-Dependent Photoluminescence and ElectricalConductance of Zinc Tin Oxide (ZTO): A Modified Stern-Volmer Description. *ChemPhysChem* **2025**, *26*, No. e202400984.
(36) Wijesinghe, U.; Longo, G.; Hutter, O. S. Defect engineering in antimony selenide thin film solar cells. *Energy Adv.* **2023**, *2*, 12−33.
(37) Dou, J.; Shen, D.; Li, Y.; Abate, A.; Wei, M. Highly Efficient Perovskite Solar Cells Based on a Zn_2SnO_4 Compact Layer. *ACS Appl. Mater. Interfaces* **2019**, *11* (40), 36553−36559.
(38) Lee, S.; Kim, S.; Shin, S.; Jin, Z.; Min, Y.-S. Band structure of amorphous zinc tin oxide thin films deposited by atomic layer deposition. *J. Ind. Eng. Chem.* **2018**, *58*, 328−333.
(39) Fang, H.-H.; Adjokatse, S.; Shao, S.; Even, J.; Loi, M. A. Long-lived hot-carrier light emission and large blue shift in formamidinium tin triiodide perovskites. *Nat. Commun.* **2018**, *9*, 243.
(40) Koziej, D.; Barsan, N.; Weimar, U.; Szuber, J.; Shimanoe, K.; Yamazoe, N. Water-oxygen interplay on tin dioxide surface: Implication on gas sensing. *Chem. Phys. Lett.* **2005**, *410*, 321−323.
(41) Wang, C.; Yin, L.; Zhang, L.; Xiang, D.; Gao, R. Metal Oxide Gas Sensors: Sensitivity and Influencing Factors. *Sensors* **2010**, *10* (3), 2088−2106.

https://doi.org/10.1021/acs.jpcc.5c01678
J. Phys. Chem. C 2025, 129, 9239−9245

Supporting Information

Temperature Studies of Zinc Tin Oxide Photoluminescence for Optical O_2 Sensing

Linda Kothe[a,b], Marvin Kloß[a], Tobias Wagner[a], Marc Wengenroth[b], Michael Poeplau[b], Stephan Ester[b], Michael Tiemann[a]*

[a]Paderborn University, Faculty of Science, Department of Chemistry, Warburger Str. 100, D-33098 Paderborn, Germany

[b]Woehler Technik GmbH, Woehler-Platz 1, D-33181 Bad Wuennenberg, Germany

Powder X-ray Diffraction

This work focuses on the photoluminescence of zinc tin oxide (ZTO). As displayed in figure S1, Zn_2SnO_4 was obtained without crystalline residual, which suggests a phase-pure product.

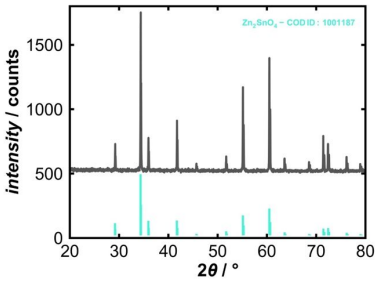

Figure S1. x-ray diffraction pattern with COD (crystallographic open database) ID reference 1001187 for Zn_2SnO_4.[1]

The most intense powder XRD reflection (311) at 34.39° was fitted with a linear combination of two gaussian functions, figure S2 and equation S1, to determine the center and full width at half maximum. The reflexes at 55.13° and 60.49° were fitted as well to determine the average crystallite size.

$$g(x) = A\frac{1}{\sigma\sqrt{2\pi}}exp\left(-\frac{1}{2}\left(\frac{x-\mu}{\sigma}\right)^2\right) \quad \text{(S1)}$$

S2

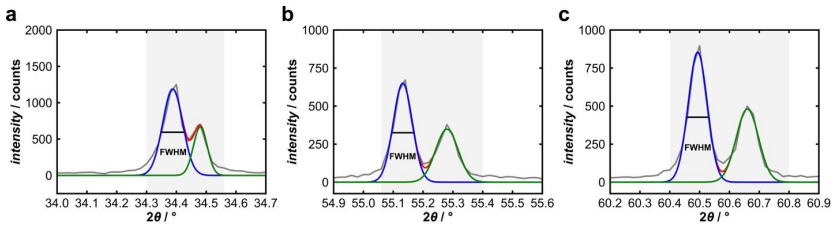

Figure S2. magnification of x-ray diffraction pattern of **a** (311) reflex at 34.39°, **b** (511) reflex at 55.13° and **c** (440) reflex at 60.49°, all fitted with a double gaussian function.

Based on the Scherrer equation, equation S2, the average crystallite size was determined with the reflex positions and FWHM obtained from the fits, table S1.[2] The wavelength λ is 0.15406 nm, the shape factor *K* was the 0.94 (general value by Scherrer).

$$L = \frac{K \cdot \lambda}{\Delta(2\theta) \cdot \cos(\theta_0)} \tag{S2}$$

Table S1. Reflex parameters and crystallite sizes.

hkl	2θ / °	FWHM / °	shape factor	L / nm	average / nm
311	34.39	0.079	0.94	109.9	120.8 ± 7.8
511	55.13	0.075		124.6	
440	60.49	0.075		127.7	

This is consistent with scanning electron microscopy (SEM) images, figure S3a, as there are either smaller and bigger crystallites. Zn and Sn are homogeneously distributed in the sample, figure S3b

S3

and c. Due to the different weights of Zn and Sn the resulting penetrations depths of x-rays, the topography of the particles is apparent in the energy dispersive x-ray spectroscopy (EDX) data.

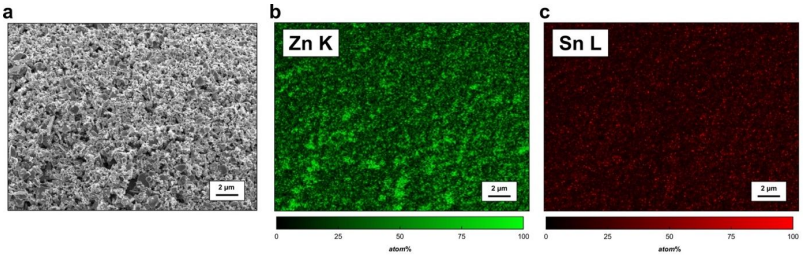

Figure S3. a SEM image 500 x magnification, **b** EDX mapping of Zn (green) and **c** Sn (red) in atom% 500 x magnification.

UV/Vis Data

UV/VIS measurements were executed at room temperature under ambient conditions. The transmittance, Figure S4a, was converted to reflectance *R* and the function of reflectance *F(R)*, equation S3. The function of reflectance was plotted according to the Tauc plot to check for a direct, Figure S4b, or indirect, Figure S4c, band gap. The absorption α of semiconducting materials is described with equation S4, which can be linearized, equation S5. α_0 is a fitting parameter, *E* the energy of the radiation in eV and E_U the Urbach energy. From the slope of the linearization the Urbach energy E_U can be determined, Figure S4d.[3-5]

$$F(R) = \frac{(1-R)^2}{2R} \quad \text{(S3)}$$

$$\alpha = \alpha_0 \cdot \exp\left\{\frac{E}{E_U}\right\} \quad \text{(S4)}$$

$$\ln(F(R)) = \frac{E}{E_U} + c \tag{S5}$$

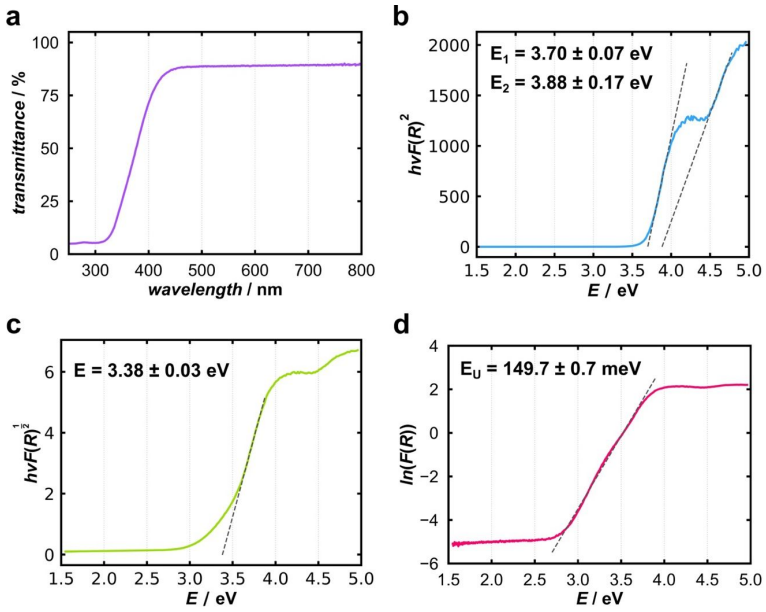

Figure S4. a transmittance **b** Tauc plot for γ = ½ (direct band gap) **c** Tauc plot for γ = 2 (indirect band gap) **d** determination of the Urbach energy E_U for ZTO.

The coexistence of two direct band gaps may be related to the Sn content in the inverse cubic spinel. In the literature it is indicated that Zn_2SnO_4 seems to be phase pure, though the Sn concentration can range between 26 at% and ca. 40 at%.[6] Though the PXRD does not indicate an additional phase, there might be domains with varying Sn content in the lattice, which would not be revealed. With increasing Sn content, the band gap is slightly increased.[7] During UV/Vis measurements a

much larger sample area (larger measurement spot) is evaluated, which could explain the additional direct band gap in the Tauc Plot.

Photoluminescence Data

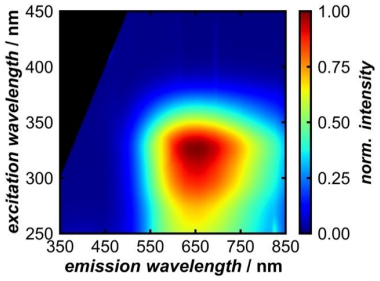

Figure S5. excitation-emission spectrum of ZTO.

Measurement Setup

The ZTO particles were either drop-coated on a ceramic substrate with a gold interdigital structure to measure the conductance and photoluminescence (PL) simultaneously or on a quartz glass substrate, which was placed in a cuvette insert. The cuvette insert was designed for a commercially available quartz glass cuvette, Figure S6a. A type-K thermocouple measures the temperature below a ceramic heating element. The measured temperature is received by a flue gas analyzer (Woehler A450). The ceramic heater is connected to an Agilent E3640A power supply, which was controlling the substrate temperature by a Python script. The gas atmosphere was controlled with a gas mixing

system (Woehler GM450) and applied with a flow rate of 150 mL/min or 300 mL/min. This setup was used in the JASCO Fluorometer or in combination with a custom-built setup and the ceramic substrate, Figure S6b to measure photoluminescence and conductance simultaneously. The measurement setup is housed in an aluminum body to shield external light. With a Voltcraft LSP-1403 power supply, operated at 15 V, a Roithner DUV325-HL46N LED (λ=325 nm) was used as a light source to excite the sample. The emission is collected with a collimator lens and transferred by optical fibers to an Ocean Optics Flame Miniature spectrometer. The interdigital electrode structure is operated in series with a 1 MOhm resistor on a Voltcraft LSP-1403 power supply with a constant output voltage of 20 V. The conductance of the ZTO particles is calculated using the measured voltage (multimeter, HP 34401A) via the interdigital structure.

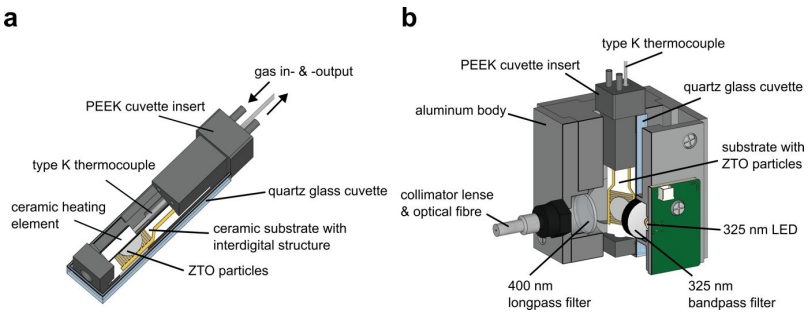

Figure S6. Sectional drawings of **a** the cuvette insert and **b** experimental setup to measure photoluminescence and conductance simultaneously at controlled temperatures and gas atmospheres.

Temperature-dependent emission spectra

For the measurement setup either a ceramic substrate with a gold interdigital structure or a quartz glass substrate can be used. When excited with 325 nm, Figure S7, the ceramic substrate shows a weak emission in the red range, whereas the quartz glass substrate shows an even weaker emission in the blue range. After drop coating of the sample on the substrate the emission spectrum of the sample overshadows the residual emissions of the substrates at low temperatures (313 K or lower), Figure S8a. With increasing temperature and decreasing emission intensity of the sample the emission of the ceramic substrate alters the spectrum significantly, Figure S8b. For the measurements with the JASCO fluorometer, the samples were drop-coated onto a quartz glass substrate.

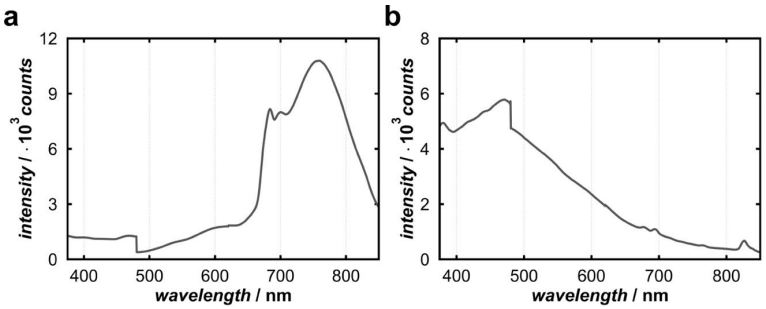

Figure S7. emission spectra of **a** empty ceramic substrate and **b** empty quartz glass substrate, both excited with 325 nm, measured at room temperature, no active gas flow.

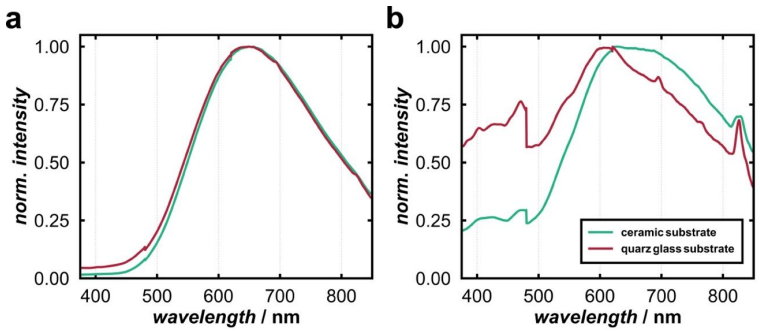

Figure S8. emission spectra of ZTO particles **a** at 313 K on ceramic substrate (green line) and quartz glass substrate (red line) and **b** at 433 K on ceramic substrate (green line) and quartz glass substrate (red line), all excited with 325 nm, 300 ml/min pure N_2.

The following emission spectra were measured in a pure N_2 (0 vol% O_2) or 20 vol%O_2 in N2 (20 vol% O_2) with a gas flow of 300 ml/min, Figure S9. The samples were tempered to 433 K and kept at this temperature and the respective atmosphere for 1 h. Then the temperature was decreased about 20 K and kept for 30 min before emission spectra and lifetime were recorded.

S9

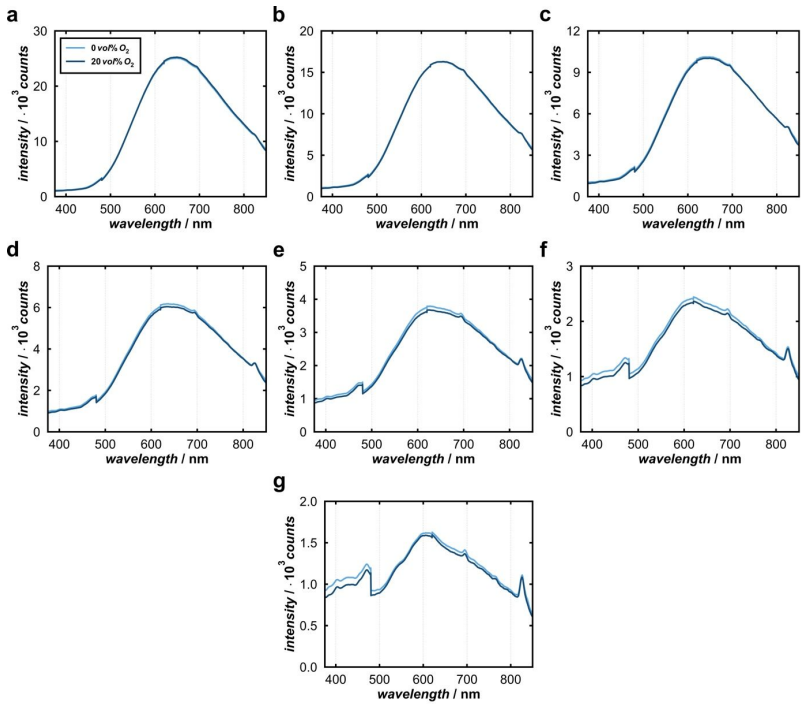

Figure S9. emission spectrum of ZTO particles at **a** 313 K, **b** 333 K, **c** 353 K, **d** 373 K, **e** 393 K, **f** 413 K and **g** 433 K in pure N_2 (0 vol% O_2, light blue) and 20 vol% O_2 in N_2 (dark blue) atmosphere, 300 ml/min.

The obtained emission spectra are all dependent of the wavelength. For further evaluation the spectra are converted to an energy scale. The possible options are evaluated in figure S10. The simple conversion with equation S6 from wavelength to energy (in eV) results in an altered spectrum, figure S10 a and b. E is the energy, h Planck's constant, c the speed of light and λ the wavelength.

$$E = \frac{hc}{\lambda} \quad \text{(S6)}$$

In the literature a *Jacobian Conversion* is recommended. Here it is assumed that the intensity of the wavelength and energy are equal due to energy conservation, equation S7. f(E) is the function of energy and f(λ) the function of wavelength.[8]

$$f(E)\,dE = f(\lambda)\,d\lambda \quad \text{(S7)}$$

As wavelength and energy are not equidistant on scale the intensity measured (I(λ)) need to be converted to an intensity in dependence of the energy I(E), equation S8. The multiplication of I(λ) with $\frac{hc}{E^2}$ results in the spectrum depicted in figure S10c.[8]

$$I(E) = I(\lambda)\frac{d\lambda}{dE} = I(\lambda)\frac{d}{dE}\left(\frac{hc}{E}\right) = -I(\lambda)\frac{hc}{E^2} \quad \text{(S8)}$$

After this transformation the peak maximum is significantly red shifted and its shape still differs from the original form. Instead by a conversion of I(λ) to I(1/E), equation S9, the energy conservation is maintained, equation S10. The spectrum is now plotted against the reciprocal energy, figure S10d.[9]

$$I(1/E) = I(\lambda)hc \quad \text{(S9)}$$

$$\lambda_{max} = hc\left(\frac{1}{E_{max}}\right) \quad \text{(S10)}$$

S11

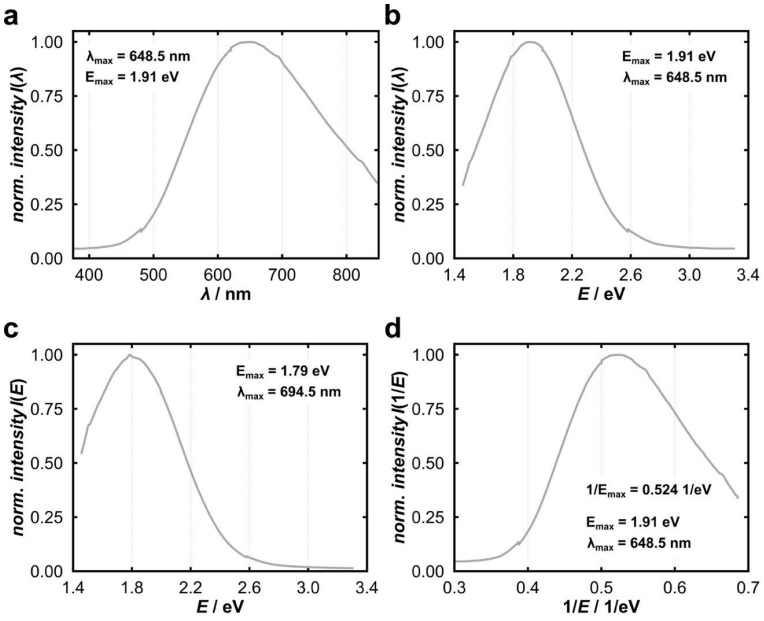

Figure S10. emission spectra of ZTO particles in **a** (I(λ)) vs. wavelength, **b** (I(λ)) vs. energy, **c** (I(E)) vs. energy and **d** (I(1/E)) vs. reciprocal energy. Measured at 313 K, excited with 325 nm, 300 ml/min pure N_2.

For the fit with the double Gaussian function, only the spectra in pure N_2 were considered, as the O_2-induced intensity change was hardly measured, and the expected spectral change was expected to be in same order as the error due to fitting. The fit range is between 0.389 1/eV and 0.65 1/eV. From each fit the amplitude A, peak center $1/E_{center}$, peak width σ and area is obtained. The fit optimization was executed with the scipy.optimize function in Python, which is based on a non-linear least squares optimization to fit the data.

S12

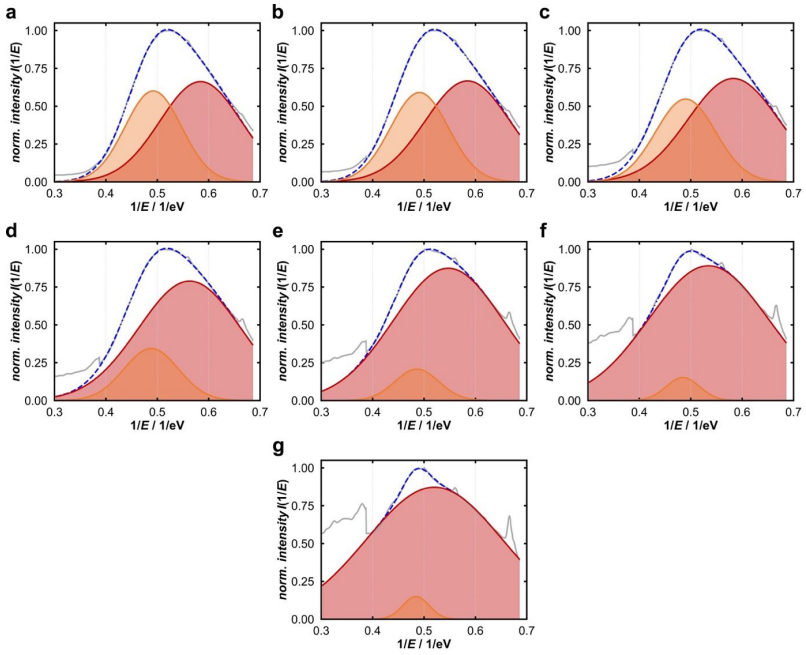

Figure S11. emission spectrum of ZTO particles at **a** 313 K, **b** 333 K, **c** 353 K, **d** 373 K, **e** 393 K, **f** 413 K and **g** 433 K fitted with a double Gaussian function (dashed blue line).

Table S2. Fit parameters of ZTO emission, 1. Gauss function (orange function).

temperature / K	**A**	**1/E$_{center}$ / 1/eV**	**σ / 1/eV**	**area**	**fit range**
313	0.083 ± 0.014	0.492 ± 0.002	0.055 ± 0.002	0.08	0.389-0.65 1/eV
333	0.084 ± 0.013	0.491 ± 0.001	0.057 ± 0.001	0.08	
353	0.080 ± 0.008	0.490 ± 0.000	0.058 ± 0.001	0.08	

373	0.046 ± 0.002	0.488 ± 0.000	0.053 ± 0.001	0.05	
393	0.022 ± 0.001	0.486 ± 0.000	0.043 ± 0.001	0.02	
413	0.012 ± 0.000	0.485 ± 0.000	0.033 ± 0.000	0.01	
433	0.010 ± 0.000	0.484 ± 0.000	0.026 ± 0.000	0.01	

Table S3. Fit parameters of ZTO emission, 2. Gauss function (red function).

temperature / K	**A**	**$1/E_{center}$ / 1/eV**	**σ / 1/eV**	**area**	**fit range**
313	0.131 ± 0.015	0.584 ± 0.009	0.079 ± 0.005	0.12	0.389-0.65 1/eV
333	0.137 ± 0.013	0.585 ± 0.007	0.082 ± 0.004	0.12	
353	0.151 ± 0.008	0.583 ± 0.005	0.088 ± 0.002	0.13	
373	0.197 ± 0.002	0.563 ± 0.001	0.099 ± 0.000	0.17	
393	0.234 ± 0.001	0.547 ± 0.000	0.107 ± 0.000	0.21	
413	0.259 ± 0.000	0.535 ± 0.000	0.116 ± 0.000	0.23	
433	0.288 ± 0.001	0.520 ± 0.000	0.132 ± 0.000	0.24	

Life Time Measurements

The lifetime was determined at the maxima of the E_{center} positions obtained from the fits. The reciprocal energy was converted to wavelength. Every measurement ("phosphorescence lifetime", λ_{ex} = 325 nm, excitation bandwidth = 5 nm, emission bandwidth = 20 nm, 50 ms chopping period) was executed 10 times in total at each emission wavelength. Each measurement was an average of 100 scans. So, every lifetime is an average value of 1000 measurements. To determine the lifetime,

the time required for the intensity to fall to 1/e is identified, Figure S12. As the emission intensity change in the presence of O_2 is very low, also the lifetime is hardly affected by it, Figure S13. The lifetime was also determined at room temperature (298 K), 303 K and 308 K. Though there is a significant change in lifetime at room temperature, already at 303 K no significant change was measured. This might hint, that either the intensity changes are too small to affect the lifetimes reliably or the changes in lifetime are in a different order. The measurement parameters and lifetimes are summarized in Tables S4 and S5.

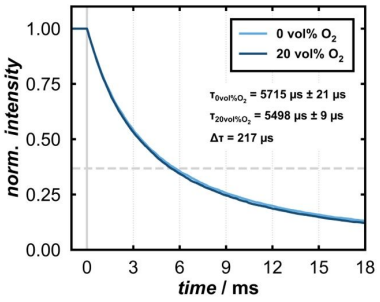

Figure S12. lifetimes of λ_{center} = 614 nm measured in pure N_2 (0 vol% O_2, light blue) and 20 vol% O_2 in N_2 (dark blue) at 298 K. The excitation wavelength is 325 nm.

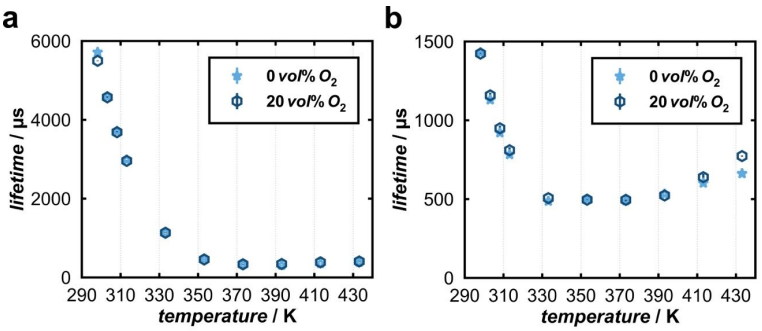

Figure S13. lifetimes of **a** orange and **b** red emission, measured at the respective peak positions between 298 K and 433 K, measured in pure N_2 (0 vol% O_2, light blue) and 20 vol% O_2 in N_2 (dark blue). For all data the excitation wavelength is 325 nm.

Table S4. Peak position in wavelength, lifetime in pure N_2 and 20 vol% O_2 in N_2 atmosphere of orange emission.

temperature / K	**λ_{em} / nm**	**$\tau_{0vol\%}$ / µs**	**$\tau_{20vol\%}$ / µs**
298	614	5715 ± 21	5498 ± 9
303	614	4588 ± 14	4571 ± 26
308	613	3710 ± 21	3686 ± 24
313	610	2984 ± 7	2959 ± 10
333	609	1132 ± 9	1134 ± 11
353	608	464 ± 18	456 ± 1
373	605	331 ± 11	334 ± 10
393	603	312 ± 14	341 ± 3
413	601	355 ± 8	384 ± 2

433	601	389 ± 14	406 ± 5

Table S5. Peak position in wavelength, lifetime in pure N_2 and 20 vol% O_2 in N_2 atmosphere of red emission.

temperature / K	**λ_{em} / nm**	**$\tau_{0vol\%}$ / µs**	**$\tau_{20vol\%}$ / µs**
298	728	1429 ± 6	1423 ± 5
303	728	1130 ± 11	1158 ± 17
308	724	921 ± 9	949 ± 17
313	724	783 ± 17	810 ± 18
333	725	487 ± 6	506 ± 10
353	723	499 ± 18	496 ± 2
373	698	490 ± 13	495 ± 9
393	679	532 ± 3	523 ± 4
413	663	602 ± 7	639 ± 21
433	645	662 ± 7	773 ± 4

Data Evaluation

For each emission spectrum the spectrometer integrates over 30 seconds. To evaluate the data, spectra are smoothed with a moving average of 20 measurement points. The spectral resolution is 0.473 nm. The emission spectrum of ZTO particles is displayed in figure S14. To evaluate the

quencher impact, the intensity at 606 nm (vertical orange line) and 730 nm (vertical red line) is determined for every spectrum and tracked over time.

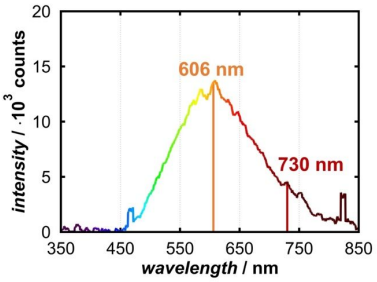

Figure S14. emission spectrum of ZTO particles at 298 K, 606 nm and 730 nm highlighted with vertical lines, excited with 325 nm.

Measurement Modes

For the intensity fitting with equation 1 the O_2 concentration was kept constant (pure N_2 or 20 vol% O_2 in N_2) and the temperature was varied according to the sequence in Figure 15a. The temperature sequence starts with a 433 K segment for 2 h, followed by a temperature decrease to 313 K in 10 K steps. Each temperature is kept constant for 30 min. Finally, an additional segment at 433 K is applied for 15 min. For the variation of the O_2 concentration the temperature was kept constant at 393 K and the gas atmosphere was varied according to Figure S15b and S15c. In both cases, 250 ppm-2000 ppm or 0.5 vol%-20 vol%, the sample was kept in a pure N_2 atmosphere for 4 h, before the respective O_2 concentration was kept constant for 1 h, followed by a 1 h regeneration segment in pure N_2.

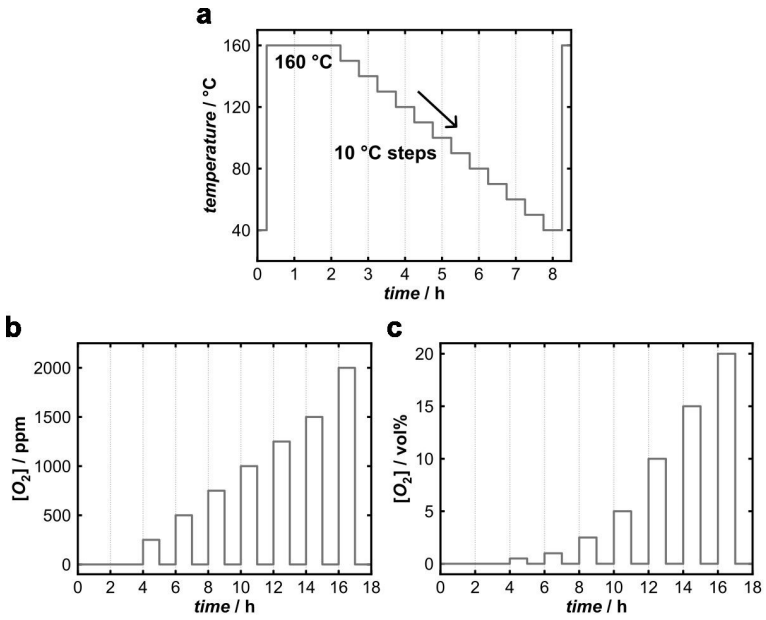

Figure S15. a temperature profile under constant O_2 concentration, **b** concentration profile between 250 ppm and 2000 ppm O_2 in N_2 at constant temperatures and **c** concentration profile between 0.5 vol% and 20 vol% O_2 in N_2 at constant temperatures.

The fit optimization was executed with the scipy.optimize function in Python, which is based on a non-linear least squares optimization to fit the data.

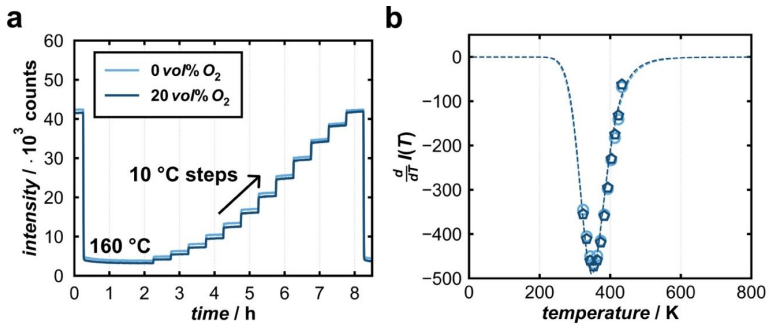

Figure S16. ***a*** ZTO emission intensity at 606 nm between 313 K and 433 K, **b** 1. deviation of equation 1, equation S6, at 606 nm. In pure N_2 (0 vol% O_2, light blue) and 20 vol% O_2 in N_2 (dark blue), excited with 325 nm.

$$\frac{d}{dT}I(T) = -\frac{I(T=0K)\cdot C\cdot E_A\cdot exp\left\{\frac{E_A}{k_BT}\right\}}{k_B\cdot T^2\cdot\left(C+exp\left\{\frac{E_A}{k_BT}\right\}\right)\cdot\left(C+exp\left\{\frac{E_A}{k_BT}\right\}\right)} \quad \text{(S11)}$$

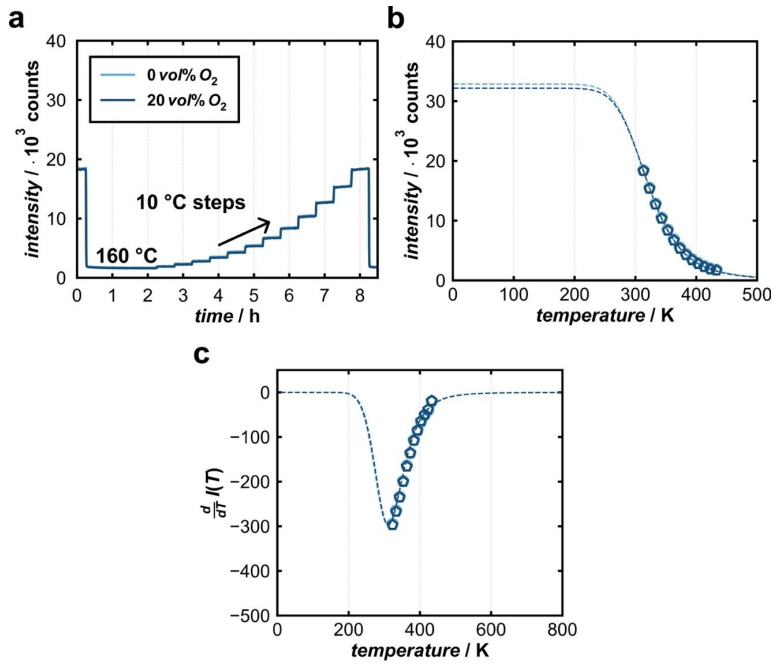

Figure S17. a ZTO emission intensity at 730 nm between 313 K and 433 K, **b** ZTO emission intensity at 730 nm, fitted with equation 1 and **c** 1. derivative of equation 1, equation S6, at 730 nm. In pure N_2 (0 vol% O_2, light blue) and 20 vol% O_2 in N_2 (dark blue), excited with 325 nm.

S21

Conductance & Photoluminescence Measurements

Table S6. Mean emission intensity of orange and red emission and maximum conductance at 393 K.

intensity / counts	606 nm	10826
	730 nm	3651
conductance / nS		223.1

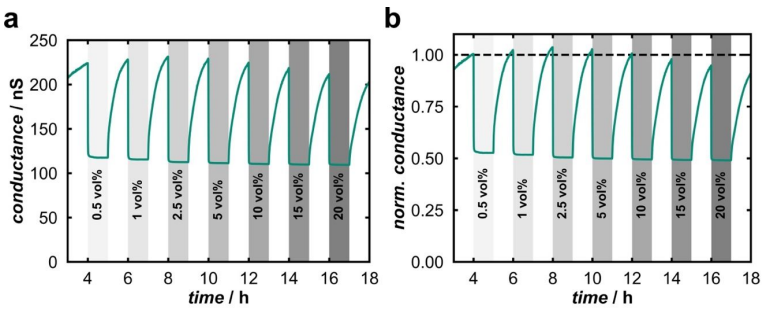

Figure S18. O_2 dependent (0.5 vol%-20 vol%) conductance of ZTO at 393 K **a** as measured, **b** normalized. 150 mL/min, excited with 325 nm.

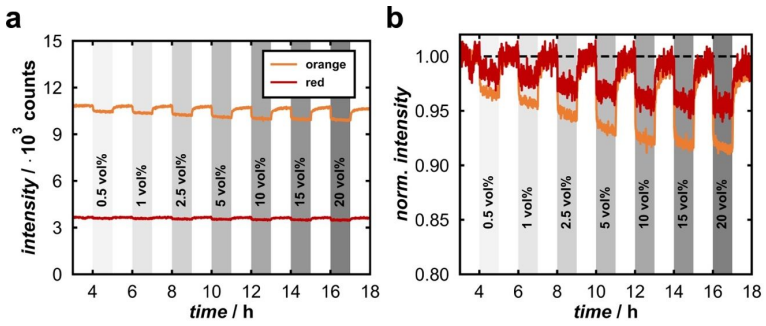

Figure S19. O_2 dependent (0.5 vol%-20 vol%) photoluminescence of ZTO at 120 ° **a** as measured, **b** normalized. 150 mL/min, excited with 325 nm.

Table S7. Mean emission intensity of orange and red emission at 393 K.

intensity / counts	606 nm	10604
	730 nm	3580

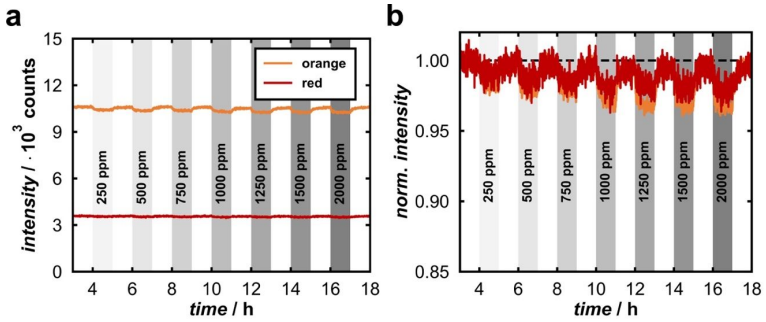

Figure S20. O_2 dependent (250 ppm-2000 ppm) photoluminescence of ZTO at 393 K **a** as measured, **b** normalized. 150 mL/min, excited with 325 nm.

References

1 Choisnet, J.; Deschanvres, A.; Raveau, B. Substitution du zinc par le cadmium dans le spinelle Zn_2SnO_4. Etude de la repartition des cations dans la solution solide $Zn_{2-2x}Cd_{2x}SnO_4$, *C. R. Acad. Sci. Paris C* **1968**, 266, p. 543-545.

2 Scherrer, P. Bestimmung der Größe und der inneren Struktur von Kolloidteilchen mittels Röntgenstrahlen, *Göttinger Nachrichten Math. Phys.* **1918**, 2, 98–100

3 Makula, P.; Pacia, M.; Macyk, W. How To Correctly Determine the Band Gap Energy of Modified Semiconductor Photocatalysts Based on UV–Vis Spectra, *J. Phys. Chem. Lett.* **2018**, 9, 23, 6814-6817. DOI: 10.1021/acs.jpclett.8b02892

4 Ugur, E.; Ledinsky, M.; Allen, T. G.; Holovsky, J.; Vlk, A.; De Wolf, S. Life on the Urbach Edge, *J. Phys. Chem. Lett.* **2022**, 13, 33, 7702-7711. DOI: 10.1021/acs.jpclett.2c01812

5 Kumar, A.; Kumar, R.; Verma, N.; Anupama, A. V.; Choudhary, H. K.; Philip, R.; Sahoo, B. Effect of the band gap and the defect states present within band gap on the non-linear optical absorption behaviour of yttrium aluminium iron garnets, *Optical Materials* **2020**, 108, 110163. DOI: 10.1016/j.optmat.2020.110163

6 Kim, W.; Kang, S.; Lee, Y.; Mun, S.; Choi, J.; Lee, S.; Hwang, C. S. Electrical properties of amorphous Zn–Sn–O thin films depending on composition and post-deposition annealing temperature near crystallization temperature, *J. Mater. Chem. C* **2023**, 11, 8254-8262. DOI: 10.1039/D2TC05090K

S24

7 Teng, J.; Chen, Y.; Huang, C.; Yang, M.; Zhu, B.; Liu, W.-J.; Ding, S.-J.; Wu, X. Graded-Band-Gap Zinc–Tin Oxide Thin-Film Transistors with a Vertically Stacked Structure for Wavelength-Selective Photodetection, *ACS Appl. Mater. Interfaces* **2024**, 16, 7, 9060-9067. DOI: 10.1021/acsami.3c18737

8 Mooney, J.; Kambhampati, P. Get the Basics Right: Jacobian Conversion of Wavelength and Energy Scales for Quantitative Analysis of Emission Spectra, *J. Phys. Chem. Lett.* **2013**, 4, 3316-3318. DOI: 10.1021/jz502066v

9 Marín, E; Calderón, A. Conversion of Wavelength and Energy Scales and the Analysis of Optical Emission Spectra, *J. Phys. Chem. Lett.* **2022**, 13, 8376-8379. DOI: 10.1021/acs.jpclett.2c02621

4 Tin(IV) Oxide as Electron Transporting Layer

The electron transporting layer (ETL) represents one of the five layers that form the structure of a perovskite solar cell (PSC). Each layer is inherently significant and must be optimized. In the present work, the PSCs were designed as follows:

- FTO or ITO coated glass substrate (anode)
- ETL: SnO_2
- perovskite layer: $FAPbBr_3$/$MAPbBr_3$ (2D-perovskite passivation)
- HTL: Spiro-MeOTAD (chemically oxidized)
- Au (cathode)

SnO_2 is among the most frequently selected ETL materials. The established syntheses of this layer often contain harsh, toxic chemicals, require a prolonged reaction time (several hours), and an additional temperature treatment. The development of a non-toxic, rapid synthesis not only reduces chemical waste and supplied energy, but also simplifies the procedure and promotes the technology's attractiveness for industrial production. The objective of this study was to synthesize a SnO_2 ETL in a time frame of less than 10 min. The efficiency of the resulting solar cell should be comparable to that based on established ETL methods.

The SnO_2 synthesis described herein was a chemical bath deposition (CBD) based on the thermal decomposition of sodium stannate ($Na_2SnO_3{\cdot}3H_2O$). In solution, the hexahydroxostannate ion ($[Sn(OH)_6^{2-}]$) was formed and able to condensate with ions of the same species or surface hydroxy groups of the substrate. The obtained powders were characterized with X-ray powder diffraction (PXRD) and scanning electron microscopy (SEM). The films that were received were characterized by SEM, transmission electron microscopy (TEM) and energy electron loss spectroscopy (EELS). The homogeneous growth in solution resulted in the formation of spherical particles with a diameter of *ca.* 50 nm. The heterogeneous growth occurring on the surface was substrate-dependent. In this study, fluorine-doped tin oxide (FTO) and indium tin oxide (ITO)-coated glass substrates were selected.

The SnO_2 deposition on FTO was successful and the primary synthesis optimization was executed with these substrates. Due to the simplicity of the coating, optimization of the reaction temperature, educt concentration, and growth time was necessary. It was demonstrated that the optimal PSC efficiency was achieved after an ETL growth time of 6 min when the reaction temperature and concentration were set. A direct comparison of conventionally prepared PSCs and this approach produced devices of equivalent efficiency. A high solar cell efficiency is indicative of suppressed charge carrier recombination at the ETL and perovskite interface.

ITO facilitated successful SnO_2 deposition, yielding PSCs that demonstrated high efficiency as well. However, under identical reaction conditions, the device's optimal efficiency was attained after 16 min of reaction time. Consequently, additional synthesis optimization is necessary.

M. J. Grotevent, L. Kothe, Y. Lu, C. Krajewska, M.-C. Shih, S. Tan, M. Tiemann, M. G. Bawendi, *Non-Toxic and Rapid Chemical Bath Deposition for SnO_2 Electron Transporting Layers in Perovskite Solar Cells*, Chemistry of Materials **2025**, submitted.

Participation in this Publication

The manuscript was written by M.J.G. and L.K. as first authors, with contributions from all authors. M.J.G. and M.G.B. conceived the project. L.K. fabricated the tin oxide films with scientific contributions of M.T. M.J.G. fabricated solar cells from the SnO_2 coated substrates and performed electrical characterization of the devices. Y.L. recorded the scanning electron microscopy images. C.K. performed the X-ray diffraction measurements. M.-C.S. and S.T. contributed to the critical scientific discussions about the perovskite composition and decomposition pathways.

Non-toxic and rapid chemical bath deposition for SnO_2 electron transporting layers in perovskite solar cells

Matthias J. Grotevent,[1,‡] Linda Kothe,[1,2,‡] Yongli Lu,[1] Chantalle Krajewska,[1] Meng-Chen Shih,[1] Shaun Tan,[1] Michael Tiemann[2], Moungi G. Bawendi[1*]

[1]Department of Chemistry, Massachusetts Institute of Technology, 77 Massachusetts Avenue, Cambridge, Massachusetts 02139, USA

[2]Paderborn University, Faculty of Science, Department of Chemistry, Warburger Str. 100, D-33098 Paderborn, Germany

E-mail: mgb@mit.edu

[‡]Both authors contributed equally to this work

[*]corresponding author

KEYWORDS: perovskite solar cell, chemical bath deposition, tin oxide, amorphous, metal oxide

Abstract. Perovskite solar cells are a promising new solar technology with efficiencies surpassing polycrystalline silicon solar cell technology. For the n-i-p perovskite solar cells, tin oxide is typically used as the electron transport layer. One typical deposition method is chemical bath deposition. However, the drawbacks are toxic precursors and the slow reaction driven by dissolved oxygen forming SnO_{2-x}. Here, we present a tin oxide chemical bath deposition starting from non-toxic sodium stannate solutions. Within 6 minutes of reaction time, a 9 nm thick amorphous

Sn(IV)-oxide film is grown yielding solar cells with power conversion efficiencies of at least 23.2%. Surprisingly, the sole use of Sn(IV) precursors contradicts the previous assumption on Sn(II) required for *n*-doping & high electric conductivity, and, unexpectedly, amorphous tin oxide films are as suitable for charge transport layers as their crystalline counterparts. The synthesis method is transferrable to other substrates (ITO, glass) and other thin-film metal oxide coatings (MoO_x, SiO_2), and beneficial for devices such as solar cells, photodetectors, light emitting diodes, and heterogeneous catalysis.

Introduction

Perovskite solar cells are one of the most promising emerging solar technologies, with power conversion efficiencies surpassing 26%.[1] Typically, perovskite solar cells are fabricated in *pin* or *nip* device architectures, indicating the relative doping of their constituent layers. The current advantages of *pin* perovskite solar cells are thermal device stability and power conversion efficiency, however, a commercial product will further require mechanical stability and price competitivity in comparison to established solar technologies. Furthermore, technological advancements and novel materials discovery are not predictable, and it is not foreseeable which technology, *nip* or *pin,* both or none, will have a successful market entry in the intermediate future. Therefore, it is advisable to continue research on both technologies, *pin* and *nip*. The latter device architecture commonly uses tin(IV) oxide (SnO_2) as the electron transport layer (ETL) due to its high photostability, ideal energy band alignment, efficient hole blocking & electron conducting property, low defect density, and low-temperature processability in comparison to TiO_2.[2] SnO_2 can be deposited using evaporation or from solution, for example, by thermal evaporation, sputtering, sol-gel, atomic layer deposition, or chemical bath deposition. The deposition methods are well summarized in a review article and citations therein.[3] Chemical bath deposition is particularly

interesting due to its ability to produce uniform, compact, and pinhole-free thin films. In a typical reaction, a water-based Sn(II)-chloride solution combined with hydrochloric acid, thioglycolic acid, and urea reacts over about 12 hours, forming a nonstoichiometric SnO_{2-x} layer.[2,4–6] Recent adaptions of this synthesis replaced thioglycolic acid with oxalic acid.[7] This removes sulfur-containing precursors, which may potentially lead to contaminations and reduced device stability, and the reaction time was shortened down to 3 hours.[7] Others have replaced the Sn(II)-chloride and hydrochloric acid with Sn(II)-sulfate precursors, enabling the chemical bath deposition on chemically sensitive substrates such as indium-tin-oxide (which is chemically etched under hydrochloric acid conditions). However, the reaction times are still multiple hours.[8] In all of the aforementioned chemical bath depositions, urea decomposes and increases the pH value. At the same time, Sn(II) is oxidized to Sn(IV) from dissolved molecular oxygen. Therefore, two reactions are simultaneously changing the reaction conditions and products. The changes in the reaction conditions at an increased pH value result in a slightly nonstoichiometric SnO_{2-x}.[2,9] This continuous oxidation state change is believed to be desired for gradual doping within the SnO_2 layer, enabling excellent charge transfer.[2] However, dissolved oxygen, critical for the oxidation of Sn(II) to Sn(IV), must be present and is usually not accounted for. Quantifying the dissolved oxygen is cumbersome and dynamic due to the exposure of the reaction to the ambient atmosphere and subsequent oxygen diffusion from the atmosphere into the solution. Notably, industrial applications require a fast and highly reproducible layer deposition with synthesis times below 15 minutes—a highly challenging task. Additional steps, such as post-synthesis annealing at 170 °C for 60 minutes in air, are typically performed, but long annealing times are also problematic for commercial processing. The annealing step is usually required to reduce the surface defect density and remove unwanted organic contaminations originating from precursors.[2,7]

Besides the direct growth of SnO_2 on substrates by chemical bath deposition, SnO_2 nanoparticles can be synthesized, for example, from tin(II) halides such as $SnCl_2$,[10,11] SnF_2,[12] and $SnCl_4$.[13] Furthermore; a few reports grow SnO_2 from tin(IV) stannates, e.g., the growth of SnO_2 shells on Au nanoparticles by thermal decomposition of the stannate at 60 °C over one hour,[14] or the synthesis of spherical SnO_2 nanoparticles of about 30 nm size by thermal decomposition of sodium stannate over 5 hours at 150 °C (pressurized water).[15] While those reactions take hours, their final deposition from solution can be faster, for example, by slot-die coating and blade coating; however, thicker coatings are required for nanoparticle films to ensure a pinhole-free and conformal layer.

Here, we present a rapid (within 6 minutes), simple chemical bath deposition of SnO_2 from non-toxic Sn (IV) stannate in water. No additional chemicals such as binders and stabilizers are required. The reaction is simply based on the thermal decomposition of the stannate. Solar cell power conversion efficiencies of at least 23.2% are demonstrated on par with the fabricated reference devices. In addition to the fabrication on fluorine-doped tin-oxide substrates, the mild reaction conditions enable the chemical bath deposition of SnO_2 on chemically sensitive substrates such as indium tin oxide. In addition, post-synthesis thermal annealing is not required, further simplifying device fabrication. This method is not limited to the deposition of tin oxide; it can also be applied to other water-soluble oxometallates to form thin films, such as molybdenum (VI) oxide and silicon dioxide.

Results and Discussion

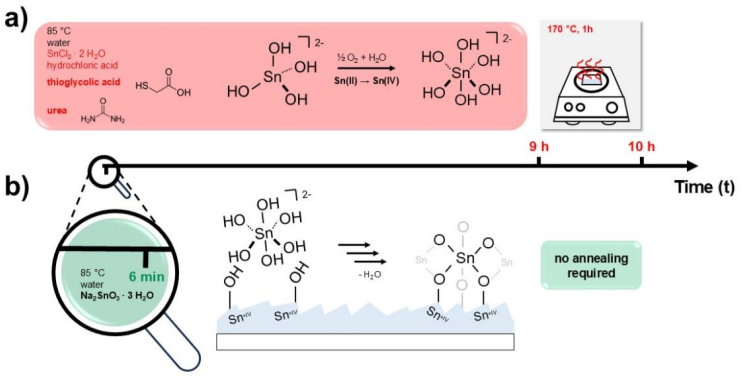

Figure 1. Schematic comparison *of the SnO_2 chemical bath deposition from a) previous reports using Sn(II) chloride and b) this work using sodium stannate (Sn(IV)).*

Figure 1a displays the reaction components for a typical chemical bath deposition. The reaction is based on a complex mechanism with various side reactions and uncontrolled Sn(II) oxidation to Sn(IV) over a few hours. A novel and simple chemical bath deposition (Figure 1b) is investigated using low-cost water-soluble stannate precursors such as sodium stannate ($Na_2SnO_3 \cdot 3H_2O$). The precursor is readily solubilized in deionized water, resulting in a clear colorless solution, with a pH value of 12 (0.1M) and the hexahydroxostannate as the dominating tin species. [16,17] While hexahydroxostannate solutions are meta-stable for weeks at room temperature, the solution slowly becomes hazy indicating a condensation reaction towards SnO_2. The chemical reaction can be described with the following equation with slight modification from Ref ([16]):

$$Na_2SnO_3 \cdot\ 3\,H_2O\ \equiv\ Na_2[Sn(OH)_6] \leftrightharpoons\ SnO_2 \downarrow\ +\ 2\,NaOH + 2\,H_2O$$

The equation indicates a pH change, which is also experimentally observed; sodium stannate solutions are already basic with a pH of 12 at room temperature and a slight increase in the pH value towards 12.4 after the chemical bath deposition reaction. The homogeneous nucleation from sodium stannate in solution is based on the condensation from two octahedral coordinated stannate complexes $[Sn(OH)_6]^{2-}$.[15,17] Surface hydroxy-groups from FTO (fluorine-doped tin (IV) oxide) substrates may well serve as nucleation centers facilitating a competing templated heterogeneous film growth.

One central aspect of our synthesis is the non-toxicity of this reaction compared to the established process: thioglycolic acid is toxic if swallowed, inhaled, or in contact with skin. Hydrochloric acid is corrosive regarding metals and can cause severe skin or eye damage. Sn(II)chloride dihydrate and sodium stannate can cause some harm to aquatic life and are caustic chemicals. In addition, Sn(II)chloride possesses some oral and inhalation toxicity. The lower toxicity of our reaction educts leads to a safer work environment and reduced waste disposal costs.

The perovskite solar cell efficiency is dependent on the SnO_2 thickness, whereas the thickness can be controlled with the reaction temperature, educt concentration, and growth time. The film growth was stopped in previous reports once the homogeneous particle growth led to a murky dispersion.[2] This qualitative estimation of the reaction end point is precise enough for very long reaction times over multiple hours but has a large error bar at short reaction times; however, it is a reasonably good starting point. As a first optimization step, the growth time was investigated for one stannate concentration at different bath temperatures between 55 °C and 85 °C with reaction times of 45 minutes down to 6 minutes, respectively (Figure 2a). The corresponding solar cells exhibited similar power conversion efficiencies (Figure 2a-inset, Supplementary Figure 1, SEM images in Supplementary Figure 2a). Even higher temperatures may lead to the outgassing

of dissolved air, resulting in gas bubbles adhered to the FTO surface, hindering the SnO2 growth locally, which is detrimental to shorter reaction times as the gas bubbles remain adhered throughout the complete reaction. Given the similarity of the power conversion efficiency with temperature and as fast reaction times are desired, the reaction bath temperature for further optimization was fixed at a temperature of 85 °C. As a second optimization step, the precursor concentration was investigated as a function of the reaction time (Figure 2b) at a fixed temperature of 85 °C, with reaction times between 20 and 5.5 minutes. 0.1 mol/L was chosen as an optimized sodium stannate concentration as the reaction time is similar to the 0.2 mol/L concentration but uses a smaller amount of the educt. The solar cell efficiencies of the corresponding solar cells are comparable to each other and lie within the estimated error bar (Figure 2b-inset, Supplementary Figure 3, SEM in SI Figure 2b). The third optimization step replaces the qualitative reaction endpoint estimation (murkiness of the suspension) with a quantitative measure of the actual reaction time independently of the murkiness of the suspension. The stannate concentration (0.1M) and bath temperature (85 °C) were fixed, the solar cell efficiency increased up to a reaction time of 6 minutes, and the observed hysteresis narrowed down simultaneously (Figure 2c, Supplementary Figure 4). Scanning electron microscopy images of the coated and one uncoated FTO substrate (as reference) are shown in Figure 2d. The fully optimized reaction conditions using our fast and green deposition process resulted in device efficiencies on par with devices fabricated with the previous chemical bath deposition process.

The film growth can be described following two distinct film growth mechanisms discussed in the literature: an ion-by-ion growth directly on the substrate and a homogeneous nanoparticle growth with subsequent nanocrystal attachment to the substrate.[3,7,9,13] A combination of both growth mechanisms would also be plausible, and individual growth mechanisms may be

specific to any underlying growth conditions (e.g., the presence of additives in solution).[9] The scanning electron microscopy images in Figure 2d strongly indicate an ion-by-ion growth: the films were grown in the same growth solution and taken out one after another at different reaction times; simultaneously, nanoparticles formed within the solution. Therefore, a nanoparticle formation in solution and subsequent attachment to the film should lead to drastic changes in the film smoothness of two subsequent films. The smoothness of the films for all growth times strongly indicates an ion-by-ion growth mechanism, while some attached nanoparticles can be observed for one sample. Those particles may have been attached by chance to the film during the removal of the substrate from the growth solution. While this study optimized the chemical bath deposition of SnO_2 from sodium stannate, other water-soluble stannate sources, such as potassium stannate, can also be used (Supplementary Figure 5). Furthermore, the reaction is not limited to stannates; other water-soluble oxometallates, such as sodium molybdate and sodium metasilicate, can be used as precursors forming coatings of molybdenum(VI) oxide and silicon(IV) oxide, respectively (Supplementary Figure 6).

Note that the perovskite and hole-transport layers were deposited by spin coating in dry air instead of a nitrogen atmosphere (humidity <1%). Processing in dry air is beneficial for industrial scalability but may have resulted in slightly lower device efficiencies.

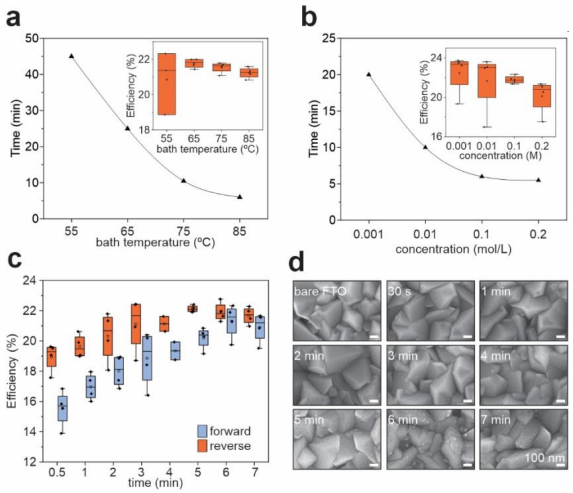

Figure 2. SnO_2 chemical bath deposition under various reaction conditions on fluorine-doped tin oxide (FTO) substrates. *Reaction time as measured by observation of murkiness as a function of a) reaction bath temperature (0.1M stannate concentration) – inset shows the corresponding device power conversion efficiency, b) $Na_2SnO_3 \cdot 3H_2O$ concentration (bath temp.: 85 °C) – inset shows the corresponding device power conversion efficiency; c) solar cell efficiency as a function of reaction time (fixed and independent of the observation of murkiness) (bath temp.: 85 °C, 0.1M concentration), and d) scanning electron microscopy images of the SnO_2/FTO substrates at respective growth times.*

Figure 3 compares the chemical bath depositions from $SnCl_2$ with the reaction from sodium stannate solutions. Scanning electron microscopy images (Figure 3a, b) reveal that both reactions produce densely compact films with continuous coverage. The morphology exhibits a rougher surface for films grown with Sn(II)-chloride, which may indicate a difference in the deposition process for both routes. The coordination of Sn(II)-ions by additives (functioning as ligands) such as urea and thioglycolic acid (or oxalic acid) may lead to particle growth in solution with subsequent adhesion to the FTO surface.[18] In addition, the coordination of molecules on the particle surface may lead to a preferential growth direction and a rougher, nanostructured surface.

This surface roughness could negatively affect conductivity and device performance;[19] however, the solar cell efficiencies from the respective films (Figure 3c) lead to the exact same device efficiencies. This surprises, as the established synthesis route from Sn(II) precursors is believed to require the formation of impurity doping (SnO_{2-x}), resulting in a *n*-type semiconductor for improved electrical conductivity. In comparison, the water-based stannate synthesis route starts from Sn(IV), and any significant Sn(II) doping seems unlikely due to the lack of reduction agents and the presence of dissolved molecular oxygen (oxidizing agent) in the solution. This is further supported by the fact that stoichiometric SnO_2 is a white powder, and SnO_{2-x} appears as a yellow powder.[10,11,15,20] The white color of the nanoparticles formed in solution from the stannate reaction indicates the absence of any significant Sn(II) doping. Therefore, the role of Sn(II) in the bulk of SnO_2 thin films remains a topic of discussion. The nonstoichiometric SnO_{2-x} surface, however, is unfavorable and presents additional charge trap states that potentially facilitate degradation of the adjacent perovskite layer.[7] Therefore, the Sn(II) chloride route requires a post-synthesis oxidation step by annealing the substrates for one hour at 170 °C, converting surface Sn(II) to Sn(IV).[7] This prolongs the overall fabrication by another hour, which is unsuitable for scale-up and industrial use. On the contrary, the sodium stannate synthesis route leads to surface Sn(IV) and does not require any post-synthesis annealing step: no efficiency difference has been observed between annealed and non-annealed substrates (Figure 3d). This highlights the advantages of the sodium stannate chemical bath deposition by starting from Sn(IV): (I) fast SnO_2 film growth within minutes (no oxidation step required), (II) surface oxidation by annealing is not required, (III) no toxic chemicals and additives are used.

The direct, in-depth analysis of the thin SnO_2 on fluorine-doped SnO_2 (FTO) substrates is highly challenging due to the low spatial dimensionality of the SnO_2 film and the similarity of the

film and growth substrate. A cross-sectional high-angle annular dark-field scanning transmission electron microscopy image (Figure 3e) shows a 9 nm thick amorphous SnO_2 layer grown on top of a FTO substrate. The amorphous character is further supported with powder x-ray diffraction measurements from solution-grown SnO_2 nanoparticles (scanning electron microscopy image, Supplementary Figure 7), which do not show any significant diffraction peaks, indicating the growth of a primarily amorphous SnO_2 film (Supplementary Figure 8). In addition, a fast growth rate at low temperatures is usually associated with forming amorphous materials. In contrast, crystalline materials typically require slow growth and high temperatures to incorporate atoms perfectly into an organized crystal lattice. Electron energy loss spectroscopy (Figure 3f) was used further to analyze the oxidation state of the tin oxide layer. Typically, the tin oxidation state is indirectly investigated by looking at the energy-loss near-edge structure of the oxygen K-edge with an energy splitting of about 3.5 eV for Sn(II)-oxide and about 6 eV for Sn(IV)-oxide.[7,21] While the energy splitting is rather 6 eV (indicating Sn(IV) oxide), the height ratio of the two oxygen peaks is smaller and closer to the reference of the Sn(II) oxide spectrum. However, the literature reference spectra analyzed crystalline samples, and the amorphous character of our tin oxide layer may result in deviations from the literature spectra due to differences in the local chemical environment. Amorphous SnO_2 is likely nonstoichiometric, with hydroxy-groups incorporated into the film to fully coordinate the oxophilic Sn(IV). While trace amounts of Sn(II) cannot entirely be ruled out—even though unlikely due to the oxidative reaction conditions—it is surprising that amorphous Sn(IV)-oxide electron transport layers perform as well as representative crystalline films.

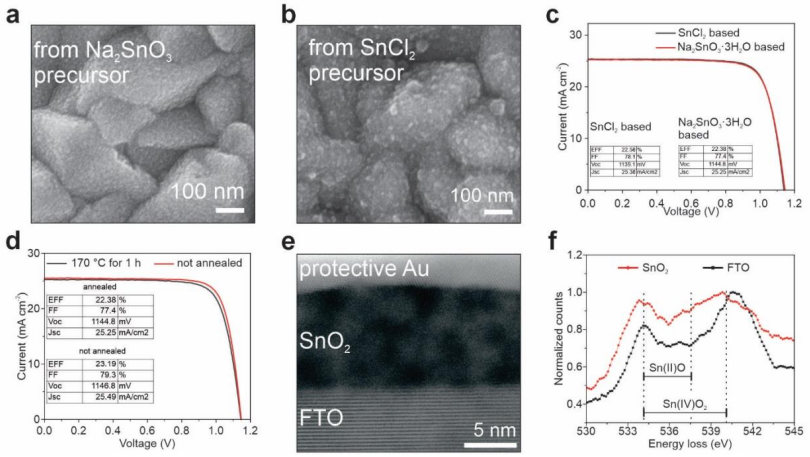

Figure 3. Analysis of SnO_2 grown from chemical bath deposition. *Scanning electron microscopy images from a) $Na_2SnO_3 \cdot 3H_2O$ precursor, b) from $SnCl_2$ precursor, c) solar cell device efficiency fabricated from SnO_2 grown with $SnCl_2$ or $Na_2SnO_3 \cdot 3H_2O$ precursors, d) solar cell device efficiency of a thermally annealed and non-annealed SnO_2 film, e) high-angle annular dark-field scanning transmission electron microscopy image of SnO_2 grown from stannate solutions on FTO, and f) electron energy loss spectroscopy of the respective films in (e).*

The stability of the thermal device was investigated under maximum power point tracking, 1-sun, and in a nitrogen atmosphere (Supplementary Figure 9). In general, solar cell stability is restricted by its least stable layer or least stable interface. We find that the perovskite solar cell degradation is currently dominated by the perovskite and 2D-perovskite passivation layer decomposition which may lead to a reaction and degradation of the hole transport layer as well.[22] Both perovskite solar cells (Supplementary Figure 9) were fabricated with SnO_2 electron transport layers following the sodium stannate chemical bath deposition reaction. However, the high-efficiency perovskite layer which includes methylammonium, chloride, and bromide ions as well as a 2D-perovskite layer fabricated with *n*-hexylammonium bromide results in a fast degradation. The perovskite solar cell with cesium in the perovskite layer and poly(methyl methacrylate) as a

thin passivation layer,[23–25] resulted in device stability exceeding 1250 hours with negligible degradation at a lower power conversion efficiency. If the dominant device degradation originates from the SnO_2 layer, we would expect a similar degradation behavior for both solar cells—which we do not observe. The presence of sodium ions remaining on the surface of the SnO_2 originating from the educt cannot be confirmed or ruled out. However, the tin oxide surface is washed multiple times with deionized water and treated with a potassium chloride solution prior to the perovskite film deposition. Any presence of sodium ions can potentially passivate defects and enhance the solar cell efficiency,[26–28] however, no noticeable effect is observed in comparison to devices fabricated from Sn(II) chloride precursors in the absence of sodium-containing precursors. The perovskite and the interface passivation require further investigation and optimization, which is beyond the scope of this investigation.

The basic reaction conditions of the chemical bath deposition from sodium stannate enable SnO_2 coatings on indium-tin-oxide (ITO) substrates, which would otherwise be chemically etched under prevalent acidic reaction conditions. The electron microscopy images in Figure 4a show pristine ITO and ITO coated with a continuous and homogeneous SnO_2 coating. Like the growth on FTO substrates, an ion-by-ion growth is initially observed within the first 10 minutes of growth. A higher degree of surface-attached nanoparticles can be observed for longer growth times. Compared to the coating on FTO, ITO substrates require a longer reaction time, with perovskite solar cell devices achieving a power conversion efficiency of at least 20% (Figure 4b, 4c, Supplementary Figure 10). Like the SnO_2 coatings on FTO, the hysteresis is reduced at longer SnO_2 growth times. The demonstrated chemical bath deposition from sodium stannate is not restricted to FTO and ITO substrates; other hydroxy-terminated substrates, such as glass, can also be coated, as we observed a visible SnO_2 film on the surface of glass slides (SiO_x). The

demonstrated scalable SnO_2 thin film deposition method may be used, e.g., for solar cells, photodetectors, light emitting devices, and heterogeneous catalysis.

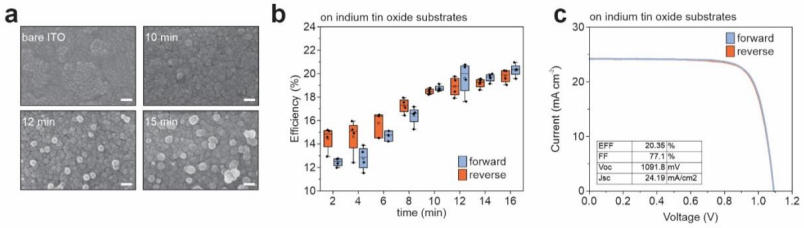

Figure 4. SnO_2 CBD from $Na_2SnO_3 \cdot 3H_2O$ precursor on indium tin oxide (ITO) substrates. *a) scanning electron microscopy images at various growth times, b) solar cell efficiency as a function of growth time, and c) current-voltage measurement. Scale bars 100 nm.*

Conclusion

A tin oxide chemical bath deposition starting from Sn(IV) stannate instead of the typical Sn(II)-chloride synthesis route is presented. The Sn(IV) stannate synthesis cuts the reaction time from hours to 6 minutes, does not require any post-synthesis annealing step, uses only non-toxic precursors, and enables the synthesis on chemically labile substrates such as indium-tin-oxide. The device efficiency of perovskite solar cells fabricated from those substrates is on par with reference solar cells with at least a 23.2% power conversion efficiency. The fast synthesis produces a mostly amorphous film of about 9 nm thickness. Previous understandings of tin oxide-based electron transport layers required a Sn(IV) surface for a low density of charge carrier trap states but sufficient *n*-doping of SnO_2 by Sn(II) for improved electrical conductivity in the bulk. The presented results contradict the current opinion as solely Sn(IV) precursors have been used in water under oxidative reaction conditions—preventing the formation of Sn(II). It also highlights that charge transport layers of amorphous metal oxide films can be as good as their crystalline

counterparts. Overall, the presented progress enables the chemical bath deposition of tin oxide to be used for commercial application. Besides tin oxide, the presented method is transferable to other metal-oxide thin films, such as molybdenum(VI) oxide and silicon(IV) oxide, grown from water-soluble oxometallates.

Experimental Section

Chemicals: Sodium stannate trihydrate (95%, Sigma Aldrich), potassium stannate trihydrate (99.9% trace metal basis, Sigma Aldrich), sodium molybdate dihydrate (≥99%, Sigma Aldrich), sodium metasilicate (Sigma Aldrich), thioglycolic acid (≥99%, Sigma Aldrich), hydrochloric acid (37 wt.% in H_2O, 99.999% trace metals basis, Sigma Aldrich), urea (≥99.5%, Sigma Aldrich), tin(II) chloride dihydrate (≥99.995% trace metals basis, Sigma Aldrich), Acetone (≥99.5%, semiconductor grade, thermo scientific), 2-propanol (≥99.5%, semiconductor grade, thermo scientific), Hellmanex III (Hellma Analytics), potassium chloride (>99%, Sigma ALdrich), 2-methoxyethanol (99.8%, anhydrous, Sigma Aldrich), lead(II) iodide (99.999% trace metals basis, perovskite grade, Sigma Aldrich), formamidinium iodide (>99.99%, Greatcellsolar), methylammonium bromide (>99.99%, Greatcellsolar), lead(II) bromide (99.999%, trace metals basis, Sigma Aldrich), methylammonium chloride (>99.99%, Greatcellsolar), *N,N*-dimethylformamide (99.8%, anhydrous, Sigma Aldrich), dimethyl sulfoxide (≥99.9%, anhydrous, Sigma Aldrich), diethyl ether (≥99.7 %, anhydrous, contains 1ppm BHT as inhibitor, Sigma Aldrich), *n*-hexylammonium bromide (>99 %, Greatcellsolar), cesium iodide (99.999% trace metal basis, Aldrich), poly(methyl methacrylate) (M_w 120k, Aldrich), chloroform (≥99%, anhydrous, contains amylenes as stabilizers, Sigma Aldrich), bis(trifluoromethane)sulfonimide (≥95.0 %, Sigma Aldrich), hydrogen peroxide$_{(aq)}$ (≥30%, Sigma Aldrich), Spiro-MeOTAD (>99,8%, Luminescence Technology), chlorobenzene (99.8%, anhydrous, Sigma Aldrich), hexane

(95%, anhydrous, Sigma Aldrich), Gold (Kurt J Lesker). All chemicals were used as received without further purification.

Synthesis of Spiro-MeOTAD(TFSI)$_4$ and Spiro-MeOTAD(TFSI)$_x$

Caution: bis(trifluoromethane)sulfonimide (HTFSI) is a toxic super acid.

Synthesis as described elsewhere.[22] Briefly, Bis(trifluoromethane)sulfonimide (HTFSI, 2 g, 7 mmol) was solved in 2 mL H_2O and 2 mL (20 mmol) 30% H_2O_2. 10 mL of Spiro-MeOTAD in chlorobenzene (0.5 mg/mL, 0.4 µmol/mL) was added and a biphasic mixture was received. The mixture was stirred at room temperature for 36 h. 7 mL of the organic solution was taken, and 40 mL hexane was added and centrifuged at 7000 rpm for 5 min. The precipitated Spiro(TFSI)$_4$ was dried with a heat gun for 3 min in ambient air.

For the hole transporting layer, typically, 5-10% of Spiro-MeOTAD was oxidized by mixing the above-obtained Spiro-MeOTAD(TFSI)$_4$ with 1.75 mL of Spiro-MeOTAD in chlorobenzene (70 mg/mL, 57 µmol/mL) and filtering the solution through a 0.22 µm polytetrafluoroethylene syringe filter.

Synthesis of methylammonium lead tribromide ($MAPbBr_3$)

Under nitrogen atmosphere, MABr (methylammonium bromide, 1.5252 g, 13.62 mmol) 10 mL *N,N*-dimethyl formamide were combined at room temperature. Pb(II)Br_2 (5 g, 13.62 mmol) was added. As the salts were dissolved completely, the solution was filtered (0.22 µm polytetrafluoroethylene syringe filter) and heated to 90 °C (stirring at 300 rpm). Crystals appeared in the first few minutes. The solution was stirred for about one hour. The crystals were gained by filtration, washed three times with diethyl ether, and transferred into a nitrogen glovebox.

Device fabrication

Substrate cleaning: In a Hellendahl staining vessel, 1 mL Hellmanex III and 49 mL deionized water were mixed, and substrates were submerged in the liquid. The substrates were ultrasonicated for 10 min at room temperature, following an ultrasonication sequence of solvents (deionized water, deionized water, acetone, 2-propanol) for 10 min each at 50 °C. The substrates were dried with a nitrogen gas gun.

SnO_2 deposition by chemical bath deposition:

Sodium Stannate trihydrate based: Substrates were placed in a Hellendahl staining vessel with 45 mL deionized water and tempered at the respective temperatures (55 °C, 65 °C, 75 °C, or 85 °C) for 20 min. A respective amount (16 mg, 160 mg, 1600 mg, or 3200 mg) of $Na_2SnO_3 \cdot 3\ H_2O$ was dissolved in 5 mL deionized water and added to the tempered vessel, no aging of the solution is required. The 3200mg $Na_2SnO_3 \cdot 3\ H_2O$ were dissolved in 10mL deionized water and added to 40mL deionized water in the tempered vessel. Substrates were removed once the solutions turned murky or the desired reaction time was reached. The substrates were cleaned by ultrasonication with a sequence of solvents (deionized water, deionized water, acetone, 2-propanol) for 10 minutes each at 50 °C. The substrates were dried with a nitrogen gas gun.

A typical synthesis uses 1600 mg (6 mmol) $Na_2SnO_3 \cdot 3\ H_2O$ dissolved in 5 mL deionized water and added to 45 mL deionized, tempered water at 85 °C. The reaction is stopped after 6 minutes by removing the substrates from the growth solution.

Tin(II) chloride based: In a Hellendahl staining vessel, urea (625 mg, 10.4 mmol), $Sn(II)Cl_2 \cdot 2H_2O$ (138 mg, 0.6 mmol), thioglycolic acid (12.5 µL, 0.1 mmol), hydrochloric acid (37 %; 625 µL, 7.5 mmol) and 50 mL deionized water are mixed. Substrates were placed in the vessel, which was kept

at 65 °C for about 12-14 h. The reaction was complete once the solution turned murky. The substrates were cleaned by ultrasonication with a sequence of solvents (deionized water, deionized water, acetone, 2-propanol) for 10 minutes each at 50 °C. The substrates were dried with a nitrogen gas gun.

MoO_x chemical bath deposition: 1 g (4.1 mmol) $Na_2MoO_4 \cdot 2\ H_2O$ was dissolved in 5 mL deionized water and added to 45 mL deionized, tempered water at a temperature of 85 °C in a Hellendahl staining vessel with FTO-coated substrates immersed in the solution. The reaction is stopped after 20 or 150 minutes by removing the substrates from the growth solution. The substrates were cleaned by ultrasonication with a sequence of solvents (deionized water, deionized water, acetone, 2-propanol) for 10 minutes each at 50 °C. The substrates were dried with a nitrogen gas gun.

SiO_2 chemical bath deposition: 1 g (8.2 mmol) Na_2SiO_3 was dissolved in 5 mL deionized water and added to 45 mL deionized, tempered water at a temperature of 85 °C in a Hellendahl staining vessel with FTO-coated substrates immersed in the solution. The reaction is stopped after 20 or 150 minutes by removing the substrates from the growth solution. The substrates were cleaned by ultrasonication with a sequence of solvents (deionized water, deionized water, acetone, 2-propanol) for 10 minutes each at 50 °C. The substrates were dried with a nitrogen gas gun.

Potassium chloride deposition: For some experiments, some substrates were annealed in an ambient atmosphere for one hour at 170 °C. Other substrates were not annealed. All samples were treated with oxygen plasma cleaning for 10 min. Subsequently, an aqueous KCl solution (0.745 mg/mL, 10 mM) was applied by spin-coating (acceleration: 3000 rpm, 3000 rpm, 30 s) onto the SnO_2 layer. Afterwards, the substrates were tempered for 10 min at 100 °C.

18

Perovskite deposition: Pb(II) iodide (704 mg, 1.53 mmol), formamidinium iodide (240 mg, 1.40 mmol), $MAPbBr_3$ (7 mg, 15 µmol), and methylammonium chloride (23 mg, 0.34 mmol) were dissolved in *N,N*-dimethylformamide (890 µL) and dimethylsulfoxide (110 µL). After filtration (0.22 µm polytetrafluoroethylene syringe filter), 70 µL of the solution was spin-coated (program: 1. 500 rpm, 5 s; 2. 1000 rpm, 14 s; 3. 5000 rpm, 30 s) on the substrates in a dry air atmosphere. 600 µL diethyl ether was added dynamically 10 s into the third spinning step. The substrates were annealed for one hour at 100 °C and 5 min at 150 °C. Once the substrates were at room temperature, *n*-hexylammonium bromide dissolved in chloroform (250 µL, 2.7 mg/mL, 15 mM) was spin-coated on top of the perovskite. After this 2D-perovskite surface treatment, the substrates were annealed for 10 min at 100 °C.

For the high thermal stability device, the perovskite layer was deposited as follows: Pb(II) iodide (1262 mg, 2.74 mmol), formamidinium iodide (424 mg, 2.47 mmol), and cesium iodide (71 mg, 0.27 mmol) were dissolved in *N,N*-dimethylformamide (1330 µL) and dimethylsulfoxide (164 µL). After filtration (0.22 µm polytetrafluoroethylene syringe filter), 70 µL of the solution was spin-coated (program: 6000 rpm, 30 s) on the substrates in a dry air atmosphere. 300 µL diethyl ether was added dynamically 10 s into the spinning step. The substrates were annealed for 10 min at 150 °C. Once the substrates were at room temperature, poly(methyl methacrylate) dissolved in chlorobenzene (250 µL, 2 mg/mL) was spin-coated on top of the perovskite. After this surface treatment, the substrates were annealed for 10 min at 100 °C.

Finally, a small device-inactive area at the edge of the substrate was cleaned with 2-methoxyethanol-soaked cleanroom swabs to remove the hole transporting and perovskite layer for access to the FTO electrode.

Gold deposition: About 100 nm of gold was thermally evaporated from an alumina-coated molybdenum boat at a pressure below 5×10^{-6} mbar and a deposition rate of 0.5 Å/s for the first 10 nm and 1 Å/s for the remaining 90 nm.

Scanning electron microscopy

Electron microscopy images were recorded with a Zeiss Merlin Gemini 450.

Focused ion beam, transmission electron microscopy, and electron energy loss spectroscopy

The cross-section lamella for transmission electron microscopy was prepared with a FEI Helios NanoLab 600 FIB/SEM system.

The lamella was analyzed using a Thermo Fisher Themis Z G3 Cs-corrected S/TEM operated at 200 kV and equipped with a continuum EEL spectrometer. A 19 mrad convergence angle and 150 pA beam current were used (50 pA for images).

Powder x-ray diffraction

Diffraction patterns were obtained using a PANalytical X'Pert Pro powder X-ray diffractometer, operating with a 1.8 kW Cu–Kα X-ray source and aligned in Bragg-Brentano geometry.

Current-Voltage measurement

The solar cells were protected by applying a polyimide tape with silicone adhesive (7639A12, McMaster-Carr) over the backside of the substrate and gold electrodes. The cells were placed in the measurement setup under ambient air, where the current was measured with a 2420 source measurement unit (Keithley) by applying a voltage. An Oriel Sol3A solar simulator (Newport) combined with a Xenon arc lamp was used for illumination. As a reference, an Oriel reference

silicon solar cell (Newport) was measured to calibrate the irradiance to 1 sun (AM1.5). To stabilize the temperature of the solar cell, a ThermoStation P500 Peltier cooler (McScience) kept the temperature at 20 °C.

Maximum Power Point tracking

A polyimide tape with silicone adhesive (7639A12, McMaster-Carr) was taped over the backside of the perovskite solar cells directly over the gold electrode for protection.

Samples were measured with litos lite (Fluxim) in a sample holder with a heating stage under flushing nitrogen with maximum power point tracking at 85 °C. Illumination of the samples was performed through a quartz window with a LS-2 solar simulator (Wavelabs) under 1-sun.

References

1 NREL - Best Research-Cell Efficiency Chart, https://www.nrel.gov/pv/assets/pdfs/best-research-cell-efficiencies.pdf, (accessed 28 June 2024).

2 J. J. Yoo, G. Seo, M. R. Chua, T. G. Park, Y. Lu, F. Rotermund, Y. K. Kim, C. S. Moon, N. J. Jeon, J. P. Correa-Baena, V. Bulović, S. S. Shin, M. G. Bawendi and J. Seo, *Nature 2021 590:7847*, 2021, **590**, 587–593.

3 A. Uddin and H. Yi, *Solar RRL*, 2022, **6**, 2100983.

4 L. Zhang, H. Bin Wu and X. Wen Lou, *Mater Horiz*, 2013, **1**, 133–138.

5 E. H. Anaraki, A. Kermanpur, L. Steier, K. Domanski, T. Matsui, W. Tress, M. Saliba, A. Abate, M. Gräzel, A. Hagfeldt and J.-P. Correa-Baena, *Energy Environ Sci*, 2016, **9**, 3128–3134.

6 T. Bu, X. Liu, Y. Zhou, J. Yi, X. Huang, L. Luo, J. Xiao, Z. Ku, Y. Peng, F. Huang, Y.-B. Cheng and J. Zhong, *Energy Environ. Sci*, 2017, **10**, 2509.

7 Y. Lu, C. Shih, S. Tan, M. J. Grotevent, L. Wang, H. Zhu, R. Zhang, J.-H. Lee, J.-W. Lee, V. Bulović and M. G. Bawendi, *Advanced Materials*, 2023, **35**, 2304168.

8 N. Ren, L. Tan, M. Li, J. Zhou, Y. Ye, B. Jiao, L. Ding and C. Yi, *iEnergy*, 2024, **3**, 39–45.

9 T. Schneller, R. Waser, M. Kosec and D. Payne, *Chemical solution deposition of functional oxide thin films*, Springer-Verlag Wien, 2013.

10 Y. Yang, Y. Wang and S. Yin, *Appl Surf Sci*, 2017, **420**, 399–406.

11 S. Anuchai, S. Phanichphant, D. Tantraviwat, P. Pluengphon, T. Bovornratanaraks and B. Inceesungvorn, *J Colloid Interface Sci*, 2018, **512**, 105–114.

12 H. Uchiyama, H. Ohgi and H. Imai, *Cryst Growth Des*, 2006, **6**, 2186–2190.

13 S. Supothina, M. R. De Guire, T. P. Niesen, J. Bill, F. Aldinger and A. H. Heuer, *MRS Online Proceedings Library*, 1999, **576**, 203–208.

14 G. Oldfield, T. Ung and P. Mulvaney, *Advanced Materials*, 2000, **12**, 1519–1522.

15 R. Medhi, C. H. Li, S. H. Lee, M. D. Marquez, A. J. Jacobson, T. C. Lee and T. R. Lee, *ACS Appl Nano Mater*, 2019, **2**, 6554–6564.

16 T. Amaya, T. Chiba, K. Suzuki, C. Oda, H. Yoshikawa and M. Yui, *Materials Research Society Symposium Proceedings*, 1997, **465**, 751–758.

17 M. Parashar, V. K. Shukla and R. Singh, *Journal of Materials Science: Materials in Electronics*, 2020, **31**, 3729–3749.

18 Q. Zhao, D. Liu, Z. Li, B. Zhang, X. Sun, Z. Shao, C. Chen, X. Wang, L. Hao, X. Wang, C. Gao, Y. Li, P. Chen, X. Zhang, S. Pang, G. Cui and L. Wang, *Chemical Engineering Journal*, 2022, **443**, 136308.

19 P. Holzhey, M. Prettl, S. Collavini, C. Mortan and M. Saliba, *Scientific report*, 2023, **13**, 6375.

20 N. Li, K. Du, G. Liu, Y. Xie, G. Zhou, J. Zhu, F. Li and H. M. Cheng, *J Mater Chem A Mater*, 2013, **1**, 1536–1539.

21 M. S. Moreno, R. F. Egerton and P. A. Midgley, *Phys Rev B*, 2004, **69**, 233304.

22 M. J. Grotevent, Y. Lu, T. Šverko, M. C. Shih, S. Tan, H. Zhu, T. Dang, J. K. Mwaura, R. Swartwout, F. Beiglböck, L. Kothe, V. Bulović and M. G. Bawendi, *Adv Energy Mater*, 2024, **14**, 2400456.

23 F. Wang, A. Shimazaki, F. Yang, K. Kanahashi, K. Matsuki, Y. Miyauchi, T. Takenobu, A. Wakamiya, Y. Murata and K. Matsuda, *Journal of Physical Chemistry C*, 2017, **121**, 1562–1568.

24 S.-H. Turren-Cruz, A. Hagfeldt and M. Saliba, *Science (1979)*, 2018, **362**, 449–453.

25 P. Ferdowsi, E. Ochoa-Martinez, S. S. Alonso, U. Steiner and M. Saliba, *Sci Rep*, 2020, **10**, 1–10.

26 C. Bi, X. Zheng, B. Chen, H. Wei and J. Huang, *ACS Energy Lett*, 2017, **2**, 1400–1406.

27 C. C. Lin, T. N. Murakami, M. Chikamatsu, T. Bessho, M. Furue and H. Segawa, *ACS Omega*, 2021, **6**, 17880–17889.

28 L. Gu, C. Wang, W. Mo, H. Zeng, C. Shou, S. Yang and F. Wen, *Org Electron*, 2023, **113**, 106677.

Conflict of Interest

The authors declare no conflict of interest.

Data availability

The data that support the findings of this study are available from the corresponding author upon reasonable request.

Author Contributions

M.J.G. and M.G.B. conceived the project. L.K. fabricated the tin oxide films with scientific contributions of M.T. M.J.G. fabricated solar cells from the SnO_2 coated substrates and performed electrical characterization of the devices. Y.L. recorded the scanning electron microscopy images. C.K. performed the X-ray diffraction measurements. M.-C.S. and S.T. contributed to the critical scientific discussions about the perovskite composition and decomposition pathways. M.J.G. and L.K. wrote the manuscript with contributions from all authors. All authors have discussed the results and approved the final version of the manuscript.

Acknowledgments

We thank First Solar for financial support and fruitful discussions. This work was performed in part at the MIT nano Characterization Facilities. We thank Dr. Zhenyuan Zhang at MIT.nano for fabricating the transport layer cross-section and Dr. Aubrey Penn at MIT.nano for the transmission electron microscopy study, including electron energy loss spectroscopy.

M.J.G. acknowledges the support of the Swiss National Science Foundation through the Early Postdoc.Mobility Fellowship grant #P2EZP2_199844. L.K. acknowledges the support of the Fulbright Germany Foundation through the D-Visiting Student Researchers (Doktorand:innen) grant and Woehler Technik GmbH for sponsoring. Y.L. and M.-C.S. acknowledge the support by the U.S. Department of Energy, Solar Energy Technologies Office award no. DE-EE0009512.

Table of Content

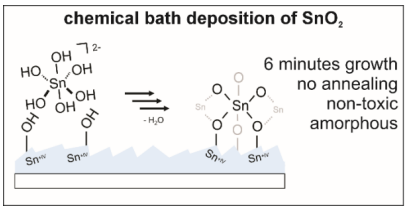

25

Supplementary Information

Non-toxic and rapid chemical bath deposition for SnO_2 electron transporting layers in perovskite solar cells

Matthias J. Grotevent,[1,‡] Linda Kothe,[1,2,‡] Yongli Lu,[1] Chantalle Krajewska,[1] Meng-Chen Shih,[1]

Shaun Tan,[1] Michael Tiemann[2], Moungi G. Bawendi[1*]

[1]Department of Chemistry, Massachusetts Institute of Technology, 77 Massachusetts Avenue, Cambridge, Massachusetts 02139, USA

[2]Paderborn University, Faculty of Science, Department of Chemistry, Warburger Str. 100, D-33098 Paderborn, Germany

E-mail: mgb@mit.edu

[‡]Both authors contributed equally to this work

[*]corresponding author

KEYWORDS: perovskite solar cell, chemical bath deposition, tin oxide, amorphous, metal oxide

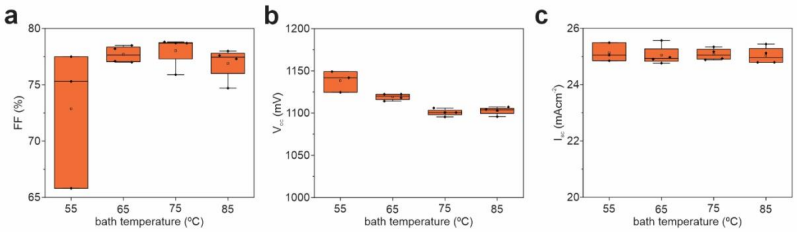

Supplementary Figure 1. *Perovskite solar cell (a) fill factor (FF), (b) open-circuit voltage (V_{oc}), (c) short-circuit current (I_{sc}) at different SnO_2 chemical bath growth temperatures.*

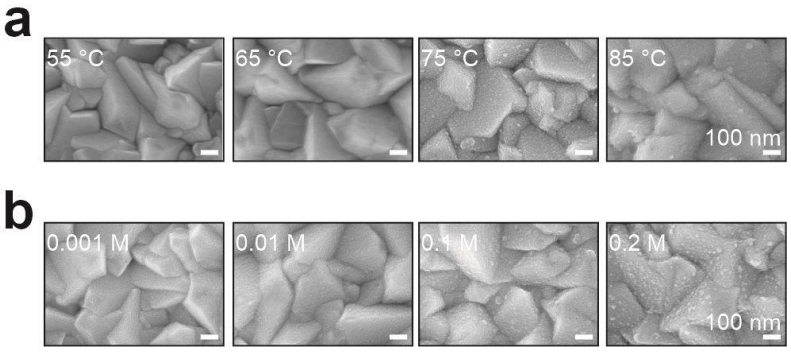

Supplementary Figure 2. *Scanning electron microscopy images of SnO_2 films on FTO substrates fabricated from sodium stannate solutions at (a) different reaction temperatures and (b) different precursor concentrations.*

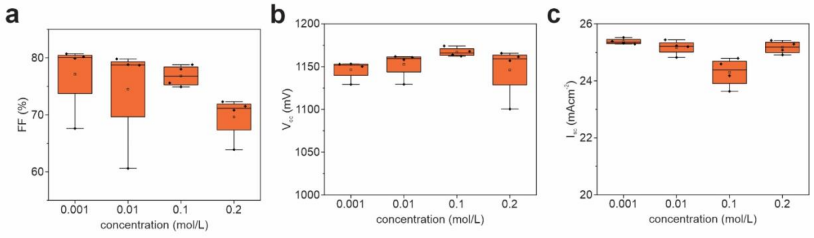

Supplementary Figure 3. *Perovskite solar cell (a) fill factor (FF), (b) open-circuit voltage (V_{oc}), (c) short-circuit current (I_{sc}) at different precursor concentrations for the chemical bath grown SnO_2 layer.*

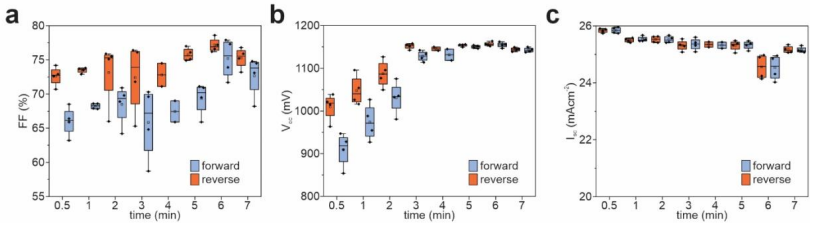

Supplementary Figure 4. *Perovskite solar cell (a) fill factor (FF), (b) open-circuit voltage (V_{oc}), (c) short-circuit current (I_{sc}) at different growth times for the chemical bath grown SnO_2 layer on FTO substrates.*

3

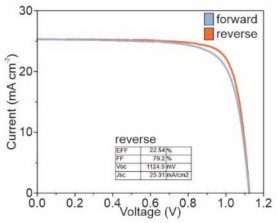

Supplementary Figure 5. *Current-voltage measurement of a perovskite solar cell with Sn(IV)-oxide fabricated from chemical bath deposition with potassium stannate: 1800mg $K_2SnO_3 \cdot 3\ H_2O$ in 50mL deionized water, 85 °C bath temperature, and 5 minutes growth time.*

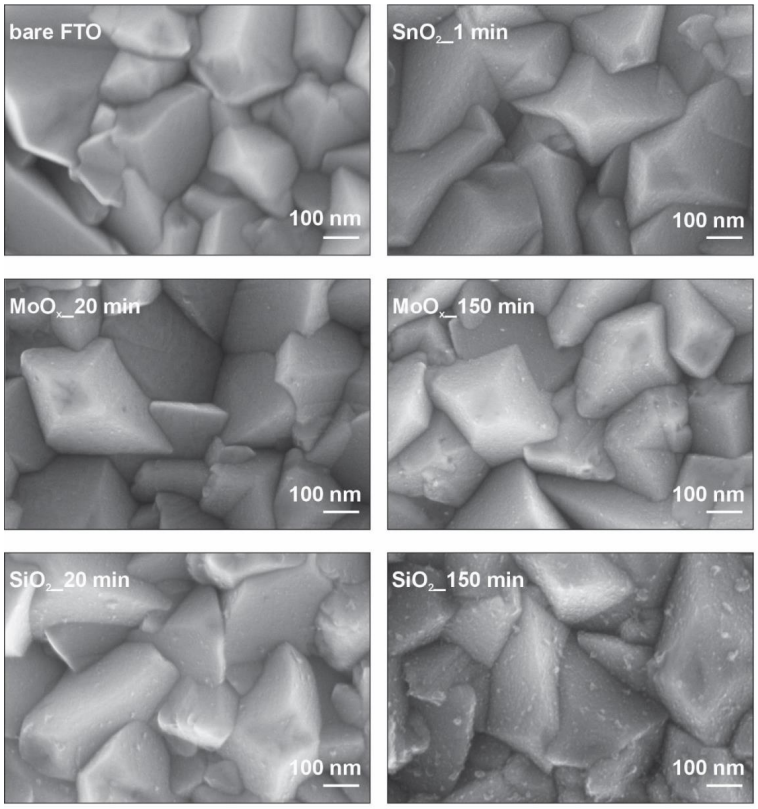

Supplementary Figure 6. *Scanning electron microscopy images of bare FTO and SnO_2, MoO_3, and SiO_2 films on FTO substrates fabricated from sodium stannate, sodium molybdate, and sodium metasilicate solutions, respectively.*

5

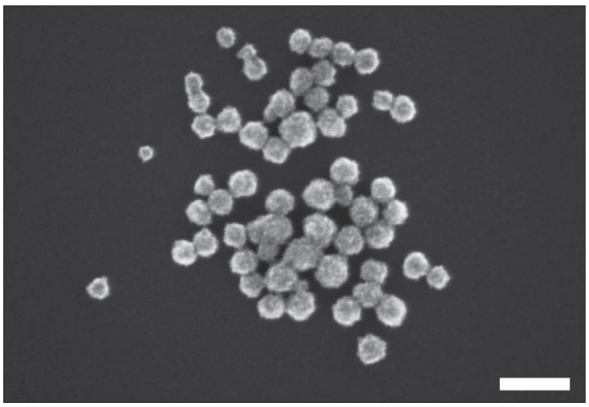

Supplementary Figure 7. *Electron microscopy image of nanoparticles obtained from a chemical bath deposition solution based on sodium stannate precursors. The scale bar is 100 nm.*

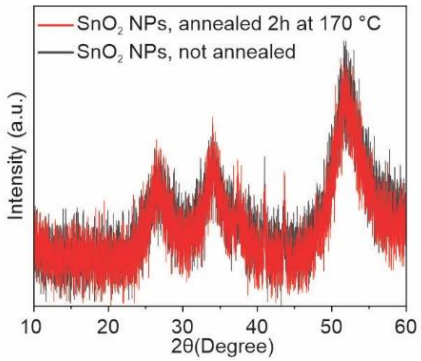

Supplementary Figure 8. *Powder x-ray diffraction patterns of nanoparticles were obtained from a chemical bath deposition solution based on sodium stannate precursors. Low-temperature annealing is not sufficient for the crystallization of* SnO_2.

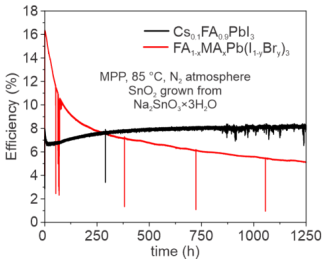

Supplementary Figure 9. *Maximum power point tracking (1-sun; 85 °C; nitrogen atmosphere) of perovskite solar cells with tin oxide electron transport layers both grown from sodium stannate. The influence and stability of the perovskite layer is limiting the efficiency and stability of the devices.*

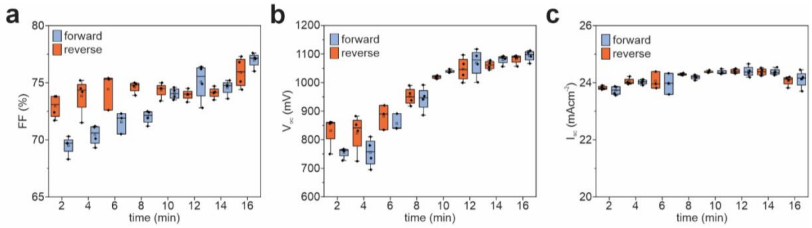

Supplementary Figure 10. *Perovskite solar cell (a) fill factor (FF), (b) open-circuit voltage (V_{oc}), (c) short-circuit current (I_{sc}) at different growth times for the chemical bath grown SnO_2 layer on ITO substrates.*

5 Final Conclusion & Outlook

Tin-based oxides have demonstrated a high degree of versatility in optoelectronic applications. The material requirements for optical O_2 sensors and electron transporting layers (ETLs) in solar cells are very different, but they can be readily adapted using a variety of synthesis routes. Each path unveils noteworthy and prospective performances of the materials.

5.1 Summary of the Work

The central focus of this thesis was the synthesis and investigation of tin-based oxides in two optoelectronic applications: photoluminescence (PL) O_2 sensing and ETLs in perovskite solar cells (PSCs). This research aimed to deepen the understanding of charge carrier recombination as well as electron transport and charge transfer mechanisms at interfaces.

In the case of PL O_2 sensing, temperature- and concentration-dependent PL and conductance studies were executed with zinc tin oxide (Zn_2SnO_4, ZTO). The synthesis of ZTO involved a sol-gel synthesis, subsequently followed by a thermal conversion process. The characterization of the samples was conducted using a variety of analytical methods, including X-ray powder diffraction (PXRD), UV/VIS and PL spectroscopy, as well as scanning electron microscopy (SEM) and energy dispersive X-ray spectroscopy (EDX). An intense and long-lived orange-red emission was detected at room temperature; however, this emission was quenched in the presence of O_2. Consequently, ZTO was identified as an effective material for PL gas sensing applications. As the operating temperature increased, the emission was quenched, thereby revealing the presence of competing mechanisms. Subsequent investigations demonstrated that the emission spectra of orange and red transitions exhibit distinct characteristics, including a shift in wavelength as the temperature rises. These emissions also interact with oxygen in a manner that differs from one another. The variation of operating temperature, O_2 concentration, and simultaneous measurement of PL and conductance demonstrated the relation between models for PL sensing with metal-organic compounds and resistive sensing with metal oxides. Stern-Volmer plots showed that the Stern-Volmer constant increased with temperature, indicating dynamic quenching. A deviation from linear behavior, manifesting as a downward curvature, was observed. The application of the modified Stern-Volmer model revealed the incomplete accessibility of the luminescent centers to O_2. The adaptation of this model to the conductance data enabled a qualitative comparison of the accessibility of luminescent centers and charge carriers. Moreover, the comparison of conductance and PL as measurands indicated that PL exhibited greater sensitivity to changes in gas concentration. These findings are fundamental to the understanding of the sensing mechanism of PL O_2 sensing with metal oxides. The temperature-dependence of the emission intensity followed a Fermi-Dirac function, thereby providing further insight into the band scheme of ZTO and band bending. The activation energy obtained may reveal the band bending induced by O_2 chemisorption. These contributions to the sensing mechanism

deepen the understanding of the surface-near region in the presence of O_2 and connect temperature-dependent PL measurements with the field of semiconductor gas sensing. Furthermore, a comprehensive banding scheme was developed by ZTO, which contributes to a better understanding of the material.

In the context of solar cells, the deposition of SnO_2 layers was accomplished through the implementation of chemical bath deposition (CBD) on fluorine-doped tin oxide (FTO) and indium tin oxide (ITO) substrates. The thermal decomposition of sodium stannate ($Na_2SnO_3{\cdot}3H_2O$) resulted in the heterogeneous layer growth on the substrates and homogeneous growth in solution forming nanoparticles. The SnO_2 layers were characterized using a variety of analytical methods, including SEM, transmission electron microscopy (TEM), and energy electron loss spectroscopy (EELS). The fabrication of perovskite solar cells (PSCs) with SnO_2 ETLs was conducted, and I-V curves were subsequently measured. In contrast to traditional CBD methods, which are complex reactions requiring multiple precursors, this approach employs solely the tin salt, constraining the synthesis process to the variables of reaction temperature, educt concentration, and reaction time. On FTO substrates, optimal efficiencies were attained within 6 min of coating. In such conditions, the formation of SnO_2 layers with a thickness of *approx.* 9 nm occured. The TEM and EELS measurements indicated the amorphous nature of the layers, which are likely nonstoichiometric. This finding contradicts the prevailing assumption that only crystalline layers can attain high device performance, as amorphous layers have been shown to achieve comparable efficiency. The successful layer deposition on ITO was also remarkable, as conventional methods contain hydrochloric acid (HCl), which etches ITO. The layer formation process on ITO exhibits was prolonged in comparison to that observed on FTO, necessitating additional optimization. The finding that amorphous SnO_2 layers are in no way inferior to crystalline ones contributes to the general understanding of ETLs. Moreover, the reduction of reaction time from 12 h to 6 min, as well as the elimination of harmful chemicals, serve to significantly simplify the deposition process.

5.2 Outlook

In the field of PL gas sensing, several issues can be addressed in future works. In this study, the particle morphology was not the primary focus of research; however, it is likely to have a significant impact on gas accessibility and sensitivity. The variation of specific surface area and subsequent simultaneous PL and conductance measurements may contribute to a more profound understanding of the topic. Precise Fermi level engineering can optimize gas sensitivity, which can be achieved through the doping of ZTO or the formation of composites. The investigation could be expanded to include other gases or humidity.

While the reaction conditions appear to be optimal for FTO substrates, the deposition on ITO substrates is not yet fully developed. The role of the cation may also be of further interest. In addition to $Na_2SnO_3{\cdot}3H_2O$, $K_2SnO_3{\cdot}3H_2O$ can also be utilized for the SnO_2 deposition. As the cation exerts a substantial influence on the passivation of ETL and perovskite, a comparative analysis of these two entities could facilitate a more profound comprehension. In order to achieve an enhanced level of efficiency in the prepared PSCs, it may be advantageous to optimize the other layers as well.

Bibliography

[1] X. Yu, T. J. Marks, A. Facchetti, *Nature Materials* **2016**, *15*, 383–396, DOI 10.1038/nmat4599.

[2] D. Nunes, A. Pimentel, A. Gonçalves, S. Pereira, R. Branquinho, P. Barquinha, E. Fortunato, R. Martins, *Semiconductor Science and Technology* **2019**, *34*, 043001, DOI 10.1088/1361-6641/ab011e.

[3] A. Fioravanti, P. Marani, S. Morandi, L. Giordano, P. Maddalena, M. C. Carotta, S. Lettieri, *Chemosensors* **2021**, *9*, DOI 10.3390/chemosensors9070163.

[4] S. Amrehn, X. Wu, T. Wagner, *ACS Sensors* **2018**, *3*, 191–199, DOI 10.1021/acssensors.7b00845.

[5] X.-d. Wang, O. S. Wolfbeis, *Chemical Society Reviews* **2014**, *43*, 3666–3761, DOI 10.1039/C4CS00039K.

[6] J. Seo, H. Yoo, *Membranes* **2022**, *12*, DOI 10.3390/membranes12050485.

[7] M.-T. Tsai, Y.-S. Chang, Y.-C. Liu, *Ceramics International* **2017**, *43*, S428–S434, DOI 10.1016/j.ceramint.2017.05.251.

[8] L. Kothe, J. Klippstein, M. Kloß, M. Wengenroth, M. Poeplau, S. Ester, M. Tiemann, *ChemPhysChem* **2025**, *26*, e202400984, DOI 10.1002/cphc.202400984.

[9] L. Kothe, M. Kloß, T. Wagner, M. Wengenroth, M. Poeplau, S. Ester, M. Tiemann, *The Journal of Physical Chemistry C* **2025**, *129*, 9239–9245, DOI 10.1021/acs.jpcc.5c01678.

[10] N. R. E. L. .-. U. D. of Energy, Best Research-Cell Efficiency Chart, https://www2.nrel.gov/pv/cell-efficiency, (accessed: 07.05.2025).

[11] S. Philipps, W. Warmuth, Photovoltaics Report, https://www.ise.fraunhofer.de/en/publications/studies/photovoltaics-report.html, (accessed: 07.05.2025).

[12] Y. Masuda, *Sensors and Actuators B: Chemical* **2022**, *364*, 131876, DOI 10.1016/j.snb.2022.131876.

[13] A. T. Raisa, S. N. Sakib, M. J. Hossain, K. A. Rocky, A. Kowsar, *Solar Energy Advances* **2025**, *5*, 100105, DOI 10.1016/j.seja.2025.100105.

[14] M. Noman, Z. Khan, S. T. Jan, *RSC Advances* **2024**, *14*, 5085–5131, DOI 10.1039/D3RA07518D.

[15] J. J. Yoo, G. Seo, M. R. Chua, T. G. Park, Y. Lu, F. Rotermund, Y.-K. Kim, C. S. Moon, N. J. Jeon, J.-P. Correa-Baena, V. Bulović, S. S. Shin, M. G. Bawendi, J. Seo, *Nature* **2021**, *590*, 587–593, DOI 10.1038/s41586-021-03285-w.

[16] M. J. Grotevent, L. Kothe, Y. Lu, C. Krajewska, M.-C. Shih, S. Tan, M. Tiemann, M. G. Bawendi, *Chemistry of Materials* **2025**, submitted.

[17] R. M. Pasquarelli, D. S. Ginley, R. O'Hayre, *Chemical Society Reviews* **2011**, *40*, 5406–5441, DOI 10.1039/C1CS15065K.

[18] Q. Wali, M. Aamir, M. Ejaz Khan, R. Jose, W. Fan, S. Yang, *Solar Energy* **2024**, *270*, 112382, DOI 10.1016/j.solener.2024.112382.

[19] A. Galdámez-Martinez, G. Santana, F. Güell, P. R. Martínez-Alanis, A. Dutt, *Nanomaterials* **2020**, *10*, DOI 10.3390/nano10050857.

[20] E. Keles, M. Yildirim, T. Öztürk, O. A. Yildirim, *Materials Science in Semiconductor Processing* **2020**, *110*, 104959, DOI 10.1016/j.mssp.2020.104959.

[21] C. K. G. Kwok, Y. Wang, X. Shu, K. M. Yu, *Applied Surface Science* **2023**, *627*, 157295, DOI 10.1016/j.apsusc.2023.157295.

[22] G. K. Dalapati et al., *Journal of Materials Chemistry A* **2021**, *9*, 16621–16684, DOI 10.1039/D1TA01291F.

[23] E. Riedel, C. Janiak, *Anorganische Chemie*, 10th ed., De Gruyter, Berlin, Boston, **2022**, DOI 10.1515/9783110694444.

[24] M. Batzill, U. Diebold, *Progress in Surface Science* **2005**, *79*, 47–154, DOI 10.1016/j.progsurf.2005.09.002.

[25] S. Anuchai, S. Phanichphant, D. Tantraviwat, P. Pluengphon, T. Bovornratanaraks, B. Inceesungvorn, *Journal of Colloid and Interface Science* **2018**, *512*, 105–114, DOI 10.1016/j.jcis.2017.10.047.

[26] T. Yang, J. Zhao, X. Li, X. Gao, C. Xue, Y. Wu, R. Tai, *Materials Letters* **2015**, *139*, 39–41, DOI 10.1016/j.matlet.2014.10.040.

[27] W. H. Baur, *Acta Crystallographica* **1956**, *9*, 515–520, DOI 10.1107/S0365110X56001388.

[28] J. Zhang, L. Gao, *Journal of Solid State Chemistry* **2004**, *177*, 1425–1430, DOI 10.1016/j.jssc.2003.11.024.

[29] F. Li, J. Xu, X. Yu, L. Chen, J. Zhu, Z. Yang, X. Xin, *Sensors and Actuators B: Chemical* **2002**, *81*, 165–169, DOI 10.1016/S0925-4005(01)00947-9.

[30] H. Yang, Y. Hu, A. Tang, S. Jin, G. Qiu, *Journal of Alloys and Compounds* **2004**, *363*, 276–279, DOI 10.1016/S0925-8388(03)00473-0.

[31] R. S. M. Parashar, V. K. Shukla, *Journal of Materials Science: Materials in Electronics* **2020**, *31*, 3729–3749, DOI 10.1007/s10854-020-02994-8.

[32] R. Al-Gaashani, S. Radiman, N. Tabet, A. Daud, *Materials Science and Engineering: B* **2012**, *177*, 462–470, DOI 10.1016/j.mseb.2012.02.006.

[33] G. Sangami, N. Dharmaraj, *Spectrochimica Acta Part A: Molecular and Biomolecular Spectroscopy* **2012**, *97*, 847–852, DOI 10.1016/j.saa.2012.07.068.

[34] M. J. Hampden-Smith, T. A. Wark, C. Brinker, *Coordination Chemistry Reviews* **1992**, *112*, 81–116, DOI 10.1016/0010-8545(92)80006-D.

[35] R. W. J. Scott, N. Coombs, G. A. Ozin, *Journal of Materials Chemistry* **2003**, *13*, 969–974, DOI 10.1039/B206002G.

[36] G. W. S. C. J. Brinker, *Sol-Gel Science - The Physics and Chemistry of Sol-Gel Processing*, Academic Press, Inc., San Diego, **1990**, DOI 10.1016/C2009-0-22386-5.

[37] R. Huang, L. Hou, B. Zhou, Q. Zhao, S. Ren, *Journal of Non-Crystalline Solids* **2005**, *351*, 23–28, DOI 10.1016/j.jnoncrysol.2004.09.023.

[38] J. P. Correa Baena, A. G. Agrios, *ACS Applied Materials & Interfaces* **2014**, *6*, 19127–19134, DOI 10.1021/am505115x.

[39] G. Zhang, M. Liu, *Journal of Materials Science* **1999**, *34*, 3213–3219, DOI 10.1023/A:1004685907751.

[40] M. Ganchev, A. Katerski, S. Stankova, J. S. Eensalu, P. Terziyska, R. Gergova, G. Popkirov, P. Vitanov, *Journal of Physics: Conference Series* **2019**, *1186*, 012027, DOI 10.1088/1742-6596/1186/1/012027.

[41] D. H. Carvalho, M. Schiavon, M. Raposo, R. de Paiva, J. Alves, R. M. Paniago, N. Speziali, A. Ferlauto, J. Ardisson, *Physics Procedia* **2012**, *28*, 22–27, DOI 10.1016/j.phpro.2012.03.664.

[42] S. Siegrist, P. Nandi, R. K. Kothandaraman, A. Abdessalem, A. N. Tiwari, F. Fu, *Solar RRL* **2023**, *7*, 2300273, DOI 10.1002/solr.202300273.

[43] M. Rieu, M. Camara, G. Tournier, J.-P. Viricelle, C. Pijolat, N. F. de Rooij, D. Briand, *Sensors and Actuators B: Chemical* **2016**, *236*, 1091–1097, DOI 10.1016/j.snb.2016.06.042.

[44] T. Bu, J. Li, F. Zheng, W. Chen, X. Wen, Z. Ku, Y. Peng, J. Zhong, Y.-B. Cheng, F. Huang, *Nature Communications* **2018**, *9*, DOI 10.1038/s41467-018-07099-9.

[45] A. van Mol, Y. Chae, A. McDaniel, M. Allendorf, *Thin Solid Films* **2006**, *502*, 72–78, DOI 10.1016/j.tsf.2005.07.247.

[46] S. R. Mishra, M. Ahmaruzzaman, *Nanoscale* **2022**, *14*, 1566–1605, DOI 10.1039/D1NR07040A.

[47] C. Avis, J. Jang, *Membranes* **2022**, *12*, DOI 10.3390/membranes12010007.

[48] E. N. Dattoli, Q. Wan, W. Guo, Y. Chen, X. Pan, W. Lu, *Nano Letters* **2007**, *7*, 2463–2469, DOI 10.1021/nl0712217.

[49] M. Maleki Shahraki, S. Alipour, P. Mahmoudi, A. Karimi, *Ceramics International* **2018**, *44*, 20386–20390, DOI https://doi.org/10.1016/j.ceramint.2018.08.031.

[50] P. Sennu, V. Aravindan, Y.-S. Lee, *Chemical Engineering Journal* **2017**, *324*, 26–34, DOI 10.1016/j.cej.2017.05.003.

[51] A. Sharma, A. Ahmed, A. Singh, S. K. Oruganti, A. Khosla, S. Arya, *Journal of the Electrochemical Society* **2021**, *168*, DOI 10.1149/1945-7111/abdee8.

[52] T. Wagner, C.-D. Kohl, M. Fröba, M. Tiemann, *Sensors* **2006**, *6*, 318–323, DOI 10.3390/s6040318.

[53] J. Cheng, J. Wang, Q. Li, H. Liu, Y. Li, *Journal of Industrial and Engineering Chemistry* **2016**, *44*, 1–22, DOI 10.1016/j.jiec.2016.08.008.

[54] A. M. Al-Hamdi, U. Rinner, M. Sillanpää, *Process Safety and Environmental Protection* **2017**, *107*, 190–205, DOI 10.1016/j.psep.2017.01.022.

[55] S. T. Nipa, R. Akter, A. Raihan, S. bin Rasul, U. Som, S. Ahmed, J. Alam, M. R. Khan, S. Enzo, W. Rahman, *Environmental Science and Pollution Research* **2022**, *29*, 10871–10893, DOI 10.1007/s11356-021-17933-1.

[56] J. Azevedo, S. D. Tilley, M. Schreier, M. Stefik, C. Sousa, J. P. Araújo, A. Mendes, M. Grätzel, M. T. Mayer, *Nano Energy* **2016**, *24*, 10–16, DOI 10.1016/j.nanoen.2016.03.022.

[57] S. Abanades, P. Charvin, F. Lemont, G. Flamant, *International Journal of Hydrogen Energy* **2008**, *33*, 6021–6030, DOI https://doi.org/10.1016/j.ijhydene.2008.05.042.

[58] C. Altinkaya, E. Aydin, E. Ugur, F. H. Isikgor, A. S. Subbiah, M. De Bastiani, J. Liu, A. Babayigit, T. G. Allen, F. Laquai, A. Yildiz, S. De Wolf, *Advanced Materials* **2021**, *33*, 2005504, DOI 10.1002/adma.202005504.

[59] Q. Wali, A. Fakharuddin, R. Jose, *Journal of Power Sources* **2015**, *293*, 1039–1052, DOI 10.1016/j.jpowsour.2015.06.037.

[60] N. Garino, A. Sacco, M. Castellino, J. A. Muñoz-Tabares, A. Chiodoni, V. Agostino, V. Margaria, M. Gerosa, G. Massaglia, M. Quaglio, *ACS Applied Materials & Interfaces* **2016**, *8*, 4633–4643, DOI 10.1021/acsami.5b11198.

[61] M. Dou, M. Hou, D. Liang, W. Lu, Z. Shao, B. Yi, *Electrochimica Acta* **2013**, *92*, 468–473, DOI 10.1016/j.electacta.2013.01.070.

[62] M. A. Azam, N. E. Safie, A. S. Ahmad, N. A. Yuza, N. S. A. Zulkifli, *Journal of Energy Storage* **2021**, *33*, 102096, DOI 10.1016/j.est.2020.102096.

[63] Y. Zhang, Z. Bi, Y. Liang, W. Zuo, G. Xu, M. Zhu, *Energy Storage Materials* **2022**, *48*, 35–43, DOI 10.1016/j.ensm.2022.03.002.

[64] S. Wu, S. Yuan, L. Shi, Y. Zhao, J. Fang, *Journal of Colloid and Interface Science* **2010**, *346*, 12–16, DOI 10.1016/j.jcis.2010.02.031.

[65] Q.-P. Tran, J.-S. Fang, T.-S. Chin, *Materials Science in Semiconductor Processing* **2015**, *40*, 664–669, DOI 10.1016/j.mssp.2015.07.047.

[66] X. Shi, K. Xu, *Materials Science in Semiconductor Processing* **2017**, *58*, 1–7, DOI 10.1016/j.mssp.2016.09.038.

[67] J. E. N. Swallow, B. A. D. Williamson, T. J. Whittles, M. Birkett, T. J. Featherstone, N. Peng, A. Abbott, M. Farnworth, K. J. Cheetham, P. Warren, D. O. Scanlon, V. R. Dhanak, T. D. Veal, *Advanced Functional Materials* **2018**, *28*, 1701900, DOI 10.1002/adfm.201701900.

[68] G. Zhang, C. Xie, S. Zhang, S. Zhang, Y. Xiong, *The Journal of Physical Chemistry C* **2014**, *118*, 18097–18109, DOI 10.1021/jp503059e.

[69] S. Kumar, Bhawna, S. K. Yadav, A. Gupta, R. Kumar, J. Ahmed, M. Chaudhary, Suhas, V. Kumar, *Environmental Science and Pollution Research* **2022**, *29*, 47448–47461, DOI 10.1007/s11356-022-18946-0.

[70] Z. Ji, Z. He, Y. Song, K. Liu, Z. Ye, *Journal of Crystal Growth* **2003**, *259*, 282–285, DOI 10.1016/j.jcrysgro.2003.07.003.

[71] A. Azam, A. S. Ahmed, M. S. Ansari, M. Shafeeq M, A. H. Naqvi, *Journal of Alloys and Compounds* **2010**, *506*, 237–242, DOI 10.1016/j.jallcom.2010.06.184.

[72] J. Ni, X. Zhao, X. Zheng, J. Zhao, B. Liu, *Acta Materialia* **2009**, *57*, 278–285, DOI 10.1016/j.actamat.2008.09.013.

[73] N. Nadaud, N. Lequeux, M. Nanot, J. Jové, T. Roisnel, *Journal of Solid State Chemistry* **1998**, *135*, 140–148, DOI 10.1006/jssc.1997.7613.

[74] M. Alam, D. Cameron, *Thin Solid Films* **2000**, *377-378*, 455–459, DOI 10.1016/S0040-6090(00)01369-9.

[75] Y. Li, Z. Liu, Q. Li, Z. Liu, L. Zeng, *Hydrometallurgy* **2011**, *105*, 207–212, DOI 10.1016/j.hydromet.2010.09.006.

[76] K. Zhang, Y. Wu, W. Wang, B. Li, Y. Zhang, T. Zuo, *Resources Conservation and Recycling* **2015**, *104*, 276–290, DOI 10.1016/j.resconrec.2015.07.015.

[77] K. Litzius, *Chemie in unserer Zeit* **2017**, *51*, 10–11, DOI 10.1002/ciuz.201790000.

[78] F. Lu, Q. Liu, *Journal of Low Temperature Physics* **2020**, *200*, 142–151, DOI 10.1007/s10909-020-02479-2.

[79] C. Janiak, H.-J. Meyer, D. Gudat, C. Schulzke, *Riedel Moderne Anorganische Chemie*, De Gruyter, Berlin, Boston, **2023**, DOI 10.1515/9783110790221.

[80] L. Gracia, A. Beltrán, J. Andrés, *The Journal of Physical Chemistry C* **2011**, *115*, 7740–7746, DOI 10.1021/jp2006606.

[81] L. Bao, J. Zang, G. Wang, X. Li, *Nano Letters* **2014**, *14*, 6505–6509, DOI 10.1021/nl503077y.

[82] H. Kawazoe, K. Ueda, *Journal of the American Ceramic Society* **1999**, *82*, 3330–3336, DOI 10.1111/j.1151-2916.1999.tb02247.x.

[83] J. Choisnet, A. Deschanvres, B. Raveau, *Comptes rendus de l'Académie des sciences C* **1968**, *266*, 543–545.

[84] T. Hashemi, H. M. Al-Allak, J. Illingsworth, A. W. Brinkman, J. Woods, *Journal of Materials Science Letters* **1990**, *9*, 776–778, DOI 10.1007/BF00720155.

[85] J. Lee, S.-C. Lee, C. S. Hwang, J.-H. Choi, *Journal of Materials Chemistry C* **2013**, *1*, 6364–6374, DOI 10.1039/C3TC30960F.

[86] P. Šimonová, L. Kotrbová, W. Pabst, V. Nečina, P. Bezdička, *Journal of the European Ceramic Society* **2024**, *44*, 6586–6596, DOI 10.1016/j.jeurceramsoc.2024.04.029.

[87] E. L. Foletto, J. M. Simões, M. A. Mazutti, S. L. Jahn, E. I. Muller, L. S. F. Pereira, E. M. de Moraes Flores, *Ceramics International* **2013**, *39*, 4569–4574, DOI 10.1016/j.ceramint.2012.11.053.

[88] J. Fang, A. Huang, P. Zhu, N. Xu, J. Xie, J. Chi, S. Feng, R. Xu, M. Wu, *Materials Research Bulletin* **2001**, *36*, 1391–1397, DOI 10.1016/S0025-5408(01)00621-3.

[89] S.-J. Seo, Y. H. Hwang, B.-S. Bae, *Electrochemical and Solid-State Letters* **2010**, *13*, H357, DOI 10.1149/1.3474606.

[90] Y. Son, A. Liao, R. L. Peterson, *Journal of Materials Chemistry C* **2017**, *5*, 8071–8081, DOI 10.1039/C7TC02343J.

[91] S. S. Shin, W. S. Yang, J. H. Noh, J. H. Suk, N. J. Jeon, J. H. Park, J. S. Kim, W. M. Seong, S. I. Seok, *Nature Communications* **2015**, *6*, DOI 10.1038/ncomms8410.

[92] C. Kim, N.-H. Lee, Y.-K. Kwon, B. Kang, *Thin Solid Films* **2013**, *544*, 129–133, DOI 10.1016/j.tsf.2013.04.051.

[93] A. R. Hegazy, B. Salameh, A. Alsmadi, *Ceramics International* **2019**, *45*, 19473–19480, DOI 10.1016/j.ceramint.2019.06.204.

[94] R. Medhi, C.-H. Li, S. H. Lee, P. Srinoi, M. D. Marquez, F. Robles-Hernandez, A. J. Jacobson, T.-C. Lee, T. R. Lee, *ACS Applied Nano Materials* **2020**, *3*, 8958–8971, DOI 10.1021/acsanm.0c01702.

[95] I.-J. Lee, N.-E. Sung, K. H. Chae, R. Conley, *Thin Solid Films* **2013**, *548*, 385–388, DOI 10.1016/j.tsf.2013.08.067.

[96] J. S. Rajachidambaram, S. Sanghavi, P. Nachimuthu, V. Shutthanandan, T. Varga, B. Flynn, S. Thevuthasan, G. S. Herman, *Journal of Materials Research* **2012**, *27*, 2309–2317, DOI 10.1557/jmr.2012.170.

[97] Sharanu, A. Kompa, M. Murari, D. Kekuda, M. Mahesha, K. Mohan Rao, *Ceramics International* **2021**, *47*, 35294–35301, DOI 10.1016/j.ceramint.2021.09.072.

[98] R. Bashir, M. K. Bilal, A. Bashir, S. U. Asif, Y. Peng, *Small* **2024**, *20*, 2402500, DOI 10.1002/smll.202402500.

[99] J. S. Kim, Y. Jang, S. Kang, Y. Lee, K. Kim, W. Kim, W. Lee, C. S. Hwang, *The Journal of Physical Chemistry C* **2020**, *124*, 26780–26792, DOI 10.1021/acs.jpcc.0c07800.

[100] B. Kim, J. Park, M. L. Geier, M. C. Hersam, A. Dodabalapur, *ACS Applied Materials & Interfaces* **2015**, *7*, 12009–12014, DOI 10.1021/acsami.5b02093.

[101] O. Klymov, M. Yermakov, R. Pshenychnyi, O. Dobrozhan, S. Agouram, M. C. Martínez-Tomás, A. Opanasyuk, V. Muñoz-Sanjosé, *Applied Surface Science Advances* **2023**, *18*, 100521, DOI 10.1016/j.apsadv.2023.100521.

[102] W. Jackson, G. Herman, R. Hoffman, C. Taussig, S. Braymen, F. Jeffery, J. Hauschildt, *Journal of Non-Crystalline Solids* **2006**, *352*, 1753–1755, DOI 10.1016/j.jnoncrysol.2005.11.080.

[103] D. Kim, Y. Jeong, K. Song, S.-K. Park, G. Cao, J. Moon, *Langmuir* **2009**, *25*, 11149–11154, DOI 10.1021/la901436p.

[104] T. Ivetić, N. Finčur, L. R. Đačanin, B. Abramović, S. Lukić-Petrović, *Materials Research Bulletin* **2015**, *62*, 114–121, DOI 10.1016/j.materresbull.2014.11.001.

[105] P. P. Das, A. Roy, M. Tathavadekar, P. S. Devi, *Applied Catalysis B: Environmental* **2017**, *203*, 692–703, DOI 10.1016/j.apcatb.2016.10.035.

[106] L. Mohapatra, A. K. Kushwaha, *The Journal of Physical Chemistry Letters* **2024**, *15*, 2279–2286, DOI 10.1021/acs.jpclett.3c03396.

[107] L. Sun, S. Li, Y. Su, D. He, Z. Zhang, *Applied Surface Science* **2019**, *463*, 474–480, DOI 10.1016/j.apsusc.2018.08.246.

[108] B. Tan, E. Toman, Y. Li, Y. Wu, *Journal of the American Chemical Society* **2007**, *129*, 4162–4163, DOI 10.1021/ja070804f.

[109] L. S. Oh, D. H. Kim, J. A. Lee, S. S. Shin, J.-W. Lee, I. J. Park, M. J. Ko, N.-G. Park, S. G. Pyo, K. S. Hong, J. Y. Kim, *The Journal of Physical Chemistry C* **2014**, *118*, 22991–22994, DOI 10.1021/jp509183k.

[110] J. Dou, D. Shen, Y. Li, A. Abate, M. Wei, *ACS Applied Materials & Interfaces* **2019**, *11*, 36553–36559, DOI 10.1021/acsami.9b09209.

[111] X. Yang, Z. Miao, Q. Zhong, H. Liu, Z. Yang, J. Yu, *Journal of Alloys and Compounds* **2023**, *948*, 169579, DOI 10.1016/j.jallcom.2023.169579.

[112] J. Song, X. Lu, Q. Tian, L. Cui, J. Chen, Z. Sui, *Journal of Alloys and Compounds* **2022**, *910*, 164924, DOI 10.1016/j.jallcom.2022.164924.

[113] S. Hemmatzadeh Saeedabad, C. Baratto, F. Rigoni, S. Rozati, G. Sberveglieri, K. Vojisavljevic, B. Malic, *Materials Science in Semiconductor Processing* **2017**, *71*, 461–469, DOI 10.1016/j.mssp.2017.09.006.

[114] S. Dutta, A. Dodabalapur, *Sensors and Actuators B: Chemical* **2009**, *143*, 50–55, DOI 10.1016/j.snb.2009.07.056.

[115] H. Fan, S. Xu, X. Cao, D. Liu, Y. Yin, H. Hao, D. Wei, Y. Shen, *Applied Surface Science* **2017**, *400*, 440–445, DOI 10.1016/j.apsusc.2016.12.221.

[116] D. B. Papkovsky, R. I. Dmitriev, *Chemical Society Reviews* **2013**, *42*, 8700–8732, DOI 10.1039/C3CS60131E.

[117] Sandhya, *LWT - Food Science and Technology* **2010**, *43*, 381–392, DOI 10.1016/j.lwt.2009.05.018.

[118] R. Moos, *International Journal of Applied Ceramic Technology* **2005**, *2*, 401–413, DOI 10.1111/j.1744-7402.2005.02041.x.

[119] A. Jones, *Atmospheric Environment* **1999**, *33*, 4535–4564, DOI 10.1016/S1352-2310(99)00272-1.

[120] F. Karagulian, M. Barbiere, A. Kotsev, L. Spinelle, M. Gerboles, F. Lagler, N. Redon, S. Crunaire, A. Borowiak, *Atmosphere* **2019**, *10*, DOI 10.3390/atmos10090506.

[121] O. S. Wolfbeis, *BioEssays* **2015**, *37*, 921–928, DOI 10.1002/bies.201500002.

[122] S. Halley, K. P. Ramaiyan, L.-k. Tsui, F. Garzon, *Sensors and Actuators B: Chemical* **2022**, *370*, 132363, DOI 10.1016/j.snb.2022.132363.

[123] J. N. Demas, B. A. DeGraff, P. B. Coleman, *Analytical Chemistry* **1999**, *71*, 793A–800A, DOI 10.1021/ac9908546.

[124] D. B. Papkovsky, Methods in Enzymology **2004**, *381*, 715–735, DOI https://doi.org/10.1016/S0076-6879(04)81046-2.

[125] M. Quaranta, S. M. Borisov, I. Klimant, *Bioanal Rev* **2012**, *4*, 115–157, DOI 10.1007/s12566-012-0032-y.

[126] K. Müller-Buschbaum, F. Beuerle, C. Feldmann, *Microporous and Mesoporous Materials* **2015**, *216*, 171–199, DOI 10.1016/j.micromeso.2015.03.036.

[127] M. Poeplau, S. Ester, B. Henning, T. Wagner, *Physical Chemistry Chemical Physics* **2020**, *22*, 19948–19956, DOI 10.1039/D0CP02269A.

[128] W. Wu, S. Ji, W. Wu, H. Guo, X. Wang, J. Zhao, Z. Wang, *Sensors and Actuators B: Chemical* **2010**, *149*, 395–406, DOI 10.1016/j.snb.2010.06.043.

[129] S. Tobita, T. Yoshihara, *Current Opinion in Chemical Biology* **2016**, *33*, 39–45, DOI 10.1016/j.cbpa.2016.05.017.

[130] K. Habermüller, A. Ramanavicius, V. Laurinavicius, W. Schuhmann, *Electroanalysis* **2000**, *12*, 1383–1389, DOI 10.1002/1521-4109(200011)12:17<1383::AID-ELAN1383>3.0.CO;2-0.

[131] S. M. Borisov, G. Nuss, I. Klimant, *Analytical Chemistry* **2008**, *80*, 9435–9442, DOI 10.1021/ac801521v.

[132] J. R. Lakowicz, *Principles of Fluorescence Spectroscopy*, 3rd ed., Springer New York, **2006**, DOI 10.1007/978-0-387-46312-4.

[133] P. I. Djurovich, D. Murphy, M. E. Thompson, B. Hernandez, R. Gao, P. L. Hunt, M. Selke, *Dalton Trans.* **2007**, 3763–3770, DOI 10.1039/B704595F.

[134] I. Pelant, J. Valenta, *Luminescence Spectroscopy of Semiconductors*, Oxford University Press, New York, **2012**, DOI 10.1093/acprof:oso/9780199588336.001.0001.

[135] M. Ishikawa, M. Watanabe, T. Hayakawa, M. Koishi, *Analytical Chemistry* **1995**, *67*, 511–518, DOI 10.1021/ac00099a005.

[136] M. Wahl, *Technical Note - Time-Correlated Single Photon Counting*, PicoQuant GmbH.

[137] D. S. Tyson, J. Bialecki, F. N. Castellano, *Chemical Communications* **2000**, 2355–2356, DOI 10.1039/B007336I.

[138] E. A. Medlycott, G. S. Hanan, *Chemical Society Reviews* **2005**, *34*, 133–142, DOI 10.1039/B316486C.

[139] D. A. Rusak, W. H. I. James, M. J. Ferzola, M. J. Stefanski, *Journal of Chemical Education* **2006**, *83*, 1857, DOI 10.1021/ed083p1857.

[140] S. Draxler, M. E. Lippitsch, I. Klimant, H. Kraus, O. S. Wolfbeis, *The Journal of Physical Chemistry* **1995**, *99*, 3162–3167, DOI 10.1021/j100010a029.

[141] M. T. Murtagh, M. R. Shahriari, M. Krihak, *Chemistry of Materials* **1998**, *10*, 3862–3869, DOI 10.1021/cm9802806.

[142] S. S. Lehrer, *Biochemistry* **1971**, *10*, 3254–3263, DOI 10.1021/bi00793a015.

[143] J. N. Demas, B. A. DeGraff, W. Xu, *Analytical Chemistry* **1995**, *67*, 1377–1380, DOI 10.1021/ac00104a012.

[144] M. M. Choi, D. Xiao, *Analytica Chimica Acta* **2000**, *403*, 57–65, DOI 10.1016/S0003-2670(99)00640-6.

[145] P. Hartmann, M. J. Leiner, P. Kohlbacher, *Sensors and Actuators B: Chemical* **1998**, *51*, 196–202, DOI 10.1016/S0925-4005(98)00188-9.

[146] Z. J. Fuller, W. D. Bare, K. A. Kneas, W.-Y. Xu, J. N. Demas, B. A. DeGraff, *Analytical Chemistry* **2003**, *75*, 2670–2677, DOI 10.1021/ac0261707.

[147] S. Oguzlar, M. Z. Ongun, *Journal of Materials Science: Materials in Electronics* **2024**, *35*, DOI 10.1007/s10854-024-12507-6.

[148] M. Anaya, A. Rubino, M. E. Calvo, H. Míguez, *Journal of Materials Chemistry C* **2016**, *4*, 4532–4537, DOI 10.1039/C6TC00663A.

[149] S. Morab, M. M. Sundaram, A. Pivrikas, *Coatings* **2023**, *13*, DOI 10.3390/coatings13091657.

[150] U. Wijesinghe, G. Longo, O. S. Hutter, *Energy Advances* **2023**, *2*, 12–33, DOI 10.1039/D2YA00232A.

[151] W. Bludau, A. Onton, W. Heinke, *Journal of Applied Physics* **1974**, *45*, 1846–1848, DOI 10.1063/1.1663501.

[152] J. D. Patterson, B. C. Bailey, *Solid-State Physics-Introduction to the Theory*, Springer Cham, Basel, **2019**, DOI 10.1007/978-3-319-75322-5.

[153] M. J. Madou, S. R. Morrison, *Chemical Sensing with Solid State Devices*, Academic Press, Inc., San Diego, **1989**, DOI 10.1016/C2009-0-22258-6.

[154] A. Staerz, U. Weimar, N. Barsan, *Sensors and Actuators B: Chemical* **2022**, *358*, 131531, DOI 10.1016/j.snb.2022.131531.

[155] M. Tiemann, *Chemistry – A European Journal* **2007**, *13*, 8376–8388, DOI 10.1002/chem.200700927.

[156] H. Ji, W. Zeng, Y. Li, *Nanoscale* **2019**, *11*, 22664–22684, DOI 10.1039/C9NR07699A.

[157] Z. Li, H. Li, Z. Wu, M. Wang, J. Luo, H. Torun, P. Hu, C. Yang, M. Grundmann, X. Liu, Y. Fu, *Materials Horizons* **2019**, *6*, 470–506, DOI 10.1039/C8MH01365A.

[158] M. A. Reshchikov, *physica status solidi (a)*, *218*, 2000101, DOI 10.1002/pssa.202000101.

[159] M. Schön, *Z. Physik* **1942**, 463–471, DOI 10.1007/BF01339783.

[160] H. Klasens, *Nature* **1946**, 306–307, DOI 10.1038/158306c0.

[161] M. Poeplau, *Untersuchung der sauerstoffinduzierten Quenchingmechanismen zinkbasierter Luminophore*, Dissertation - Paderborn University, **2021**, DOI 10.17619/UNIPB/1-1160.

[162] J. E. Martin, L. E. Shea-Rohwer, *Journal of Luminescence* **2006**, *121*, 573–587, DOI 10.1016/j.jlumin.2005.12.043.

[163] M. A. Becker, C. Bernasconi, M. I. Bodnarchuk, G. Rainò, M. V. Kovalenko, D. J. Norris, R. F. Mahrt, T. Stöferle, *ACS Nano* **2020**, *14*, 14939–14946, DOI 10.1021/acsnano.0c04401.

[164] F. Shan, Y. Yu, *Journal of the European Ceramic Society* **2004**, *24*, 1869–1872, DOI 10.1016/S0955-2219(03)00490-4.

[165] F. Kröger, H. Vink in (Eds.: F. Seitz, D. Turnbull), Solid State Physics, Academic Press, **1956**, pp. 307–435, DOI 10.1016/S0081-1947(08)60135-6.

[166] A. Galdámez-Martinez, G. Santana, F. Güell, P. R. Martínez-Alanis, A. Dutt, *Nanomaterials* **2020**, *10*, DOI 10.3390/nano10050857.

[167] R. Marin, F. Oussta, S. N. Katea, S. Prabhudev, G. A. Botton, G. Westin, E. Hemmer, *Journal of Materials Chemistry C* **2019**, *7*, 3909–3919, DOI 10.1039/C9TC00215D.

[168] P. Mondal, *Optical Materials* **2019**, *98*, 109476, DOI 10.1016/j.optmat.2019.109476.

[169] A. Teke, Ü. Özgür, S. Do ğan, X. Gu, H. Morko ç, B. Nemeth, J. Nause, H. O. Everitt, *Physical Review B* **2004**, *70*, 195207, DOI 10.1103/PhysRevB.70.195207.

[170] H. He, Z. Ye, S. Lin, B. Zhao, J. Huang, H. Tang, *The Journal of Physical Chemistry C* **2008**, *112*, 14262–14265, DOI 10.1021/jp8023099.

[171] A. B. Djurišić, Y. H. Leung, K. H. Tam, Y. F. Hsu, L. Ding, W. K. Ge, Y. C. Zhong, K. S. Wong, W. K. Chan, H. L. Tam, K. W. Cheah, W. M. Kwok, D. L. Phillips, *Nanotechnology* **2007**, *18*, 095702, DOI 10.1088/0957-4484/18/9/095702.

[172] X. Xiang, X. T. Zu, S. Zhu, L. M. Wang, V. Shutthanandan, P. Nachimuthu, Y. Zhang, *Journal of Physics D: Applied Physics* **2008**, *41*, 225102, DOI 10.1088/0022-3727/41/22/225102.

[173] F. Gu, S. F. Wang, M. K. Lü, G. J. Zhou, D. Xu, D. R. Yuan, *The Journal of Physical Chemistry B* **2004**, *108*, 8119–8123, DOI 10.1021/jp036741e.

[174] F. Gu, S. Fen Wang, C. Feng Song, M. Kai Lü, Y. Xin Qi, G. Jun Zhou, D. Xu, D. Rong Yuan, *Chemical Physics Letters* **2003**, *372*, 451–454, DOI 10.1016/S0009-2614(03)00440-8.

[175] M. A. Z. G. Sial, M. Iqbal, Z. Siddique, M. A. Nadeem, M. Ishaq, A. Iqbal, *Journal of Molecular Structure* **2017**, *1144*, 355–359, DOI 10.1016/j.molstruc.2017.05.067.

[176] A. D. Pramata, K. Suematsu, A. T. Quitain, M. Sasaki, T. Kida, *Advanced Functional Materials* **2018**, *28*, 1704620, DOI 10.1002/adfm.201704620.

[177] J. Zhou, M. Zhang, J. Hong, Z. Yin, *Solid State Communications* **2006**, *138*, 242–246, DOI 10.1016/j.ssc.2006.03.007.

[178] J. H. He, T. H. Wu, C. L. Hsin, K. M. Li, L. J. Chen, Y. L. Chueh, L. J. Chou, Z. L. Wang, *Small* **2006**, *2*, 116–120, DOI 10.1002/smll.200500210.

[179] X. Zhang, T. Lin, P. Zhang, J. Xu, S. Lin, L. Xu, K. Chen, *Optics Express* **2014**, *22*, 369–376, DOI 10.1364/OE.22.000369.

[180] L. Chantelle, C. O. de Lima, M. C. Dantas, M. Siu-Li, R. R. Menezes, F. S. de Souza, A. L. M. de Oliveira, I. M. G. dos Santos, *Journal of Thermal Analysis and Calorimetry* **2024**, 4453–4468, DOI 10.1007/s10973-024-13020-y.

[181] J. Xue, D. Lei, Q. Bi, C. Tang, L. Zhang, *Optical Materials* **2020**, *108*, 110454, DOI 10.1016/j.optmat.2020.110454.

[182] I. Arora, P. Kumar, *Materials Research Express* **2020**, *7*, 035023, DOI 10.1088/2053-1591/ab730e.

[183] C. Mrabet, R. Dridi, N. Mahdhi, M. Amlouk, *Journal of Alloys and Compounds* **2017**, *725*, 765–772, DOI 10.1016/j.jallcom.2017.07.212.

[184] R. Dridi, C. Mrabet, A. Labidi, N. Mahdhi, A. Amlouk, M. Amlouk, *Journal of Alloys and Compounds* **2017**, *708*, 769–779, DOI 10.1016/j.jallcom.2017.03.055.

[185] A. Kamo, O. Ates Sonmezoglu, S. Sonmezoglu, *ACS Applied Bio Materials* **2024**, *7*, 8656–8670, DOI 10.1021/acsabm.4c01447.

[186] N. H. Hanh, T. M. Ngoc, L. Van Duy, C. M. Hung, N. Van Duy, N. D. Hoa, *Sensors and Actuators B: Chemical* **2021**, *343*, 130147, DOI 10.1016/j.snb.2021.130147.

[187] P. Santhoshkumar, K. Prasanna, Y. N. Jo, S. H. Kang, Y. C. Joe, C. W. Lee, *Applied Surface Science* **2018**, *449*, 514–520, DOI 10.1016/j.apsusc.2018.01.120.

[188] S. Yang, J. Zhang, *Chemical Physics Letters* **2018**, *712*, 40–43, DOI 10.1016/j.cplett.2018.09.061.

[189] L. Vien, N. Tu, M. T. Tran, N. Van Du, D. Nguyen, D. Viet, N. Quang, D. Trung, P. Huy, *Optical Materials* **2020**, *100*, 109670, DOI 10.1016/j.optmat.2020.109670.

[190] V. T. T. Le, D. M. Tien, V. X. Dao, T. Nguyen, H. T. Phan, *Journal of Electronic Materials* **2025**, *54*, 3001–3013, DOI 10.1007/s11664-025-11798-7.

[191] L. Vien, N. Tu, D. Viet, D. Anh, D. Nguyen, P. Huy, *Journal of Luminescence* **2020**, *227*, 117522, DOI 10.1016/j.jlumin.2020.117522.

[192] A. B. A. Kayani, S. Kuriakose, M. Monshipouri, F. A. Khalid, S. Walia, S. Sriram, M. Bhaskaran, *Small* **2021**, *17*, 2100621, DOI 10.1002/smll.202100621.

[193] B.-X. Wei, L. Zhao, T.-J. Wang, H. Gao, H.-X. Wu, Y. Jin, *Advanced Powder Technology* **2013**, *24*, 708–713, DOI 10.1016/j.apt.2012.12.009.

[194] H. D. Pham, T. C.-J. Yang, S. M. Jain, G. J. Wilson, P. Sonar, *Advanced Energy Materials* **2020**, *10*, 1903326, DOI 10.1002/aenm.201903326.

[195] P. Roy, N. K. Sinha, S. Tiwari, A. Khare, *Solar Energy* **2020**, *198*, 665–688, DOI 10.1016/j.solener.2020.01.080.

[196] M. Grätzel, S. Ahmad, S. Kazim, *Perovskite Solar Cells: Materials, Processes, and Devices*, Wiley-VCH GmbH, Weinheim, **2022**, DOI 10.1002/9783527825790.

[197] N. Nikfar, N. Memarian, *Optik* **2022**, *258*, 168932, DOI 10.1016/j.ijleo.2022.168932.

[198] J. Hutton, R. J. Nelmes, G. M. Meyer, V. R. Eiriksson, *Journal of Physics C: Solid State Physic* **1979**, *12*, 5393, DOI 10.1088/0022-3719/12/24/011.

[199] S. Arya, P. Mahajan, *Solar Cells*, Springer Singapore, Singapore, **2023**, DOI 10.1007/978-981-99-7333-0.

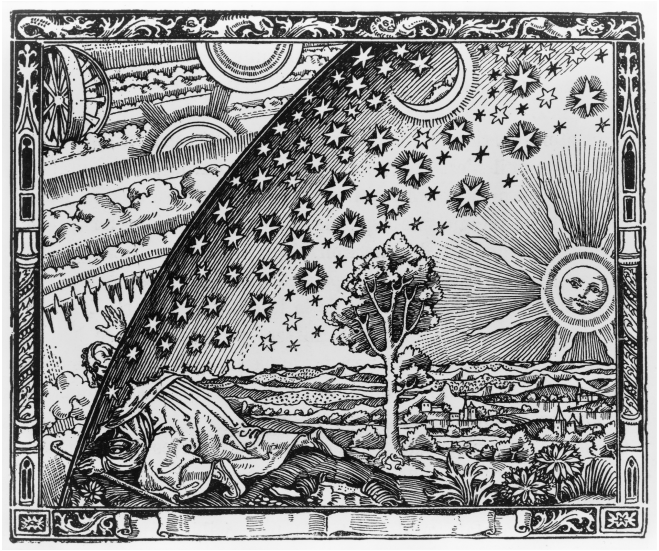

Camille Flammarion's *L'atmosphère: météorologie populaire* (Paris: Hachette, 1888), p. 163